

A novel sub-grid model for super-Eddington accretion of spinning black holes in galaxy-scale simulations

Wei-Bo Kao,^{1*} Pedro R. Capelo,² Elia Cenci,³ Lucio Mayer,² Alessandro Lupi⁴ and Luca Sala⁵

¹*Department of Physics, ETH Zürich, Wolfgang-Pauli-Strasse 27, CH-8093 Zürich, Switzerland*

²*Department of Astrophysics, University of Zurich, Winterthurerstrasse 190, CH-8057 Zürich, Switzerland*

³*Department of Astronomy, University of Geneva, Chemin d'Ecogia, CH-1290 Versoix, Switzerland*

⁴*DiSAT, Università degli Studi dell'Insubria, via Valleggio 11, IT-22100 Como, Italy*

⁵*Universitäts-Sternwarte, Fakultät für Physik, Ludwig-Maximilians-Universität München, Scheinerstr. 1, DE-81679 München, Germany*

Accepted XXX. Received YYY; in original form ZZZ

ABSTRACT

Super-Eddington accretion has been proposed to explain the existence of black holes (BHs) with masses exceeding a billion solar masses within the first billion years after the Big Bang. We present a novel accretion disc-based sub-grid model for BH mass and spin evolution in the super-Eddington regime, implemented in the hydrodynamics code GIZMO. In our model, motivated by results of radiation-hydrodynamics simulations of accretion discs, the growth of the BH is mediated by a sub-grid accretion disc, comprising an inner photon-trapping region described by simulation-based fitting formulae and an outer thin α -disc with three regions. We incorporate a self-consistent spin evolution prescription that transitions between the Bardeen-Petterson effect and inner thick-disc precession, depending on the accretion rate. We perform a suite of idealised simulations of a BH embedded in a gaseous circumnuclear disc and a spherically distributed stellar component to explore the conditions under which super-Eddington accretion can be sustained in the environment of a realistic galactic nucleus. Simulations with misaligned gas inflows onto an initially aligned BH-disc system yield very high Eddington ratios, triggered by the rapid removal of disc angular momentum via inflows. Mildly super-Eddington accretion can also be maintained when the BH is misaligned with the disc, as the Lense-Thirring effect reduces the disc angular momentum. These results highlight the importance of angular momentum misalignment in enabling super-Eddington accretion and suggest that such episodes are difficult to trigger unless the system resides in a highly dynamical environment – a condition more likely to occur in high-redshift galaxies. Our model potentially provides a way to grow moderate-mass BH seeds to the sizes required to explain the bright high-redshift quasars.

Key words: accretion, accretion discs – black hole physics – galaxies: nuclei – methods: numerical – quasars: supermassive black holes.

1 INTRODUCTION

It is widely accepted that most galaxies host a supermassive black hole (SMBH) at their centre (Kormendy & Richstone 1995). Some SMBHs are responsible for the luminous emission observed in active galactic nuclei (AGN; Schmidt 1963) due to the accretion of gas from their surroundings (Lynden-Bell 1969; Antonucci 1993). SMBHs also play a crucial role in galaxy formation and evolution through accretion and feedback processes, potentially driving their co-evolution with their host galaxies (King 2003; Di Matteo et al. 2005; Fabian 2012; Kormendy & Ho 2013; Heckman & Best 2014; King & Pounds 2015).

Prior to the launch of the James Webb Space Telescope (JWST), observations of AGN at $z \gtrsim 6$ revealed SMBHs with $M_{\text{BH}} > 10^9 M_{\odot}$ (Mortlock et al. 2011; Bañados et al. 2018;

Yang et al. 2020; Wang et al. 2021; Yang et al. 2021; Fan et al. 2023). With the launch of JWST, such observations have been extended to $z \sim 10$, with detections of SMBHs with masses as high as $10^6 M_{\odot}$ (Larson et al. 2023; Maiolino et al. 2024). These discoveries present a significant challenge in explaining how such massive SMBHs already exist so early in cosmic history (see a recent review by Inayoshi et al. 2020).

One possible explanation is the formation of heavy seed BHs with high initial masses under peculiar conditions (Dijkstra et al. 2006; Latif et al. 2015; Boekholt et al. 2018; Wise et al. 2019; Volonteri et al. 2021; Toyouchi et al. 2023; Zwick et al. 2023; Mayer et al. 2024, 2025). Alternatively, seed BHs could undergo episodes of super-Eddington accretion with rapid mass growth (Madau et al. 2014; Volonteri et al. 2015; Lupi et al. 2016; Regan et al. 2019; Hu et al. 2022b; Massonneau et al. 2023b; Sassano et al. 2023; Lupi et al. 2024a; Piana et al. 2024; Shi et al. 2024; Chiu et al. 2025; Huško et al. 2025).

* E-mail: weikao@student.ethz.ch

Candidates for super-Eddington accretion events have been observed in the local Universe in tidal disruption events (TDEs; Lin et al. 2017; Dai et al. 2018), ultra-luminous X-ray sources (ULXs; Bachetti et al. 2014; Motch et al. 2014), and AGN (Jin et al. 2012; Du et al. 2015, 2018; Liu et al. 2021; Abuter et al. 2024; Marziani et al. 2025). Recently, Abuter et al. (2024) dynamically measured the mass of a super-Eddington-accreting SMBH at $z \sim 2$, whereas JWST also identified a potential super-Eddington-accreting SMBH at $z \sim 4$ (Suh et al. 2025). Moreover, Leung et al. (2024) and Lupi et al. (2024b) suggest that JWST may observe an extensive population of super-Eddington-accreting SMBHs at $z > 4$. Super-Eddington accretion has also been proposed as a possible explanation for the X-ray weakness problem and non-detection of high-ionization emission lines in the “little red dots” observed by JWST (Inayoshi et al. 2024; Lambrides et al. 2024; Pacucci & Narayan 2024; Madau 2025).

The thin α -disc model is commonly used to describe the structure of accretion flows around BHs (Shakura & Sunyaev 1973; Frank et al. 2002; Kato et al. 2008, hereafter K08). However, super-Eddington accretion flows cannot be adequately described by the commonly used standard thin α -disc model, since advection significantly alters the structure of the disc. Instead, they are better described by the slim disc model (Abramowicz et al. 1988), a one-dimensional (1D) accretion disc model that accounts for the advection of the photons. Approximate analytical solutions have been derived by Wang & Zhou (1999) and Watarai (2006), whereas numerical relativistic solutions have been obtained by Sądowski (2009, 2011).

Further simulations have provided deeper insight into this process (e.g. Ohsuga et al. 2005; Jiang et al. 2014; Inayoshi et al. 2016; Sądowski & Narayan 2016; Kitaki et al. 2018, hereafter K18; Jiang et al. 2019; Kitaki et al. 2021; Hu et al. 2022a; Yoshioka et al. 2024). These studies have elucidated how extreme physical conditions inherent to super-Eddington flows – such as high radiation pressure, complex magnetic fields, strong outflows, and turbulent accretion – affect the accretion process (Mayer 2019; Jiang & Dai 2024).

The mass of an SMBH is not its only fundamental parameter, its spin being also crucial to its evolution. The spin determines the location of the innermost stable circular orbit (ISCO; Bardeen et al. 1972), which modulates the rate of BH growth by altering the radiative efficiency and the structures of the disc (Sądowski 2009; Lopez Armengol et al. 2021; Inayoshi & Ichikawa 2024). A rapidly spinning SMBH is also responsible for the production of relativistic jets (Blandford & Znajek 1977). Furthermore, both the direction and magnitude of the spin influence the feedback exerted on the BH surroundings, impacting the accretion process and the evolution of the host galaxy (Silk & Rees 1998; McKinney et al. 2012; King & Pounds 2015; Sala et al. 2021; Massonneau et al. 2023a; Ricarte et al. 2023; Bollati et al. 2024).

The growth of SMBHs during galactic evolution is a complex and multi-scale process spanning over ten orders of magnitude in spatial scale, from the event horizon of the SMBH to the scales of entire galaxies and the cosmic web. Resolving BH physics across this vast spatial range in cosmological simulations remains computationally unfeasible. Progress has been made by focusing on a limited range of spatial or temporal scales (e.g. Guo et al. 2023, 2024; Hopkins et al. 2024).

Another widely adopted approach is the accretion disc par-

ticle method, in which the SMBH is represented as an unresolved composite SMBH-accretion disc particle (e.g. Power et al. 2011; Dubois et al. 2014; Fiacconi et al. 2018; Cenci et al. 2021, hereafter C21; Tarténas & Zubovas 2022; Massonneau et al. 2023a,b; Koudmani et al. 2024; Huško et al. 2025). In this framework, the SMBH is evolved by tracking the mass and angular momentum flows onto the accretion disc.

In many of these models, the BH mass accretion rate is estimated using the Bondi-Hoyle-Lyttleton prescription (BHL; Hoyle & Lyttleton 1939; Bondi & Hoyle 1944; Bondi 1952). However, this approach neglects the influence of the gas angular momentum, which strongly regulates accretion. To address this limitation, Fiacconi et al. (2018) introduced a steady-state accretion disc-mediated accretion rate, which was further refined by C21 and Koudmani et al. (2024). By contrast, Tarténas & Zubovas (2022) introduced the viscous evolution of the disc, allowing for a more general treatment in scenarios wherein the inflow rate changes rapidly, finding that accounting for the disc viscous evolution leads to different BH growth histories and BH feedback effects compared to the BHL prescription.

In this paper, we develop the first sub-grid model of an SMBH-accretion disc particle that is capable of capturing the evolution of both the SMBH mass and spin allowing for super-Eddington accretion. Our model builds upon and extends the framework introduced by C21 (see also Fiacconi et al. 2018) and is implemented in the publicly available code GIZMO (Hopkins 2015).

The remainder of the paper is structured as follows. Section 2 provides a detailed theoretical description of this model. Section 3 outlines its numerical implementation and simulation setup. Section 4 presents our results. In Section 5, we discuss the relevance of super-Eddington accretion and the caveats of our model. Finally, we summarise our findings in Section 6.

2 THE SUPER-EDDINGTON MODEL

An astrophysical BH is characterised by its mass, $M_{\text{BH}} = 10^6 M_{\text{BH},6} M_{\odot}$, and angular momentum, $\mathbf{J}_{\text{BH}} = J_{\text{BH}} \hat{\mathbf{j}}_{\text{BH}}$, where \mathbf{J}_{BH} and J_{BH} denote the BH angular momentum vector and magnitude, respectively.¹ The (dimensionless) spin parameter of the BH is defined as $a_{\text{BH}} = cJ_{\text{BH}}/(GM_{\text{BH}}^2)$, where G is the gravitational constant, and c is the speed of light in vacuum. Since the maximum angular momentum of a BH is GM_{BH}^2/c (Kerr 1963), the theoretical range of a_{BH} is between 0 (for a non-spinning BH) and 1 (for a maximally spinning BH).² However, during accretion, the theoretical upper limit of a_{BH} is 0.998, due to the torque exerted by retrograde photons (Thorne 1974), thus we cap a_{BH} to such a value.

An accreting BH releases energy according to

¹ We neglect the BH charge, as it is generally believed that electrically charged BHs cannot exist stably in astrophysical environments (e.g. Gibbons 1975; Blandford & Znajek 1977).

² We note that other authors (e.g. Kerr 1963) define the BH spin as $J_{\text{BH}}/(M_{\text{BH}}c)$ (with units of length), so that its maximum value is given by GM_{BH}/c^2 .

$$L_{\text{BH}} = \eta \dot{M}_{\text{BH,accr}} c^2, \quad (1)$$

where L_{BH} is the BH (bolometric) luminosity originating from the conversion of gravitational potential energy into radiation as gas is accreted, $\dot{M}_{\text{BH,accr}}$ is the BH mass accretion rate, and $\eta = 0.1\eta_{0.1}$ is the radiative efficiency, that is how much of the rest energy of the accreting gas is converted into radiation. This luminosity has a theoretical upper limit, given by the Eddington (1916) luminosity, L_{Edd} , which defines the maximum accretion power a celestial object undergoing a spherically symmetric accretion process (such as an accreting star or BH) can achieve when the outward pressure of radiation, generated in the accretion flow, counteracts the inward pull of gravity:

$$L_{\text{Edd}} = \frac{4\pi G M_{\text{BH}} \mu_e m_p c}{\sigma_T}, \quad (2)$$

where m_p is the proton mass, μ_e is the mean molecular weight per electron, and σ_T is the Thomson scattering cross-section. We assume $\mu_e = 1$ for simplicity (as in K08).

Following Equation (1), the Eddington mass accretion rate is then $\dot{M}_{\text{Edd},\eta} = L_{\text{Edd}}/(\eta c^2)$ and we also introduce the corresponding Eddington ratio as $f_{\text{Edd},\eta} = \dot{M}_{\text{BH,accr}}/\dot{M}_{\text{Edd},\eta}$. The radiative efficiency is not a constant and can vary as a function of spin and accretion rate (Bardeen et al. 1972; Sądowski 2009; Madau et al. 2014). However, a characteristic value is usually assumed for the definition of Eddington mass accretion rate, so that the latter quantity does not depend on the varying radiative efficiency (although it still obviously depends on the varying BH mass). Therefore, we also define the Eddington mass accretion rate and Eddington ratio for a fixed value of η , for ease of comparison with other literature, picking $\eta = 1/16$ (as in Sądowski 2009; Madau et al. 2014) and obtaining $\dot{M}_{\text{Edd},16} = 16 L_{\text{Edd}}/c^2$ and $f_{\text{Edd},16} = \dot{M}_{\text{BH,accr}}/\dot{M}_{\text{Edd},16}$.³

We mediate accretion onto the BH via an accretion disc with physical properties that reflect the state of the BH and the surrounding gas reservoir. The accretion disc size is R_{disc} , the total mass is M_{disc} , and the total angular momentum is denoted as $\mathbf{J}_{\text{disc}} = J_{\text{disc}} \mathbf{j}_{\text{disc}}$, with J_{disc} and \mathbf{j}_{disc} being its magnitude and unit vector, respectively. To model the accretion disc structure, we define the disc surface density and specific angular momentum at a given radius R (in cylindrical coordinates) as, respectively, $\Sigma(R)$ and $\mathbf{L}(R) = L(R) \mathbf{l}(R)$, where $L(R)$ is the magnitude and $\mathbf{l}(R)$ is the unit vector. The disc temperature, volume density, total pressure, and scale height are denoted as $T(R)$, $\rho(R)$, $P(R)$, and $H(R)$, respectively. Here, H is defined as $H = c_s/\Omega_K$, where c_s is

³ Other authors define the Eddington mass accretion rate as $\dot{M}_{\text{Edd},10} = 10 L_{\text{Edd}}/c^2$ (e.g. Jiang et al. 2019; Hu et al. 2022a; Massonneau et al. 2023b) or $\dot{M}_{\text{Edd},1} = L_{\text{Edd}}/c^2$ (e.g. K08; Kitaki et al. 2021; Liu et al. 2021), with corresponding definitions of the Eddington ratio as $f_{\text{Edd},10} = \dot{M}_{\text{BH,accr}}/\dot{M}_{\text{Edd},10}$ and $f_{\text{Edd},1} = \dot{M}_{\text{BH,accr}}/\dot{M}_{\text{Edd},1}$ (the latter denoted as \dot{m} in some works). The relation between the different definitions of the Eddington ratio is $f_{\text{Edd},16} = 10 f_{\text{Edd},10}/16 = f_{\text{Edd},1}/16 = f_{\text{Edd},\eta}/(16\eta) = 10 f_{\text{Edd},\eta}/(16\eta_{0.1})$. Note that f_{Edd} in Perego et al. (2009); Dubois et al. (2014); Fiacconi et al. (2018); Bustamante & Springel (2019); C21; Sala et al. (2021) is equal to our $f_{\text{Edd},\eta}$.

the sound speed of the gas and $\Omega_K = \sqrt{GM_{\text{BH}}/R^3}$ is its Keplerian angular velocity.

In the accretion disc, the mass inflow is driven by the radial viscosity, ν_1 , as it is responsible for transporting angular momentum, thereby driving the inflow. Following K08, the viscosity prescription is given by the $r\phi$ -component of the shear stress tensor, $t_{r\phi} = -\alpha P$, where $\alpha = 0.1\alpha_{0.1}$ is a dimensionless constant for describing the viscosity: this is equivalent to $\nu_1 = 2\alpha c_s H/3$. We note the presence of an extra factor of $2/3$ in this expression compared to the original formulation by Shakura & Sunyaev (1973; see Appendix B for further details).

In our model, we consider the situation in which the BH might not be aligned with the disc (i.e. \mathbf{J}_{disc} is not parallel to \mathbf{J}_{BH}) and investigate the evolution of the BH in this scenario. In this case, the spinning BH generates a frame-dragging effect on the misaligned disc, known as the Lense-Thirring effect (Lense & Thirring 1918). Consequently, when a disc is tilted relative to the spinning BH, it naturally becomes warped (i.e. the tilt angle of the disc varies with radius) due to the Lense-Thirring effect. We note that, in this model, we assume that \mathbf{j}_{disc} corresponds to the direction of the outer part of the warped accretion disc (as in Perego et al. 2009; Fiacconi et al. 2018). The justification for this assumption is given in Section 2.4.3. For a thin disc, the vertical viscosity, ν_2 , acts to damp the warps and tends to align each disc ring with its neighbours.⁴ This is related to ν_1 by the relation

$$\frac{\nu_2}{\nu_1} = \frac{\xi}{2\alpha^2}, \quad (3)$$

where ξ is a dimensionless constant of order unity (Papaloizou & Pringle 1983; Lodato & Pringle 2007).

2.1 Model overview

In our model, a BH particle represents a sub-grid system consisting of a BH surrounded by its accretion disc. The unresolved accretion disc is described by its global properties: M_{disc} and \mathbf{J}_{disc} . Our model extends from previous accretion disc-based BH growth sub-grid models (Power et al. 2011; Dubois et al. 2014; Fiacconi et al. 2018; C21; Massonneau et al. 2023b; Koudmani et al. 2024). The mass and angular momentum of the BH and accretion disc are evolved considering accretion from the accretion disc onto the BH, external inflows from the large-scale gas onto the disc, and relativistic torques exerted by the spinning BH onto the disc.

Most previous sub-grid models describe the structure of the accretion disc using only the outer region of the thin α -disc model [i.e. region (c), introduced in Section 2.2] to describe the structure of the accretion disc. However, the thin α -disc model [even when considering all regions: (a), (b), and (c)] is valid only when the disc is optically thick and radiative cooling is efficient. Consequently, it applies only at intermediate Eddington ratios, $0.01 \lesssim f_{\text{Edd},16} \lesssim 0.2$ (Laor & Netzer 1989; Koratkar & Blaes 1999; Narayan & McClintock 2008).

Koudmani et al. (2024) extended this popular sub-grid

⁴ The third viscosity, ν_3 , which represents a torque that induces precession when a disc ring is misaligned with its neighbours, is often neglected, as it is typically negligible compared to other viscosities in a thin Keplerian disc (Ogilvie 1999).

Table 1. Overview of our sub-grid model.

Components	Relevant equations and quantities
Disc structure (Sec. 2.2)	Use four regions to describe the accretion disc: Structure : $\begin{cases} \text{Photon-trapping region (} L \text{ and } \Sigma \text{ follow Eqs 10 and 11)} & \text{if } R_{\text{ISCO}} \leq R < R_{\text{trap}} \\ \text{Region (a) of thin } \alpha\text{-disc (Eqs 12 and 15)} & \text{if } \max(R_{\text{ISCO}}, R_{\text{trap}}) \leq R < R_{\text{ab}} \\ \text{Region (b) of thin } \alpha\text{-disc (Eqs 13 and 15)} & \text{if } R_{\text{ab}} \leq R < R_{\text{bc}} \\ \text{Region (c) of thin } \alpha\text{-disc (Eqs 14 and 15)} & \text{if } R_{\text{bc}} \leq R \end{cases}$ $R_{\text{ISCO}}, R_{\text{trap}}, R_{\text{ab}}, \text{ and } R_{\text{bc}}$ are given by Eqs (4), (7), (8), and (9), respectively.
Mass accretion rate (Sec. 2.3)	$f_{\text{Edd},16}$ is calculated using the Newton-Raphson method by solving for it based on the integrated disc properties, specifically M_{disc} and J_{disc} . The maximum value for $f_{\text{Edd},16}$, $f_{\text{Edd},16,\text{max}}$, is given by Eq. (20).
Angular momentum (Sec. 2.4)	$\mathbf{J}_{\text{BH}} = \mathbf{J}_{\text{BH,acc}} + \mathbf{J}_{\text{BH,LT}}$ $\mathbf{J}_{\text{BH,acc}}$ is given by Eq. (24). $\mathbf{J}_{\text{BH,LT}} : \begin{cases} \text{Bardeen-Petterson effect (Eq. 36)} & \text{if } f_{\text{Edd},16} \leq \hat{f}_{\text{Edd},16} \\ \text{Inner precessing thick disc (Eq. 41)} & \text{if } f_{\text{Edd},16} > \hat{f}_{\text{Edd},16} \end{cases}$ Disc and BH (counter)-align instantaneously if $R_{\text{disc}} < R_{\text{warp}}$ (Eq. 27).
Self-gravitating mass (Sec. 2.5)	We limit $M_{\text{disc}} \leq M_{\text{sg}}$, where $M_{\text{sg}} = M_{\text{disc}}(R = R_{\text{sg}})$. R_{sg} is given by Eq. (48).
Radiative efficiency (Sec. 2.6)	Eqs (49)–(52) are utilised to compute the radiative efficiency.

model by incorporating an analytical advection-dominated inflow-outflow solution (ADIOS; Blandford & Begelman 1999, 2004) to account for lower mass accretion rates ($f_{\text{Edd},16} \lesssim 0.01$).

In our model, we focus instead on the super-Eddington regime and employ simulation results from K18, alongside a more detailed thin α -disc model from K08 [that includes also the inner regions (a) and (b), introduced in Section 2.2], to develop an accretion disc model also applicable to super-Eddington accretion.

Our model builds upon that of C21, which itself extends from that of Fiacconi et al. (2018). Table 1 illustrates a summary of our accretion disc-based BH growth sub-grid model for super-Eddington accretion. It outlines the methods used to compute the disc structure (Section 2.2), BH mass accretion rate (Section 2.3), angular momentum evolution (Section 2.4), self-gravitating conditions (Section 2.5), and radiative efficiency (Section 2.6). The differences between our model and that of C21 are detailed in Appendix A.

2.2 Accretion disc structure

We begin defining the relevant length-scales of the accretion disc, moving from the BH outwards. We first set the radius of the ISCO, R_{ISCO} , as the inner boundary of the accretion disc. Following Bardeen et al. (1972), R_{ISCO} is calculated as

$$\frac{R_{\text{ISCO}}}{R_g} = 3 + Z_2 \mp \sqrt{(3 - Z_1)(3 + Z_1 + 2Z_2)}, \quad (4)$$

where $R_g = GM_{\text{BH}}/c^2$ is the gravitational radius of the BH, the upper and lower signs indicate orbits that are prograde and retrograde relative to the BH spin, respectively, and Z_1 and Z_2 are two functions of a_{BH} :

$$Z_1(a_{\text{BH}}) = 1 + (1 - a_{\text{BH}}^2)^{1/3} \left[(1 + a_{\text{BH}})^{1/3} + (1 - a_{\text{BH}})^{1/3} \right], \quad (5)$$

$$Z_2(a_{\text{BH}}) = \sqrt{3a_{\text{BH}}^2 + Z_1^2(a_{\text{BH}})}. \quad (6)$$

Photon-trapping plays a crucial rule for super-Eddington accretion (Begelman 1978). In the inner parts of the disc, photons can become trapped in the radial flow and are unable to escape from the disc surface, eventually being accreted by the BH. This occurs when the photon diffusion time-scale, t_{diff} , exceeds the accretion time-scale in the (cylindrical) radial direction, $t_{\text{acc},R}$. Following K08, we define $t_{\text{diff}} = 3H\tau/c$, where τ is the vertical optical depth in the disc, and $t_{\text{acc},R} = R/|v_R|$, where v_R is the radial velocity. Here, $\tau = \kappa_{\text{es}}\Sigma/2$, where $\kappa_{\text{es}} = 0.20(1 + X) \text{ cm}^2 \text{ g}^{-1}$ is the electron scattering opacity. We assume a hydrogen mass fraction $X = 1$ to calculate κ_{es} (as in K08), the exact value of which does not significantly affect the results (Frank et al. 2002). The photon-trapping radius, R_{trap} , is defined as the radius where the photon diffusion time-scale equals the accretion time-scale. To derive this, we employ the continuity equation to obtain

$$\frac{R_{\text{trap}}}{R_g} = 48 f_{\text{Edd},16} \left(\frac{H}{R} \right). \quad (7)$$

Based on results from two-dimensional (2D) radiation hydrodynamics (RHD) simulations of super-Eddington accretion flows in Kitaki et al. (2021), we set $H/R = 1$. Photons within R_{trap} are accreted onto the BH instead of escaping from the accretion disc. If $f_{\text{Edd},16} \lesssim 0.1$, R_{trap} would become smaller than R_{ISCO} . In this case, the photon-trapping region cannot exist stably and we assume that it disappears if $R_{\text{trap}} < R_{\text{ISCO}}$.

For $R < R_{\text{trap}}$, the assumptions underlying the thin α -disc break down, as the flow is radiatively inefficient and the advection of the photon entropy becomes significant. The slim

disc model accounts for the photon advection and constructs a 1D, stable, and steady accretion disc model (Abramowicz et al. 1988). Although approximate analytical solutions have been derived (Wang & Zhou 1999; Watarai 2006), the multi-dimensional motion and outflows driven by strong radiation pressure are not considered in the slim disc model.

K18 performed 2D RHD simulations of super-Eddington accretion flows with outflows around a non-spinning BH, assuming a constant $\alpha_{0.1} = 1$. They were the first to obtain fitting formulae for the structure of super-Eddington accretion discs covering a wide range of values of $M_{\text{BH,acc}}$ and M_{BH} . We employ these fitting formulae to establish the inner structure of the accretion disc for $R < R_{\text{trap}}$.

For $R > R_{\text{trap}}$, we assume that the accretion disc structure follows the solutions of the thin α -disc model. This assumption is supported by both analytical and simulation results (Watarai 2006; Kitaki et al. 2021). The pressure of the accretion disc can be written as $P = P_{\text{rad}} + P_{\text{gas}}$, where P_{rad} and P_{gas} are the radiation and gas pressure, respectively. In this work, we assume that the gas temperature is above 10^4 K, so that the disc opacity, κ , is dominated by two sources: electron scattering opacity, κ_{es} , and free-free absorption opacity, $\kappa_{\text{ff}} \propto T^{-7/2}$, but we refer to Section 5.2.3 for a discussion on the validity of this assumption. The thin α -disc model is further divided into three regions based on the dominant sources of opacity and pressure (Shakura & Sunyaev 1973; K08):

- Region (a) – the inner region. This region has the highest temperature amongst the three: radiation pressure dominates ($P \sim P_{\text{rad}}$) and electron scattering is the primary opacity source ($\kappa \sim \kappa_{\text{es}}$). This region exists between $\max(R_{\text{ISCO}}, R_{\text{trap}}) \leq R < R_{\text{ab}}$, where R_{ISCO} , R_{trap} , and R_{ab} are defined by Equations (4), (7), and (8), respectively.
- Region (b) – the middle region. Gas pressure dominates ($P \sim P_{\text{gas}}$) and electron scattering remains the primary source of opacity ($\kappa \sim \kappa_{\text{es}}$). This region exists between $R_{\text{ab}} \leq R < R_{\text{bc}}$, where R_{bc} is defined by Equation (9).
- Region (c) – the outer region. Gas pressure dominates ($P \sim P_{\text{gas}}$) and free-free absorption becomes the primary source of opacity ($\kappa \sim \kappa_{\text{ff}}$). This region extends beyond $R \geq R_{\text{bc}}$.

Following K08, the transitions between the different regions of the thin α -disc occur at the characteristic radii⁵

$$\frac{R_{\text{ab}}}{R_g} = 1.12 \times 10^3 M_{\text{BH},6}^{2/21} \alpha_{0.1}^{2/21} f_{\text{Edd},16}^{16/21}, \quad (8)$$

$$\frac{R_{\text{bc}}}{R_g} = 3.15 \times 10^4 f_{\text{Edd},16}^{2/3}. \quad (9)$$

Unlike in Koudmani et al. (2024), we neglect an additional transition radius, $R_{\text{tran}}/R_g \sim 6 (1.25 \times 10^{-2}/f_{\text{Edd},16})^2$, below which the thin α -disc model breaks down (Liu et al. 1999; Yuan et al. 2018). For $R < R_{\text{tran}}$, the disc becomes radiatively inefficient due to low gas density and to extended cooling time. This region can instead be better described by

the ADIOS solution or by an advection-dominated accretion flow (ADAF; Narayan & Yi 1994, 1995a,b; Abramowicz et al. 1995; Chen et al. 1995). The value of R_{tran} is inversely correlated with $f_{\text{Edd},16}$, with the ADAF and ADIOS models becoming more relevant at lower mass accretion rates. We neglected the impact of R_{tran} in our model, since it remains smaller than R_{ISCO} for $f_{\text{Edd},16} \gtrsim 0.01$. Situations involving low accretion rates, for which the ADAF or ADIOS models become significant, are beyond the scope of this study.

Unlike R_{tran} , the radii R_{trap} , R_{ab} , and R_{bc} are all positively correlated with the mass accretion rate, because a higher mass accretion rate increases T , enhancing the importance of radiation pressure and electron scattering opacity. As a result, at intermediate mass accretion rates, only region (c) of the thin α -disc remains dominant, as the other regions shrink significantly in comparison. Consequently, most accretion disc-based BH growth sub-grid models consider only region (c) when describing the disc structure (e.g. see footnote 1 in Fiacconi et al. 2018). However, for super-Eddington accretion, the contribution from the inner regions may become non-negligible (see the top two panels of Figure 1), necessitating the inclusion of all three regions of the thin α -disc in our model.

Finally, we define the self-gravitating radius, R_{sg} , beyond which the accretion disc is assumed to fragment due to self-gravity. Accordingly, we impose the condition that $R_{\text{disc}} \leq R_{\text{sg}}$. R_{sg} is determined using the Toomre (1964) parameter $Q(R) = \Omega_K c_s / (\pi G \Sigma)$. We define R_{sg} as the radius where $Q(R_{\text{sg}}) = Q_{\text{min}}$, with $Q_{\text{min}} \sim \mathcal{O}(1)$ is a constant that can be set in the code and determines the maximum size of the disc. The self-gravitating mass is defined as $M_{\text{sg}} = M_{\text{disc}}(R_{\text{disc}} = R_{\text{sg}})$. A detailed calculation of R_{sg} and M_{sg} is provided in Section 2.5.

To model the inner accretion disc structure, we adopt the fitting formulae from simulation results of K18 to compute the surface gas density, Σ_{trap} , and specific angular momentum, L_{trap} , in the photon-trapping region of the accretion disc, where $R < R_{\text{trap}}$:

$$\Sigma_{\text{trap}} = \frac{\dot{M}_{\text{BH,accr}}}{2\pi R v_R} = 222 f_{\text{Edd},16}^{0.98} \left(\frac{R}{R_g} \right)^{0.11} \text{ g cm}^{-2}, \quad (10)$$

$$\begin{aligned} L_{\text{trap}} &= 1.27 f_{\text{Edd},16}^{0.01} \left(\frac{GM_{\text{BH}}}{c} \right) \left(\frac{R}{R_g} \right)^{0.4} \\ &= 5.622 \times 10^{21} M_{\text{BH},6} f_{\text{Edd},16}^{0.01} \left(\frac{R}{R_g} \right)^{0.4} \text{ cm}^2 \text{ s}^{-1}. \end{aligned} \quad (11)$$

Watarai (2006) derived an analytical formula for the slim disc model, predicting a surface density profile of $\Sigma \propto R^{-0.5}$ in the photon-trapping region. The slope is negative in Watarai (2006), whereas it is positive in K18. The discrepancy may be attributed to the presence of large-scale circulation and outflows observed in the 2D simulations of K18, which are not included in the analytical model.

Śądowski (2011) calculated 1D numerical solutions for the relativistic slim disc model. For $f_{\text{Edd},16} = 10$ and $R < 200 R_g < R_{\text{trap}}$, their results indicate a slightly larger specific angular momentum and a steeper surface density profile compared to those of K18. The discrepancy may be attributed to the inclusion of general relativistic (GR) effects considered in

⁵ We note that R_{bc} in K08 is nearly identical to that given by Shakura & Sunyaev (1973), but R_{ab} is approximately three times larger than that of Shakura & Sunyaev (1973). The differences arise from slight variations in definitions (see Appendix B for further details).

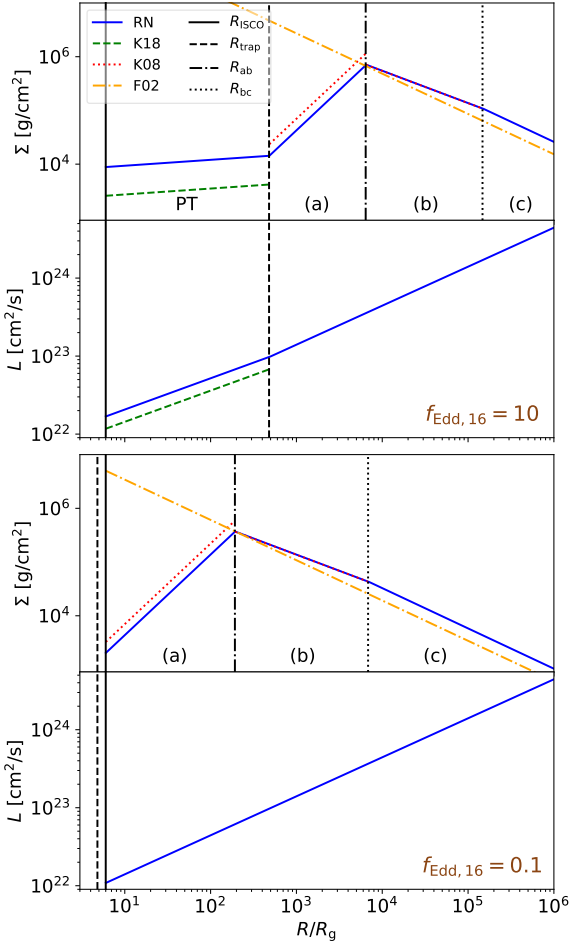


Figure 1. Surface density profile (first and third panels) and specific angular momentum profile (second and fourth panels) for accretion discs with $f_{\text{Edd},16} = 10$ and 0.1 , assuming $M_{\text{BH},6} = 1$, $\alpha_{0.1} = 1$, and $a_{\text{BH}} = 0$. The blue solid lines represent the profile constructed using our model, renormalised to ensure continuity (RN in the figure). The green dashed lines correspond to the fitting formulae from K18, i.e. Equations (10) and (11). The red dotted lines show the surface density profile of regions (a) and (b) from K08, i.e. Equations (12) and (13). We also plot the surface density profile from Frank et al. (2002), which includes only region (c) of the thin α -disc and has been commonly used in previous sub-grid models. The black vertical lines in the first and third panels indicate R_{ISCO} (solid), R_{trap} (dashed), R_{ab} (dashed-dotted), and R_{bc} (dotted). The black vertical lines in the second and fourth panels indicate R_{ISCO} and R_{trap} . For $f_{\text{Edd},16} = 0.1$, $R_{\text{trap}} < R_{\text{ISCO}}$, meaning that the photon-trapping region does not exist. Texts “PT”, “(a)”, “(b)”, and “(c)” indicate the photon-trapping region and regions (a), (b), and (c) of the disc, respectively. The value of R_{tran}/R_g , which is 10^{-5} for $f_{\text{Edd},16} = 10$ and 10^{-1} for $f_{\text{Edd},16} = 0.1$, is not shown in this figure due to its small value. R_{sg}/R_g (for $Q_{\text{min}} = 1$) is equal to 4×10^4 [in region (b)] and 2.9×10^5 [in region (c)] for $f_{\text{Edd},16} = 10$ and 0.1 , respectively.

Sądowski (2011). Furthermore, K18 consider a 2D flow with outflows, which may further contribute to the differences.

Following K08, we obtain the asymptotic limits of the surface density profile for the three regions of the thin α -disc around a non-spinning BH by assuming that the pressure is

dominated by either P_{gas} or P_{rad} and the opacity κ is dominated by either κ_{es} or κ_{ff} :

$$\Sigma_a = 21.9 \alpha_{0.1}^{-1} f_{\text{Edd},16}^{-1} \left(\frac{R}{R_g} \right)^{3/2} f^{-1} \text{ g cm}^{-2}, \quad (12)$$

$$\Sigma_b = 3.45 \times 10^7 \alpha_{0.1}^{-4/5} M_{\text{BH},6}^{1/5} f_{\text{Edd},16}^{3/5} \left(\frac{R}{R_g} \right)^{-3/5} f^{3/5} \text{ g cm}^{-2}, \quad (13)$$

$$\Sigma_c = 1.67 \times 10^8 \alpha_{0.1}^{-4/5} M_{\text{BH},6}^{1/5} f_{\text{Edd},16}^{7/10} \left(\frac{R}{R_g} \right)^{-3/4} f^{7/10} \text{ g cm}^{-2}, \quad (14)$$

where $f = 1 - \sqrt{6R_g/R}$, and we assume $f = 1$ for simplicity, since its value differs from unity only very close to the ISCO radius. Σ_a , Σ_b , and Σ_c are the surface (gas) densities of regions (a), (b), and (c), respectively. Keplerian angular momentum is assumed in all three regions of the thin α -disc:

$$\begin{aligned} L_K &= \left(\frac{GM_{\text{BH}}}{c} \right) \left(\frac{R}{R_g} \right)^{0.5} \\ &= 4.427 \times 10^{21} M_{\text{BH},6} \left(\frac{R}{R_g} \right)^{0.5} \text{ cm}^2 \text{ s}^{-1}. \end{aligned} \quad (15)$$

To construct the surface density profile of the entire accretion disc, we first compute the surface density using Equation (14) for region (c) of the thin α -disc, where $R > R_{\text{bc}}$. In all inner regions, we renormalise the surface density profile for each region to ensure continuity at the boundaries. This approach results in a continuous surface density profile without abrupt transitions between different regions. When the mass accretion rate is low, the structure of the accretion disc is dominated by region (c), as the other regions significantly decrease in size (Equation 9). Therefore, during renormalisation, we preserve the exact results in region (c) rather than in other regions. This ensures that the surface density profile remains accurate at low mass accretion rates and maintain consistency with other accretion disc-based sub-grid models that consider only region (c) of the α -disc. We apply the same method even when $R_{\text{disc}} < R_{\text{bc}}$, such that the construction always starts from region (c), with a cut-off applied at R_{disc} .⁶ We apply a similar procedure for the specific angular momentum profile and apply the renormalisation also to the photon-trapping region. Hereafter, unless otherwise stated, all surface density and specific angular momentum profiles used in the calculations are the renormalised ones.

In the top two panels of Figure 1, we show the (renormalised) surface density and specific angular momentum profiles for $f_{\text{Edd},16} = 10$ (i.e. $f_{\text{Edd},\eta}/\eta_{0.1} = 16$ in the equations of C21), with $\alpha_{0.1} = 1$, $M_{\text{BH},6} = 1$, and $a_{\text{BH}} = 0$. The panels also include the surface density and specific angular momentum profiles without renormalisation (i.e. the exact Equations 10, 11, 12, and 13). For comparison, we also plot the

⁶ We have tested that applying this renormalisation does not affect the BH mass evolution. Moreover, R_{disc} is always greater than R_{ab} (see Section 2.3 for the cause) and the renormalisation of region (b) is minimal (see Figure 1).

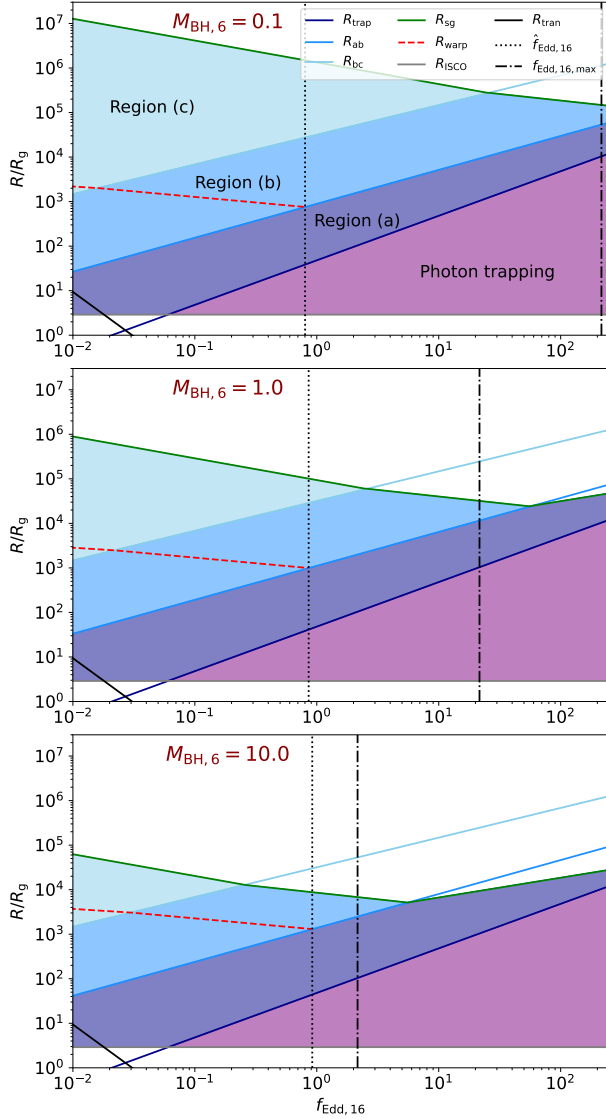


Figure 2. Characteristic radii as a function of $f_{\text{Edd},16}$ for different values of M_{BH} : R_{trap} (dark blue line), R_{ab} (medium blue line), R_{bc} (light blue line), R_{sg} (green line), R_{ISCO} (grey line), and R_{tran} (solid black line). The warp radius (R_{warp} , red dashed line) is defined in Section 2.4. The top, middle, and bottom panels correspond to $M_{\text{BH},6} = 0.1, 1$, and 10 , respectively, with $\alpha_{0.1} = 1$, $Q_{\text{min}} = 1$, and $a_{\text{BH}} = 0.8$ (prograde disc). The shaded regions indicate the parameter space corresponding to different disc regions. The vertical black dotted lines represent $\hat{f}_{\text{Edd},16}$, the critical value of $f_{\text{Edd},16}$ distinguishing the two torque models (see Section 2.4 for more details). The vertical black dashed-dotted lines represent $f_{\text{Edd},16,\text{max}}$ (defined in Section 2.3), assuming $M_{\text{disc}} = M_{\text{sg}}$.

surface density profile of region (c) of the thin α -disc from Frank et al. (2002), which is commonly used to describe the thin α -disc in sub-grid models (e.g. Perego et al. 2009; Fiaccconi et al. 2018; C21; Koudmani et al. 2024). However, in our model, we refer to K08 for the thin α -disc model, as it provides detailed equations for all three regions of the thin α -disc. Notably, the surface density in region (c) of K08 is approximately 1.7 times higher than that in Frank et al. (2002). This discrepancy arises from differences in definitions and opacity values adopted in the two references (see Appendix B

for further details, wherein we also compare these two models to the original model by Shakura & Sunyaev 1973).

While the differences between the renormalised surface density and the original surface density equations in regions (a) and (b) of the thin α -disc model are relatively small, they become non-negligible in the photon-trapping region. For example, the surface density can differ by a factor of a few, as seen in the top two panels of this figure. One possible explanation for this discrepancy is that the effective α might change in this region, due to the strong photon advection (e.g. Jiang et al. 2019). Another is the inclusion of outflows in the simulations of K18. By contrast, the discrepancy in specific angular momentum is much smaller compared to the surface density profile.

In the bottom two panels of the same figure, we present the case of a lower Eddington ratio, $f_{\text{Edd},16} = 0.1$ (i.e. $f_{\text{Edd},\eta}/\eta_{0.1} = 0.16$). In this scenario, $R_{\text{trap}} < R_{\text{ISCO}}$, indicating that the photon-trapping region is absent. Additionally, regions (a) and (b) shift significantly inwards within the disc, as lower accretion rates lead to weaker radiation pressure and a reduced dominance of electron scattering opacity.

Note that, in general, our renormalisation does not significantly affect the total mass and angular momentum of the disc, as these are dominated by the outer parts of the accretion disc – typically corresponding to region (b) or region (c) – due to their much larger area (proportional to R^2).

In reality, both the surface density profile and the specific angular momentum profile should not only be continuous but also smooth. Although transitions between different regions should ideally be smooth rather than exhibiting discontinuous changes in slopes, we neglect this issue due to the difficulty in determining the exact values of Σ and L (and related quantities) at these transitions. For instance, at $R \sim R_{\text{ab}}$, both P_{gas} and P_{rad} contribute significantly to the total pressure, making it challenging to derive a simple analytical solution. Instead, we ensure continuity in the profiles while acknowledging that a fully smooth transition would require a more detailed treatment of the disc structure (e.g. Hure et al. 1994a; Derdzinski & Mayer 2023; Gangardt et al. 2024).

Figure 2 illustrates the characteristic radii as a function of $f_{\text{Edd},16}$, for a few different values of BH mass, with each shaded region indicating the parameter space corresponding to a specific disc region. For example, consider a BH with $M_{\text{BH},6} = 1$: when $f_{\text{Edd},16} \gtrsim 2.5$, region (c) of the accretion disc vanishes, since $R_{\text{bc}} > R_{\text{sg}}$. This supports our claim that at higher mass accretion rates, the contributions of the inner regions of the accretion disc become increasingly significant.

2.3 Mass accretion

At each time step, the growth rates of M_{BH} and M_{disc} , denoted as $\dot{M}_{\text{BH,growth}}$ and \dot{M}_{disc} , respectively, are calculated using the following equations:

$$\dot{M}_{\text{BH,growth}} = (1 - \eta) \dot{M}_{\text{BH,accr}} , \quad (16)$$

$$\dot{M}_{\text{disc}} = \dot{M}_{\text{in}} - \dot{M}_{\text{BH,accr}} - \dot{M}_{\text{out}} , \quad (17)$$

where the term $(1 - \eta)$ represents the fraction of mass that

is effectively accreted onto the BH due to radiative losses.⁷ The mass outflow rate due to BH feedback, \dot{M}_{out} , is set to zero in this work, as we do not consider BH feedback. The mass accretion rate onto the disc, \dot{M}_{in} , is determined by the gas dynamics on resolved scales.

Instead of using the BHL prescription for $\dot{M}_{\text{BH,accr}}$ (as in, e.g. [Dubois et al. 2014](#); [Bustamante & Springel 2019](#); [Masonneau et al. 2023b](#); [Sala et al. 2024](#); [Huško et al. 2025](#)), which neglects the influence of angular momentum transport on accretion disc scales, we update $\dot{M}_{\text{BH,accr}}$ using an accretion disc-mediated accretion rate ([Fiacconi et al. 2018](#)). Since the accretion disc is unresolved in the simulation, $\dot{M}_{\text{BH,accr}}$ is determined based on integrated properties of the disc, M_{disc} and J_{disc} , within a sub-grid model. For instance, equation (5) in [C21](#) (see also equations 2 and A5 in [Fiacconi et al. 2018](#)) describes the relation between M_{disc} , J_{disc} , and $f_{\text{Edd},\eta}$. However, these relations are derived under the assumption that the whole accretion disc follows the region (c) solution of the thin α -disc model, which is not consistent with the multi-region disc structure considered in this work.

Within our more complex disc model, it is not feasible any longer to derive a simple analytic equation relating $f_{\text{Edd},16}$ to M_{disc} and J_{disc} , as was done in previous works. Instead, we first calculate M_{disc} and J_{disc} via numerical integration using the following equations:

$$M_{\text{disc}} = 2\pi \int_{R_{\text{ISCO}}}^{R_{\text{disc}}} \Sigma(R, f_{\text{Edd},16}) R dR, \quad (18)$$

$$J_{\text{disc}} = 2\pi \int_{R_{\text{ISCO}}}^{R_{\text{disc}}} \Sigma(R, f_{\text{Edd},16}) L(R, f_{\text{Edd},16}) R dR. \quad (19)$$

For simplicity, we assume $R_{\text{ISCO}} = 0$ when performing the integration. These integrations allow us to determine M_{disc} and J_{disc} as functions of $f_{\text{Edd},16}$ and R_{disc} . We then apply the Newton-Raphson method to invert these two functions numerically and compute $f_{\text{Edd},16}$ from given values of M_{disc} and J_{disc} . The initial guess for the Newton-Raphson method is taken as the $f_{\text{Edd},16}$ and R_{disc} values from the previous time step.

However, the Newton-Raphson method fails to compute $f_{\text{Edd},16}$ when multiple or no solutions exist for a given pair of M_{disc} and J_{disc} values. As shown in Appendix C, degeneracies arise when region (a) dominates the disc structure instead of regions (b) or (c), leading to multiple or no valid solutions of $f_{\text{Edd},16}$ for the same $(M_{\text{disc}}, J_{\text{disc}})$. To address this, we define an upper limit for the Eddington ratio, given by

$$f_{\text{Edd},16,\text{max}} = 21.6 M_{\text{BH},6}^{-1} \alpha_{0.1}^{4/10} Q_{\text{min}}^{-7/10} \left(\frac{M_{\text{disc}}}{M_{\text{sg}}} \right)^{3/5}. \quad (20)$$

To prevent degeneracies, we impose the constraint $f_{\text{Edd},16} \leq f_{\text{Edd},16,\text{max}}$, as exceeding this limit would lead to degeneracy due to region (a) dominating the accretion disc structure.

Many previous sub-grid models that do not account for

super-Eddington accretion impose an upper limit on the Eddington ratio, capping it below a value close to unity to prevent super-Eddington accretion (e.g. [Power et al. 2011](#); [Dubois et al. 2014](#); [Fiacconi et al. 2018](#); [Bustamante & Springel 2019](#); [C21](#)). In contrast, our model introduces a new cap at $f_{\text{Edd},16,\text{max}}$, which is approximately 20 for $M_{\text{BH},6} = 1$ (and $M_{\text{disc}} = M_{\text{sg}}$). However, we caution that for more massive BHs ($M_{\text{BH}} \gtrsim 10^8 M_{\odot}$), $f_{\text{Edd},16,\text{max}} \lesssim 1$. Additionally, previous sub-grid models that consider only region (c) of the thin α -disc solution might become inaccurate when $f_{\text{Edd},16} > f_{\text{Edd},16,\text{max}}$, as the disc should instead be dominated by region (a), which has significantly different structural properties (see Figure 1).

2.4 Angular momentum evolution

In this section, we describe the evolution of the BH angular momentum due to gas accretion at R_{ISCO} (see Section 2.4.1) and the Lense-Thirring effect. The evolution of the angular momentum of the BH is given by

$$\dot{\mathbf{J}}_{\text{BH}} = \dot{\mathbf{J}}_{\text{BH,acc}} + \dot{\mathbf{J}}_{\text{BH,LT}}, \quad (21)$$

where $\dot{\mathbf{J}}_{\text{BH,acc}}$ represents the change in angular momentum due to accretion and $\dot{\mathbf{J}}_{\text{BH,LT}}$ is the Lense-Thirring torque. We adopt two different models to compute the Lense-Thirring torque, for low and high mass accretion rates (see Section 2.4.2).

Due to the conservation of angular momentum, \mathbf{J}_{disc} evolves according to

$$\dot{\mathbf{J}}_{\text{disc}} = -\dot{\mathbf{J}}_{\text{BH}} + \dot{\mathbf{J}}_{\text{in}}, \quad (22)$$

where $\dot{\mathbf{J}}_{\text{in}}$ is the angular momentum inflow onto the accretion disc from resolved scales.

2.4.1 Accretion

The specific angular momentum at R_{ISCO} , denoted as Λ_{ISCO} , depends on a_{BH} and M_{BH} . Following [Bardeen et al. \(1972\)](#), it is computed using

$$\Lambda_{\text{ISCO}}(a_{\text{BH}}) = \pm \frac{GM_{\text{BH}}}{c\lambda} \frac{\lambda^2 \mp 2a_{\text{BH}}\sqrt{\lambda} + a_{\text{BH}}^2}{(\lambda - 3 \pm 2a_{\text{BH}}/\sqrt{\lambda})^{1/2}}, \quad (23)$$

where $\lambda = R_{\text{ISCO}}/R_{\text{g}}$ (given by Equation 4), and the upper and lower signs correspond to a prograde and retrograde disc, respectively. The evolution of the BH angular momentum due to accretion is given by

$$\dot{\mathbf{J}}_{\text{BH,acc}} = \dot{M}_{\text{BH}} \Lambda_{\text{ISCO}} \frac{\dot{\mathbf{J}}_{\text{BH}} \cdot \dot{\mathbf{J}}_{\text{disc}}}{|\dot{\mathbf{J}}_{\text{BH}} \cdot \dot{\mathbf{J}}_{\text{disc}}|} \dot{\mathbf{J}}_{\text{BH}}. \quad (24)$$

Following [C21](#), the disc is depleted if $J_{\text{disc}}/M_{\text{disc}} < \Lambda_{\text{ISCO}}$. In such cases,⁸ it is refilled stochastically through inflows from the surrounding gas. However, in the simulations presented in this paper, such depletion never occurs.

⁸ For example, when there is no gas inflow from the surroundings, or in very special configurations (e.g. [Fiacconi et al. 2018](#); [C21](#)).

⁷ In the common case wherein only the BH is modelled (i.e. with no accretion disc), the BH growth rate should be $\dot{M}_{\text{BH,growth}} = (1 - \eta_{\text{m}}) \dot{M}_{\text{BH,accr}}$, where $\eta_{\text{m}} \geq \eta$ is the fraction of mass-energy released by accretion in any form (e.g. [Volonteri et al. 2015](#); [Capelo et al. 2023](#)). In our model, $\eta_{\text{m}} = \eta$, as any mass loss due to feedback is described by \dot{M}_{out} .

2.4.2 The Lense-Thirring effect

The spinning BH induces Lense-Thirring precession on the surrounding accretion disc. The precession frequency, ω_{LT} , is given by (Lense & Thirring 1918)

$$\omega_{\text{LT}} = \frac{2GJ_{\text{BH}}}{c^2 R^3}. \quad (25)$$

The response of the disc to Lense-Thirring precession depends on the parameters α and H/R . For a thin disc ($\alpha > H/R$), the system lies in the diffusive regime, in which the warp is communicated through the vertical viscosity, ν_2 , related to ν_1 via Equation (3). It is important to note that ξ is a function of α (Lodato & Pringle 2007). For larger values of α , ξ can increase to around 1. We adopt $\xi = 0.7$ in this study, as it is more appropriate for $\alpha_{0.1} = 1$ (as in C21). In this regime, the precessional motion is damped by the vertical viscosity.

When $\alpha < H/R$, the disc enters the wave-like regime, wherein bending waves effectively communicate the warp because the sound-crossing time-scale becomes shorter than the vertical viscous time-scale, rendering the effect of vertical viscosity negligible (see the reviews by Ingram & Motta 2019; Fragile & Liska 2024). In this regime, if the outer boundary of the disc is misaligned with the BH, the entire region remains misaligned and undergoes solid-body precession. Beyond the bending wave radius, $R_{\text{bw}} = 6(H/R)^{-4/5} a_{\text{BH}}^{2/5} R_g$, bending waves propagate smoothly, maintaining a nearly constant tilt angle. However, for $R < R_{\text{bw}}$, the wavelength of these waves depends strongly on radius, leading to significant variations in the tilt angle. GR magnetohydrodynamics (GRMHD) simulations suggest that this effect can induce a substantial decrease in density within this region (Fragile et al. 2009; Ingram et al. 2009).

In our accretion disc model, the photon-trapping region lies in the wave-like regime, since it is geometrically thick ($H/R = 1$), whereas all three regions of the thin α -disc are in the diffusive regime.

Within the diffusive regime, we qualitatively estimate the shape of the disc by considering the balance between the Lense-Thirring torque and vertical shear. Following equations (1) and (9) in Martin et al. (2007), the torque induced by the Lense-Thirring precession on the disc at radius R is given by $\tau_{\text{LT}} = -\omega_{\text{LT}} \Sigma \mathbf{j}_{\text{BH}} \times \mathbf{L}$, whereas the vertical shear exerted by the vertical viscosity is $\tau_{\text{visc}} = \frac{1}{R} \frac{\partial}{\partial R} \left(\frac{1}{2} R \nu_2 \Sigma L \frac{\partial l}{\partial R} \right)$. The equilibrium state of the warped disc is reached when $\tau_{\text{visc}} = \tau_{\text{LT}}$. To characterise the relative strength of the vertical shear and the Lense-Thirring torque, we introduce the dimensionless parameter \mathcal{A} :

$$\mathcal{A} = \frac{\frac{1}{R^2} \frac{1}{2} R \nu_2 \Sigma \frac{L}{R}}{\omega_{\text{LT}} \Sigma L} = \frac{\nu_2}{2\omega_{\text{LT}} R^2} = \frac{c^2}{4GJ_{\text{BH}}} \nu_2(R) R. \quad (26)$$

If $\nu_2(R)$ is a continuous and monotonically increasing function, then $\mathcal{A} > 1$ in the outer part of the disc and $\mathcal{A} < 1$ in the inner part. This implies that the inner region of the disc is governed by the Lense-Thirring torque and aligns with the BH, while the outer region remains misaligned due to the relatively weaker Lense-Thirring torque. This configuration is also known as the Bardeen-Petterson effect (Bardeen & Petterson 1975; Papaloizou & Pringle 1983; Nealon et al. 2015; Liska et al. 2019). A smooth transition occurs around

the warp radius, R_{warp} , which is defined by the condition $\mathcal{A}(R = R_{\text{warp}}) = 1$.⁹

For simplicity, we first assume a power law expression for ν_1 : $\nu_1 = CR^\beta$. Using this assumption, we derive R_{warp} based on its definition:

$$R_{\text{warp}} = \frac{4GJ_{\text{BH}}}{c^2 \nu_2(R_{\text{warp}})} = \left(\frac{8G^2 M_{\text{BH}}^2 a_{\text{BH}} \alpha^2}{\xi C c^3} \right)^{1/(1+\beta)}. \quad (27)$$

We use this equation to reformulate \mathcal{A} in terms of R_{warp} :

$$\mathcal{A} = \left(\frac{R}{R_{\text{warp}}} \right) \left(\frac{\nu_2}{\nu_2(R_{\text{warp}})} \right) = \left(\frac{R}{R_{\text{warp}}} \right)^{1+\beta}. \quad (28)$$

For instance, consider an accretion disc composed only of region (c) of the thin α -disc (i.e. $\beta = 3/4$). The corresponding warp radius, $R_{\text{warp,c}}$, and the dimensionless parameter, \mathcal{A}_c , can be determined using Equations (27) and (28). The same method is applicable also to regions (a) and (b):¹⁰

$$\frac{R_{\text{warp,a}}}{R_g} = 9.18 \times 10^2 \xi^2 \alpha_{0.1}^{-2} a_{\text{BH}}^{-2} f_{\text{Edd},16}^4, \quad (29)$$

$$\frac{R_{\text{warp,b}}}{R_g} = 8.78 \times 10^2 \xi^{-5/8} M_{\text{BH},6}^{1/8} \alpha_{0.1}^{3/4} a_{\text{BH}}^{5/8} f_{\text{Edd},16}^{-1/4}, \quad (30)$$

$$\frac{R_{\text{warp,c}}}{R_g} = 1.19 \times 10^3 \xi^{-4/7} M_{\text{BH},6}^{4/35} \alpha_{0.1}^{24/35} a_{\text{BH}}^{4/7} f_{\text{Edd},16}^{-6/35}, \quad (31)$$

$$\mathcal{A}_a = \left(\frac{R}{R_{\text{warp,a}}} \right)^{-1/2}, \quad (32)$$

$$\mathcal{A}_b = \left(\frac{R}{R_{\text{warp,b}}} \right)^{8/5}, \quad (33)$$

$$\mathcal{A}_c = \left(\frac{R}{R_{\text{warp,c}}} \right)^{7/4}. \quad (34)$$

We then use the above equations to characterise the alignment behaviour of the accretion disc in our model. In region (a), $\mathcal{A}(R)$ decreases with increasing R , whereas in regions (b) and (c), $\mathcal{A}(R)$ increases with increasing R . Since \mathcal{A} is a continuous function after renormalising the surface density and specific angular momentum profiles, its minimum value occurs at $R = R_{\text{ab}}$. If $\min(\mathcal{A}) = \mathcal{A}(R_{\text{ab}}) > 1$, the vertical shear generated by viscosity is always more significant than the Lense-Thirring torque throughout the disc. Therefore, the disc does not reach the Bardeen-Petterson configuration and remains misaligned with the BH. This condition is satisfied when $R_{\text{warp,a}} > R_{\text{ab}}$ and $R_{\text{warp,b}} < R_{\text{ab}}$. Conversely, if $\min(\mathcal{A}) = \mathcal{A}(R_{\text{ab}}) < 1$, we assume that the innermost part

⁹ This definition is equivalent to requiring that the Lense-Thirring precession period is comparable to the vertical warp diffusion time-scale: $\omega_{\text{LT}}^{-1}(R_{\text{warp}}) \sim R_{\text{warp}}^2/\nu_2(R_{\text{warp}})$.

¹⁰ Strictly speaking, the warp radius does not exist for region (a), where $\beta = -3/2$. In this case, $\mathcal{A}(R)$ is a decreasing function, meaning that $\mathcal{A} > 1$ in the inner disc, preventing alignment with the BH. Nonetheless, we still calculate $R_{\text{warp,a}}$ and use it to describe $\mathcal{A}_a(R)$ for simplicity. We also note that this approach is not applicable to the photon-trapping region, as it lies in the wave-like regime. Finally, we note that Equations (29)–(31) are not renormalised, but the computations in the code and the results we show are based on their renormalised version. The same applies to Equations (45)–(47).

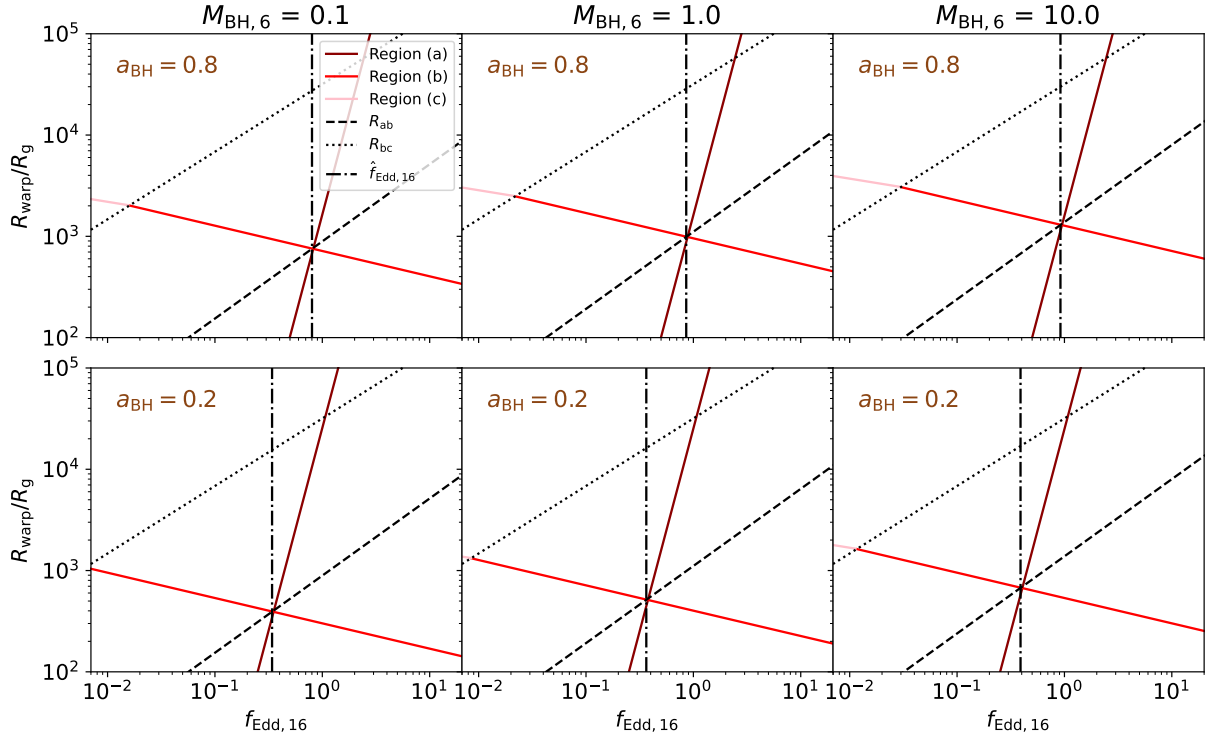


Figure 3. The warp radius, R_{warp} , as a function of $f_{\text{Edd},16}$ for $a_{\text{BH}} = 0.8$ (top row) and 0.2 (bottom row) and $M_{\text{BH},6} = 0.1$ (left-hand column), 1 (central column), and 10 (right-hand column), with $\alpha_{0.1} = 1$ and $\xi = 0.7$. For each region, R_{warp} is calculated by assuming a power-law surface density profile, using Equations (31), (30), and (29), properly readjusted after the renormalisation of the surface density and specific angular momentum profiles. Dark red, red, and pink lines correspond to regions (a), (b), and (c), respectively. Black lines indicate R_{bc} (dotted), R_{ab} (dashed), and $\hat{f}_{\text{Edd},16}$ (dash-dotted). When $f_{\text{Edd},16} < \hat{f}_{\text{Edd},16}$, $R_{\text{warp}} = R_{\text{warp},b}$ if $R_{\text{warp},b} < R_{\text{bc}}$; otherwise, $R_{\text{warp}} = R_{\text{warp},c}$. When $f_{\text{Edd},16} > \hat{f}_{\text{Edd},16}$, $R_{\text{warp},a} > R_{\text{ab}}$ and $R_{\text{warp},b} < R_{\text{ab}}$. In this case, the Bardeen-Petterson configuration cannot be reached. For $f_{\text{Edd},16} > \hat{f}_{\text{Edd},16}$, we extrapolate $R_{\text{warp},b}$ and $R_{\text{warp},a}$ beyond their regions of validity to better illustrate this in the figure.

of region (b) aligns with the BH, since $\mathcal{A} > 1$ there. Consequently, region (b) supplies aligned gas inflow to region (a) and the photon-trapping region, causing them to align with the BH as well.

Figure 3 illustrates R_{warp} (after renormalisation of the surface density and the specific angular momentum) in different regions as a function of $f_{\text{Edd},16}$ for a few values of M_{BH} and a_{BH} (note that this result is the same for prograde/retrograde orbits, since the Lense-Thirring torque has the same magnitude in both cases). We define a critical Eddington ratio, $\hat{f}_{\text{Edd},16}$, such that $R_{\text{warp},b}(\hat{f}_{\text{Edd},16}) = R_{\text{ab}}(\hat{f}_{\text{Edd},16})$. For $f_{\text{Edd},16} < \hat{f}_{\text{Edd},16}$, $R_{\text{warp},b} < R_{\text{ab}}$, which implies $\min(\mathcal{A}) < 1$. This condition allows the system to reach the Bardeen-Petterson configuration. If $f_{\text{Edd},16} \ll \hat{f}_{\text{Edd},16}$, then $R_{\text{warp},b} > R_{\text{bc}}$, meaning that $R_{\text{warp},b}$ cannot lie within region (b). In this case, we assume $R_{\text{warp}} = R_{\text{warp},c}$. Otherwise, if $f_{\text{Edd},16}$ is larger, such that $R_{\text{warp},b}$ lies within region (b), $R_{\text{warp}} = R_{\text{warp},b}$. It is evident that when $f_{\text{Edd},16} > \hat{f}_{\text{Edd},16}$, $R_{\text{warp},a} > R_{\text{ab}}$ and $R_{\text{warp},b} < R_{\text{ab}}$, leading to $\min(\mathcal{A}) > 1$. In this regime, the system cannot achieve the Bardeen-Petterson configuration, and the Lense-Thirring torque is instead generated by precession in the misaligned wave-like photon-trapping region.

Using Equations (8) and (30), we obtain $\hat{f}_{\text{Edd},16} = 0.79 \xi^{-21/34} M_{\text{BH},6}^{1/34} a_{\text{BH}}^{21/34} \alpha_{0.1}^{11/17}$. However, when $a_{\text{BH}} \ll 1$, $\hat{f}_{\text{Edd},16} \ll 1$, leading to $R_{\text{trap}} < R_{\text{ISCO}}$. In this case,

the photon-trapping region disappears. From Equations (4) and (7), the condition $R_{\text{trap}} < R_{\text{ISCO}}$ occurs when $f_{\text{Edd},16} < R_{\text{ISCO}}/(48R_g) = \lambda/48 \sim 0.125$. Here, we assume $R_{\text{ISCO}} \sim 6R_g$, since $a_{\text{BH}} \ll 1$. Consequently, the photon-trapping region disappears when $f_{\text{Edd},16} < 0.125$. If $\hat{f}_{\text{Edd},16} < f_{\text{Edd},16} < 0.125$, the photon-trapping region vanishes, but the disc remain misaligned with the BH. This implies that the torque between the BH and the disc would be extremely weak. For simplicity, we assume that the Lense-Thirring torque in this regime still follows the Bardeen-Petterson configuration. Given that $a_{\text{BH}} \ll 1$, the Lense-Thirring torque is weak and it would not significantly affect the results. Thus, we redefine the critical value for $f_{\text{Edd},16}$ as

$$\hat{f}_{\text{Edd},16} = \max \left(0.125, 0.79 \xi^{-21/34} M_{\text{BH},6}^{1/34} a_{\text{BH}}^{21/34} \alpha_{0.1}^{11/17} \right). \quad (35)$$

Figure 4 presents $\hat{f}_{\text{Edd},16}$ as a function of a_{BH} for $M_{\text{BH},6} = 0.1, 1$, and 10 . It is evident that the dependence of $\hat{f}_{\text{Edd},16}$ on M_{BH} is minimal, with a_{BH} being the primary factor influencing its value. For a rapidly spinning BH ($a_{\text{BH}} \gtrsim 0.5$), we find that $\hat{f}_{\text{Edd},16} \approx 1$.

When $f_{\text{Edd},16} \leq \hat{f}_{\text{Edd},16}$, we assume that the torque is exerted via the Bardeen-Petterson effect, leading to alignment between the inner disc and the BH spin (see Section 2.4.3).

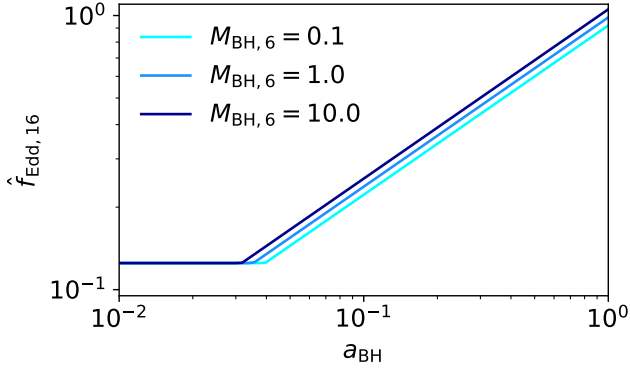


Figure 4. Critical Eddington ratio, $\hat{f}_{\text{Edd},16}$ (Equation 35), as a function of the BH spin parameter, a_{BH} , with $\alpha_{0.1} = 1$ and $\xi = 0.7$. The different curves correspond to $M_{\text{BH},6} = 0.1$ (cyan), 1 (blue), and 10 (dark blue).

Conversely, when $f_{\text{Edd},16} > \hat{f}_{\text{Edd},16}$, the disc remains misaligned with the BH, and the Lense-Thirring torque is instead driven by the inner precessing thick disc (see Section 2.4.4).

2.4.3 Lense-Thirring effect for low mass accretion rates

In this section, we compute the Lense-Thirring effect for $f_{\text{Edd},16} \leq \hat{f}_{\text{Edd},16}$, when the Bardeen-Petterson configuration is achieved. The gravito-magnetic torque exerted by the Lense-Thirring effect in a misaligned disc is derived in Fiacconi et al. (2018), based on the formulation of Martin et al. (2007):

$$\mathbf{j}_{\text{BH,LT}} = -\frac{\mathbf{J}_{\text{BH}}}{t_{\text{gm}}} \times \left\{ \sin\left(\frac{\pi}{7}\right) \mathbf{j}_{\text{disc}} + \cos\left(\frac{\pi}{7}\right) (\mathbf{j}_{\text{BH}} \times \mathbf{j}_{\text{disc}}) \right\}, \quad (36)$$

where t_{gm} represents the characteristic time-scale over which the gravito-magnetic interaction significantly alters the BH spin direction. We re-derive the time-scale using expressions from Fiacconi et al. (2018), assuming that the disc structure follows region (c) of the thin α -disc as described in K08:

$$t_{\text{gm}} \simeq 9.5 \times 10^{-2} \xi^{-5/7} \alpha_{0.1}^{58/35} M_{\text{BH},6}^{-2/35} a_{\text{BH}}^{5/7} f_{\text{Edd},16}^{-32/35} \text{ Myr}. \quad (37)$$

We note that the derivations of $\mathbf{j}_{\text{BH,LT}}$ and t_{gm} are both based on the assumption that the accretion disc structure is well-described by region (c). In our model, when $f_{\text{Edd},16} \leq \hat{f}_{\text{Edd},16}$, region (a) aligns with the BH and does not contribute to the torque. Additionally, the structure of region (b) closely resembles that of region (c) (see Figure 1), as the only difference between them is the dominant opacity source. Consequently, we adopt the same assumption in our calculation.

As discussed in Section 2, we assume that \mathbf{J}_{disc} is aligned with the outer section of the warped disc, as this region contains the majority of the disc angular momentum. Specifically, the outer section of the warped disc corresponds to $R_{\text{disc}} > R_{\text{warp}}$. This assumption holds as long as $R_{\text{disc}} \gg R_{\text{warp}}$. If this condition is not met, the angular momentum contribution from the inner section, which is aligned with the BH, would be comparable to that of the outer section. In

this case, \mathbf{J}_{disc} would not align with the outer section. Moreover, the condition $R_{\text{disc}} \gg R_{\text{warp}}$ is an implicit assumption in the derivation of Equation (36) (Martin et al. 2007). Even though the condition $R_{\text{disc}} \gg R_{\text{warp}}$ is always verified in the simulations conducted in this study (but may not hold for $M_{\text{BH}} \gtrsim 10^8 M_{\odot}$; see Figure 2), we modify the angular momentum model when $R_{\text{disc}} < R_{\text{warp}}$. In this regime, the strong Lense-Thirring torque significantly reduces the time-scale for (counter)-alignment between the disc and the BH. Following Dotti et al. (2013), Fiacconi et al. (2018), and C21, we assume that the disc and the BH instantaneously (counter)-align with each other. \mathbf{J}_{BH} aligns with the total angular momentum of the BH-disc system, defined as $\mathbf{J}_{\text{tot}} = \mathbf{J}_{\text{disc}} + \mathbf{J}_{\text{BH}}$, and \mathbf{J}_{disc} aligns with \mathbf{J}_{tot} if

$$\mathbf{j}_{\text{BH}} \cdot \mathbf{j}_{\text{disc}} \geq -\frac{J_{\text{disc}}}{2J_{\text{BH}}}. \quad (38)$$

Otherwise, \mathbf{J}_{disc} would end up counter-aligned with \mathbf{J}_{tot} (King et al. 2005).

2.4.4 Lense-Thirring effect for high mass accretion rates

In this section, we calculate the Lense-Thirring effect for $f_{\text{Edd},16} > \hat{f}_{\text{Edd},16}$. In this regime, the accretion disc remains misaligned with the BH, and the thick disc in the photon-trapping region, which lies in the wave-like regime, undergoes precession due to the Lense-Thirring effect. This scenario is analogous to the truncated disc model described in Koudmani et al. (2024).

Following Ingram & Motta (2019), the angular frequency of precession for the inner thick disc, ω_{prec} , is given by

$$\omega_{\text{prec}} = \frac{\int_{R_{\text{in}}}^{R_{\text{trap}}} \omega_{\text{LT}}(R) \Sigma(R) L(R) R dR}{\int_{R_{\text{in}}}^{R_{\text{trap}}} \Sigma(R) L(R) R dR}. \quad (39)$$

As noted by Ingram et al. (2009) and Koudmani et al. (2024), it is crucial to account for the bending wave radius R_{bw} , as the density decreases significantly for $R < R_{\text{bw}}$. Therefore, we define $R_{\text{in}} = \max(R_{\text{ISCO}}, R_{\text{bw}})$. In our calculations, we assume $H/R = 1$ when calculating R_{bw} (as shown in Kitaki et al. 2021). Assuming $\Sigma(R)L(R) \propto R^s$, we obtain:

$$\begin{aligned} \omega_{\text{prec}} &= 8ca_{\text{BH}} R_g^2 \frac{\int_{R_{\text{in}}}^{R_{\text{trap}}} R^{s+1-3} dR}{\int_{R_{\text{in}}}^{R_{\text{trap}}} R^{s+1} dR} \\ &= \frac{8ca_{\text{BH}}}{R_g} \frac{s+2}{s-1} \frac{(R_{\text{trap}}/R_g)^{s-1} - (R_{\text{in}}/R_g)^{s-1}}{(R_{\text{trap}}/R_g)^{s+2} - (R_{\text{in}}/R_g)^{s+2}}. \end{aligned} \quad (40)$$

Similarly to what done by Koudmani et al. (2024), the Lense-Thirring torque for a precessing disc is calculated as follows:

$$\mathbf{j}_{\text{BH,LT}} = -\mathbf{J}_{\text{BH}} \times \left\{ t_{\text{prec}}^{-1} \mathbf{j}_{\text{disc}} + t_{\text{align}}^{-1} (\mathbf{j}_{\text{BH}} \times \mathbf{j}_{\text{disc}}) \right\}, \quad (41)$$

where the first term describes the precession between the BH and the disc, which does not alter the magnitude of J_{disc} and J_{BH} , and the second term represents the additional alignment torque between the BH and the disc, as found in both simulations and analytic models (Volonteri et al. 2005; Liska et al. 2018). Here, t_{align} is the alignment time-scale, defined as

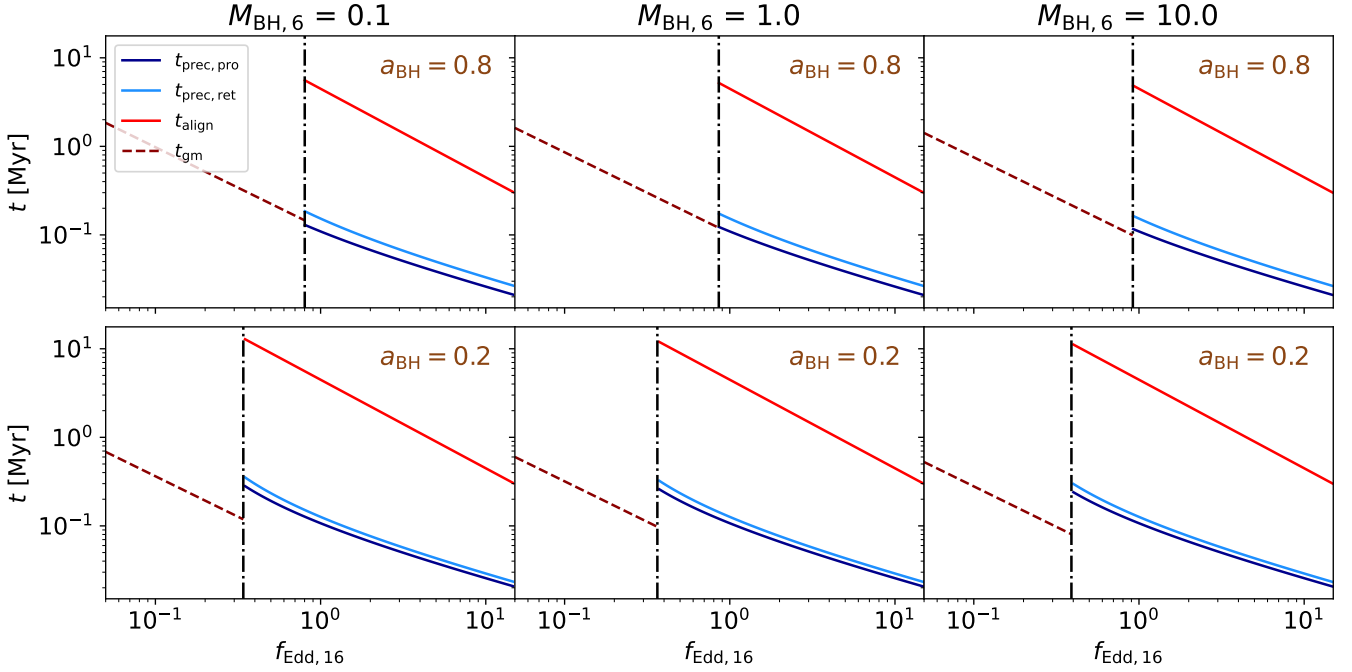


Figure 5. Time-scales t_{align} (red line), t_{gm} (dashed dark red line), and t_{prec} for prograde ($t_{\text{prec,pro}}$; dark blue line) and retrograde ($t_{\text{prec,ret}}$; light blue line) discs as a function of $f_{\text{Edd},16}$, displayed for $a_{\text{BH}} = 0.8$ (top row) and 0.2 (bottom row), and for $M_{\text{BH},6} = 0.1$ (left-hand column), 1 (central column), and 10 (right-hand column), with $\alpha_{0.1} = 1$ and $\xi = 0.7$. The vertical black dash-dotted line marks $\hat{f}_{\text{Edd},16}$. We find that $t_{\text{prec}} \sim t_{\text{gm}}$, whereas $t_{\text{align}} \gg t_{\text{gm}}$ at $f_{\text{Edd},16} = \hat{f}_{\text{Edd},16}$.

$$t_{\text{align}} = \frac{1}{2\pi} \frac{\dot{M}_{\text{BH}}}{\dot{M}_{\text{BH}}} = \frac{4.47}{f_{\text{Edd},16}} \text{ Myr}, \quad (42)$$

and t_{prec} is the precession time-scale for the BH:

$$t_{\text{prec}} = \frac{1}{\omega_{\text{prec}}} \frac{J_{\text{BH}}}{J_{\text{disc,trap}}}, \quad (43)$$

where $J_{\text{disc,trap}}$ is the angular momentum of the disc within the photon-trapping region.

Figure 5 presents t_{prec} , t_{acc} , and t_{gm} as functions of $f_{\text{Edd},16}$, for a few values of M_{BH} and a_{BH} . It is evident that these time-scales show minimal dependence on the BH mass, while their dependence on the BH spin is more pronounced. For the Lense-Thirring effect at low mass accretion rates (i.e. $f_{\text{Edd},16} < \hat{f}_{\text{Edd},16}$), both the alignment and precession time-scales are of the order of t_{gm} (Equation 36). However, for $f_{\text{Edd},16} > \hat{f}_{\text{Edd},16}$, the precession time-scale for both prograde and retrograde discs becomes much shorter than the alignment time-scale. It is also evident that t_{prec} is comparable to t_{gm} , while $t_{\text{align}} \gg t_{\text{gm}}$ at $f_{\text{Edd},16} = \hat{f}_{\text{Edd},16}$. This can be quantified by computing the ratio $t_{\text{gm}}/t_{\text{align}}$:

$$\frac{t_{\text{gm}}}{t_{\text{align}}} = 2.1 \times 10^{-2} \xi^{-5/7} \alpha_{0.1}^{58/35} M_{\text{BH},6}^{-2/35} a_{\text{BH}}^{5/7} \hat{f}_{\text{Edd},16}^{3/35}. \quad (44)$$

This result demonstrates that t_{align} is one to two orders of magnitude larger than t_{gm} , indicating that, at high mass ac-

cretion rates, the alignment process between the BH and the disc occurs much more slowly.¹¹

2.5 Self-gravitating mass

In this section, we discuss how we calculate R_{sg} and M_{sg} , as well as the motivation for imposing the constraint $R_{\text{disc}} < R_{\text{sg}}$.

In each region of the thin α -disc, we utilise the sound speed equation, derived from $c_s = \sqrt{P/\rho}$ in K08, to calculate R_{sg} . We define $R_{\text{sg},a}$, $R_{\text{sg},b}$, and $R_{\text{sg},c}$ as the self-gravitating radii for regions (a), (b), and (c), respectively, assuming that the entire disc is described by a single region:

$$\frac{R_{\text{sg},a}}{R_g} = 3.45 \times 10^3 \alpha_{0.1}^{2/9} M_{\text{BH},6}^{-2/9} f_{\text{Edd},16}^{4/9} Q_{\text{min}}^{2/9}, \quad (45)$$

$$\frac{R_{\text{sg},b}}{R_g} = 7.66 \times 10^4 \alpha_{0.1}^{14/27} M_{\text{BH},6}^{-26/27} f_{\text{Edd},16}^{-8/27} Q_{\text{min}}^{-20/27}, \quad (46)$$

$$\frac{R_{\text{sg},c}}{R_g} = 9.54 \times 10^4 \alpha_{0.1}^{28/45} M_{\text{BH},6}^{-52/45} f_{\text{Edd},16}^{-22/45} Q_{\text{min}}^{-8/9}. \quad (47)$$

We define the self-gravitating radius for our disc model as follows:

¹¹ If $\hat{f}_{\text{Edd},16} \gg 10^4$ or $M_{\text{BH},6} \ll 10^{-6}$, then t_{gm} would become comparable to t_{align} . However, this lies well outside the parameter space considered in this study.

$$R_{\text{sg}} = \begin{cases} R_{\text{sg},a} & \text{if } \max(R_{\text{ISCO}}, R_{\text{trap}}) \leq R_{\text{sg},a} < R_{\text{ab}} , \\ R_{\text{sg},b} & \text{if } R_{\text{ab}} \leq R_{\text{sg},b} < R_{\text{bc}} , \\ R_{\text{sg},c} & \text{if } R_{\text{bc}} \leq R_{\text{sg},c} . \end{cases} \quad (48)$$

Using R_{sg} , we compute M_{sg} by setting $R_{\text{disc}} = R_{\text{sg}}$ in the surface density integration from Equation (18).

If the accretion disc becomes self-gravitating (i.e. $M_{\text{disc}} > M_{\text{sg}}$), gravitational instabilities would develop in its outer regions. These instabilities could lead to disc fragmentation and potentially trigger star formation (Shlosman & Begelman 1987; Deng et al. 2017; Chen et al. 2023; Derdzinski & Mayer 2023) or generate non-axisymmetric structures such as spiral arms and clumps (Durisen et al. 2007). The exact details of these processes remain uncertain. However, gravitational instabilities would significantly alter the disc structure, as the transport of mass and angular momentum can no longer be adequately described by the thin α -disc model and may lead to disc truncation (Goodman 2003; Sirko & Goodman 2003; Thompson et al. 2005; Rafikov 2015).

Following Perego et al. (2009), Dubois et al. (2014), Fiacconi et al. (2018), and C21, we avoid these complexities by assuming that the disc truncates at $R_{\text{disc}} = R_{\text{sg}}$, ensuring that the disc does not enter a self-gravitating state. This imposes a constraint on \dot{M}_{in} such that $M_{\text{disc}} \leq M_{\text{sg}}$ (in the case that M_{disc} is initially larger than M_{sg} , then \dot{M}_{in} is set to zero until M_{disc} decreases, due to accretion onto the BH, down to the value of M_{sg}). By preventing gravitational instabilities from developing in the outer disc regions, this approach maintains the validity of the thin α -disc framework. The limitations of this assumption are discussed in Section 5.2.1.

2.6 Radiative efficiency

Due to the strong photon-trapping effect in super-Eddington flows, photons cannot freely escape the accretion disc in the innermost region. Consequently, the radiative efficiency is reduced compared to the efficiency determined solely using the Kerr metric as in Bardeen et al. (1972). To smoothly transition between the sub-Eddington and super-Eddington regimes, we adopt the results from Madau et al. (2014), which are derived from fitting numerical solutions of the relativistic slim accretion disc equations presented in Sądowski (2009):

$$\frac{\eta}{1/16} = A(a_{\text{BH}}) \left[\frac{0.985}{1 + B(a_{\text{BH}})f_{\text{Edd},16}} + \frac{0.015}{1 + C(a_{\text{BH}})f_{\text{Edd},16}} \right], \quad (49)$$

where the coefficients A , B , and C are given by, respectively,

$$A(a_{\text{BH}}) = (0.9663 \mp 0.9292 a_{\text{BH}})^{-0.5639}, \quad (50)$$

$$B(a_{\text{BH}}) = (4.627 \mp 4.445 a_{\text{BH}})^{-0.5524}, \quad (51)$$

$$C(a_{\text{BH}}) = (827.3 \mp 718.1 a_{\text{BH}})^{-0.7060}, \quad (52)$$

where the minus and plus signs correspond to a prograde and retrograde disc, respectively.

We note that Madau et al. (2014) originally calibrated this fitting function for prograde-only accretion flows (i.e. Equations 50–52 only had the minus sign), as the results from Sądowski (2009) were specified only for those cases. We extended the fitting function to cover also retrograde accretion

flows and verified that this extension provides reasonable results: Figure D1 illustrates the value of η as a function of a_{BH} for different values of $f_{\text{Edd},16}$.

We note with caution that the results of Madau et al. (2014) are derived from numerical solutions of the relativistic slim accretion disc in Sądowski (2009), which exhibit a different disc structure compared to K18. It is not straightforward to properly compare the two models. However, we can partially validate Equations (49)–(52) using simulation results from Kitaki et al. (2021), which are in close agreement with those of K18. Their simulations model a non-spinning BH accreting at a rate of $\dot{M}_{\text{BH,accr}} \sim 180 L_{\text{Edd}}/c^2$ (i.e. $f_{\text{Edd},16} \sim 11.25$). The (bolometric) luminosity observed by a distant observer is $L \sim 2.5 L_{\text{Edd}}$, implying a radiative efficiency $\eta = L/(\dot{M}_{\text{BH,accr}} c^2) \sim 0.0139$, which is consistent with $\eta \sim 0.012$ predicted by Equations (49)–(52) when using $a_{\text{BH}} = 0$ and $f_{\text{Edd},16} = 11.25$. These findings suggest that the radiative efficiency adopted in our model remains in reasonable agreement with this expression, even if the underlying disc structure differs.¹²

3 NUMERICAL SETUP

This sub-grid model, as detailed in Section 2, is built upon the model and code in C21 and has been integrated into the publicly available N -body, mesh-less hydrodynamics code GIZMO¹³ (Hopkins 2015). The numerical setup follows the methodology outlined in C21. We provide here a brief summary for completeness.

The initial conditions consist of a single BH particle, which represents a sub-resolution “BH+accretion disc” system, embedded within a spherically distributed stellar structure and surrounded by a gaseous circumnuclear disc (CND).

The spherical stellar component is modelled using the Hernquist (1990) profile as a function of (spherical) radius r :

$$\rho_b(r) = \frac{M_b}{2\pi} \frac{r_b}{r(r+r_b)^3}, \quad (53)$$

where the total mass of the bulge is $M_b = 5 \times 10^8 M_{\odot}$ and its scale radius is $r_b = 100$ pc.

The CND is a rotationally supported disc in vertical hydrostatic equilibrium. Its surface density profile is given by the exponential disc as follows:

$$\Sigma_{\text{CND}}(R) = \frac{M_{\text{CND}}}{2\pi R_{\text{CND}}^2} \exp\left(-\frac{R}{R_{\text{CND}}}\right), \quad (54)$$

where the total mass of the disc is $M_{\text{CND}} = 10^8 M_{\odot}$ and its scale radius is $R_{\text{CND}} = 50$ pc.

The vertical density profile and velocity field are computed using the publicly available code GD_BASIC¹⁴ to ensure vertical hydrostatic equilibrium under the combined potential

¹² We note that Sądowski (2011) quotes a slightly higher value for the radiative efficiency, of the order of 0.025 (see also Watarai et al. 2000; Kubota & Done 2019). However, the proper comparison here is with the results of Sądowski (2009), since those were used for the improved fitting functions by Madau et al. (2014).

¹³ <http://www.tapir.caltech.edu/~phopkins/Site/GIZMO.html>

¹⁴ <https://alessandrolupiastro.wordpress.com/software/>

Table 2. Summary of simulations with different parameters. From left to right, we list the name of each simulation, the initial BH mass, $M_{\text{BH},0}$, the initial Eddington ratio, $f_{\text{Edd},16,0}$, the circularisation radius ratio of the inflow gas, W_{circ} , the initial BH spin magnitude, $a_{\text{BH},0}$, the initial angle between the angular momentum of the BH and that of the disc, $\theta_{\text{BH-disc},0}$, the minimum Toomre parameter, Q_{min} , and the initial angle between the angular momentum of the gas and that of the disc, $\theta_{\text{BH-gas},0}$. The suffixes VL, L, H, and VH denote runs wherein a specific parameter is set to very-low, low, high, and very-high values, respectively. The top 18 rows show the runs with initial gas-disc alignment (illustrated by the top diagram), whereas the bottom three rows show the runs with initial BH-disc alignment (bottom diagram).

Simulation name	$M_{\text{BH},0}/M_{\odot}$	$f_{\text{Edd},16,0}$	W_{circ}	$a_{\text{BH},0}$	$\theta_{\text{BH-disc},0}$	Q_{min}	$\theta_{\text{gas-disc},0}$
Fiducial	10^6	1	0.1	0.8	$5\pi/6$	1	0
Edd-H	10^6	5	0.1	0.8	$5\pi/6$	1	0
Edd-L	10^6	0.6	0.1	0.8	$5\pi/6$	1	0
Edd-VL	10^6	0.1	0.1	0.8	$5\pi/6$	1	0
Wcirc-VH	10^6	1	0.9	0.8	$5\pi/6$	1	0
Wcirc-H	10^6	1	0.5	0.8	$5\pi/6$	1	0
Wcirc-L	10^6	1	0.05	0.8	$5\pi/6$	1	0
Wcirc-VL	10^6	1	0.01	0.8	$5\pi/6$	1	0
aBH-H	10^6	1	0.1	0.99	$5\pi/6$	1	0
aBH-L	10^6	1	0.1	0.5	$5\pi/6$	1	0
aBH-VL	10^6	1	0.1	0.2	$5\pi/6$	1	0
theta-L	10^6	1	0.1	0.8	$2\pi/3$	1	0
theta-VL	10^6	1	0.1	0.8	$\pi/2$	1	0
Q-VH	10^6	1	0.1	0.8	$5\pi/6$	4	0
Q-H	10^6	1	0.1	0.8	$5\pi/6$	2	0
Q-L	10^6	1	0.1	0.8	$5\pi/6$	0.5	0
MBH-H	10^7	1	0.1	0.8	$5\pi/6$	1	0
MBH-L	10^5	1	0.1	0.8	$5\pi/6$	1	0
GD-Misalign-VH	10^6	1	0.1	0.8	0	1	$5\pi/6$
GD-Misalign-H	10^6	1	0.1	0.8	0	1	$3\pi/4$
GD-Misalign-L	10^6	1	0.1	0.8	0	1	$2\pi/3$

of the bulge, CND, and BH (Lupi et al. 2015). The gas is initially set up assuming an ideal-gas equation of state with a uniform temperature of $T_0 = 2 \times 10^4$ K and a polytropic index of $\gamma = 5/3$. The system is first evolved in isolation for 20 Myr, with only gravity and hydrodynamics active, to allow for relaxation. Subsequently, during the simulations, a lower polytropic index of $\gamma = 7/5$ is adopted to mimic mild cooling and drive gas accretion onto BH without using a dedicated cooling model (Dotti et al. 2009; C21; Sala et al. 2021).

Both the number of stellar particles, N_{stars} , and the number of gas particles, N_{gas} , are set to 10^5 ($N_{\text{stars}} = N_{\text{gas}} = 10^5$). For the stellar particles, the Plummer-equivalent gravitational softening length is set to $\epsilon_{\text{stars}} = 0.16$ pc, whereas for the BH particle, it is $\epsilon_{\text{BH}} = 1$ pc. For the gas particles, a fully adaptive softening scheme is employed. Their resolution is defined by the size of the smoothing kernel, which is chosen to include an effective number of neighbours, $N_{\text{ngb}} = 32$. The minimum gravitational softening length for the gas, which sets the maximum spatial resolution, is set to $\epsilon_{\text{gas}} = 0.16$ pc.

The mass transfer rate from resolved scales onto the accretion disc of the BH particle, \dot{M}_{in} , can be determined using different prescriptions. In this work, we use the BHL formula:

$$\dot{M}_{\text{in}} = \frac{4\pi\alpha_{\text{acc}}G^2M_{\text{BH}}^2\rho_{\text{gas}}}{(c_{\text{s,gas}}^2 + v^2)^{3/2}}, \quad (55)$$

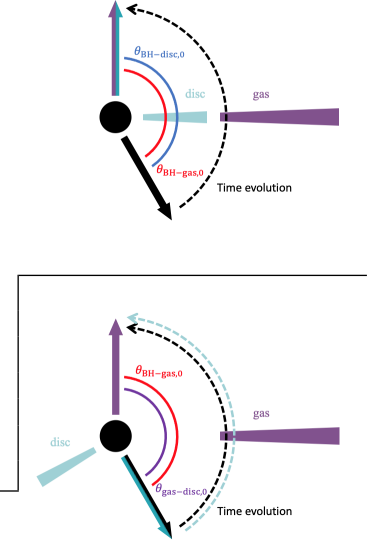
where ρ_{gas} is the density of the surrounding gas, v represents the relative velocity between the gas and the BH, $c_{\text{s,gas}}$ is the sound speed of the surrounding gas, and α_{acc} is a dimensionless parameter to boost the mass accretion rate for

unresolved dense gas in kpc-scale simulations (e.g. Springel et al. 2005; Booth & Schaye 2009). At high-enough resolution, as in isolated simulations of galaxies (e.g. Tamburello et al. 2017) and their central regions (e.g. CNDs; Souza Lima et al. 2017, 2020), this boost parameter is not needed (but see Negri & Volonteri 2017 for a discussion): therefore, we set $\alpha_{\text{acc}} = 1$.

When computing \dot{M}_{in} , the gas properties are determined using a mass-weighted average over the nearest $N_{\text{ngb,BH}}$ neighbour gas particles around the BH. To ensure a sufficiently large sampling of the gas properties surrounding the BH, we set $N_{\text{ngb,BH}} = 3N_{\text{ngb}}$. The BH particle kernel is defined as the region encompassing $N_{\text{ngb,BH}}$ neighbours, up to a maximum accretion radius, $r_{\text{max,acc}} = 10$ pc.

There are also many different prescriptions to determine \dot{J}_{in} . In this paper, we consider coherent accretion, in which the angular momentum of the inflow is aligned to that of the surrounding gas (Volonteri et al. 2007). Consequently, we use the relation $\dot{J}_{\text{in}} = \Lambda_{\text{in}}\dot{M}_{\text{in}}\mathbf{j}_{\text{gas}}$, where Λ_{in} is the specific angular momentum of the inflowing material (as in C21), and \mathbf{j}_{gas} is the unit vector of the total angular momentum of the gas in the BH kernel, \mathbf{J}_{gas} (of magnitude J_{gas}). In the simulation, we define the z -axis as the direction of the initial \mathbf{j}_{gas} (i.e. the initial CND lies in the x - y plane before relaxation).

Since angular momentum transport is not fully resolved for the inflowing gas, we assume that it circularises at the circularisation radius, R_{circ} , which reduces the angular momentum influx and prevents the formation of a self-gravitating disc with excessive angular momentum. We further define the ra-



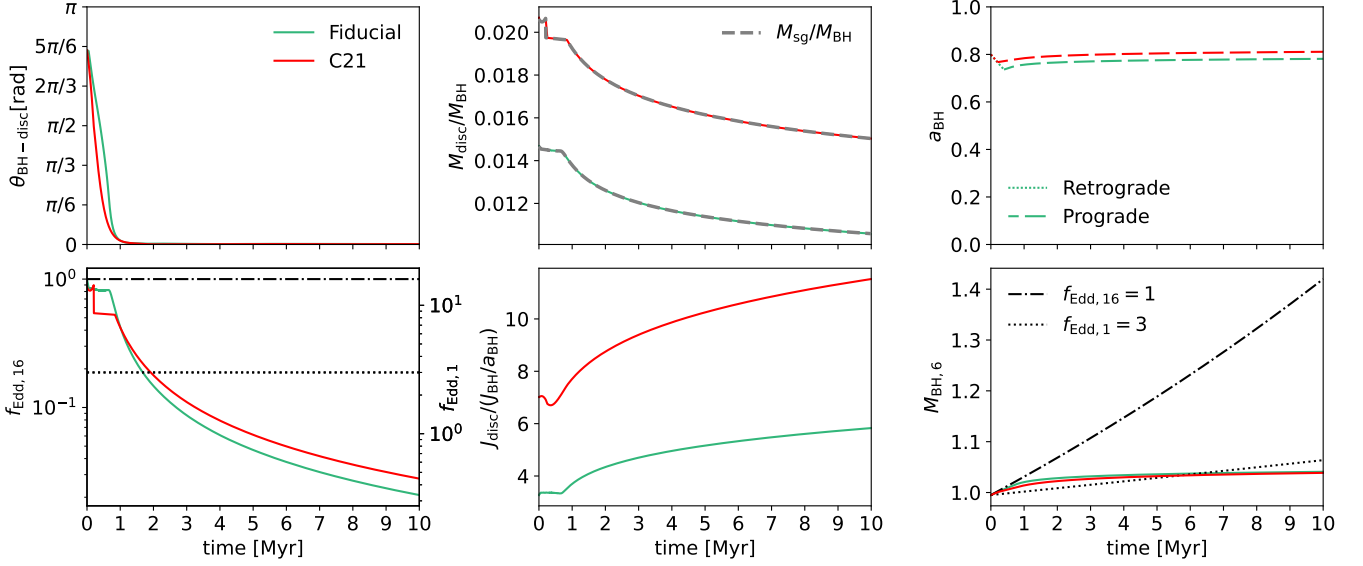


Figure 6. Comparison between the Fiducial run using our model (green) and the model by C21 (red). Each panel shows the time evolution of key quantities. *Top left panel:* misalignment angle between the BH and the disc, $\theta_{\text{BH-disc}}$. *Top central panel:* disc mass, M_{disc} , in units of M_{BH} . The self-gravitating mass, M_{sg} , is also shown as a grey dashed line for comparison. *Top right panel:* BH spin parameter, a_{BH} . Dotted and dashed lines correspond to a retrograde and prograde disc, respectively. *Bottom left panel:* Eddington ratio, $f_{\text{Edd},16}$, with $f_{\text{Edd},1}$ shown on the right axis for comparison. For reference, the black dash-dotted line marks $f_{\text{Edd},16} = 1$ and the dotted line indicates $f_{\text{Edd},1} = 3$. *Bottom central panel:* disc angular momentum, J_{disc} , in units of $J_{\text{BH}}/a_{\text{BH}} = GM_{\text{BH}}^2/c$ (i.e. the maximum angular momentum of a BH). *Bottom right panel:* BH mass in units of $10^6 M_{\odot}$, $M_{\text{BH},6}$. The black dash-dotted and dotted lines represent reference tracks for constant specific accretion rates of $f_{\text{Edd},16} = 1$ and $f_{\text{Edd},1} = 3$, respectively. Owing to the shorter (longer) alignment time-scale of the Lense-Thirring torque model at low (high) mass accretion rates, our model remains at $f_{\text{Edd},16} \sim \hat{f}_{\text{Edd},16} \sim 0.9$ for the first 1 Myr in this run. After the BH aligns with the disc, $f_{\text{Edd},16}$ continues to decrease, as the inflow onto the disc gradually increases J_{disc} .

tio of the circularisation radius to the self-gravitating radius as $W_{\text{circ}} = R_{\text{circ}}/R_{\text{sg}}$. The value of W_{circ} can be specified in the code. We impose an upper limit on Λ_{in} by comparing two possible values:

$$\Lambda_{\text{in}} = \min \left(\frac{J_{\text{disc}}(R_{\text{circ}})}{M_{\text{disc}}(R_{\text{circ}})}, \frac{J_{\text{gas}}}{M_{\text{gas}}} \right), \quad (56)$$

where M_{gas} is the total mass of the gas particles in the BH particle kernel.

For the properties of the BH and disc, we perform simulations by initialising the BH mass, spin, and Eddington ratio as follows: $M_{\text{BH}} = M_{\text{BH},0}$, $a_{\text{BH}} = a_{\text{BH},0}$, and $f_{\text{Edd},16} = f_{\text{Edd},16,0}$. To prevent an initial rapid increase in M_{disc} due to a large inflow onto the accretion disc (as was the case in C21, wherein the disc was initially less massive than its own self-gravitating mass), we set the initial disc mass to $M_{\text{disc},0} = M_{\text{sg}}$. The initial disc angular momentum, $J_{\text{disc},0}$, is determined based on other initial given values.

To describe the initial angle between the BH, disc, and surrounding gas, we introduce the following angles: $\theta_{\text{BH-disc}} \equiv \arccos(\mathbf{j}_{\text{BH}} \cdot \mathbf{j}_{\text{disc}})$, $\theta_{\text{gas-disc}} \equiv \arccos(\mathbf{j}_{\text{gas}} \cdot \mathbf{j}_{\text{disc}})$, and $\theta_{\text{BH-gas}} \equiv \arccos(\mathbf{j}_{\text{BH}} \cdot \mathbf{j}_{\text{gas}})$. We remind the reader that \mathbf{j}_{disc} refers to the outer part of the accretion disc. We initialise $\theta_{\text{BH-disc}} = \theta_{\text{BH-disc},0}$ and $\theta_{\text{gas-disc}} = \theta_{\text{gas-disc},0}$. Two types of initial misalignment configurations are considered to explore different scenarios of BH-disc-gas alignment:

- (i) BH-disc alignment: we set $\theta_{\text{BH-disc},0} = 0$, meaning that

\mathbf{J}_{BH} is parallel to \mathbf{J}_{disc} , while both are misaligned with the angular momentum of the surrounding gas ($\theta_{\text{gas-disc},0} \neq 0$). In this case, $\theta_{\text{BH-gas},0} = \theta_{\text{gas-disc},0}$.

- (ii) Gas-disc alignment: we set $\theta_{\text{gas-disc},0} = 0$, meaning that \mathbf{J}_{gas} is parallel to \mathbf{J}_{disc} , while the BH is misaligned with the disc ($\theta_{\text{BH-disc},0} \neq 0$). In this case, $\theta_{\text{BH-gas},0} = \theta_{\text{BH-disc},0}$.

These two types of initial conditions represent two different scenarios wherein a new stream of gas with a different angular momentum direction flows into the centre of the galaxy. If the BH initially lacks a disc or hosts only a small accretion disc with negligible mass and angular momentum, the incoming gas stream is expected to establish a configuration similar to the gas-disc alignment case. Conversely, if the BH already possesses a large accretion disc aligned with its own spin, the initial condition would resemble the BH-disc alignment scenario.

Q_{min} and W_{circ} are constants that can be set in the code. The choices of parameters for the simulation runs are summarised in Table 2. The fixed parameters used in all simulations are $\alpha_{0,1} = 1$, $\xi = 0.7$, and $\dot{M}_{\text{out}} = 0$.

4 RESULTS

In this section, we analyse our simulation results using the new sub-grid model presented in this paper. For both the Fiducial run and the GD-Misalign-VH run, we also apply the model from C21, using identical initial conditions. In both

models, we set $M_{\text{disc},0} = M_{\text{sg}}$ and compute $J_{\text{disc},0}$ accordingly. However, since M_{sg} differs between the two models, the resulting $J_{\text{disc},0}$ varies. This discrepancy arises because our model adopts the thin α -disc structure from K08, whereas C21 refer to Frank et al. (2002). Due to the lower surface density in Frank et al. (2002; see Figure 1 and Appendix B), the results of C21 yield a larger R_{sg} . As a result of the combined effects of lower surface density and larger R_{sg} , the values of M_{disc} and corresponding J_{disc} in C21 are typically 1.5–2 times larger than those obtained with our model for the same initial $f_{\text{Edd},16}$ and M_{BH} .

We first discuss the results of the Fiducial run in Section 4.1. In Section 4.2, we explore variations in model parameters for the initial gas-disc alignment configuration. Section 4.3 presents the GD-Misalign-L, GD-Misalign-H, and GD-Misalign-VH runs, which assume initial BH-disc alignment and can lead to higher mass accretion rates.

4.1 The Fiducial run

Figure 6 shows the evolution of $\theta_{\text{BH-disc}}$, $f_{\text{Edd},16}$, M_{disc} , J_{disc} , a_{BH} , and M_{BH} in the Fiducial run. Results from both our model and the model by C21 are presented for comparison. In both models, $\theta_{\text{BH-disc}}$ rapidly decreases from its initial value of $5\pi/6$ to 0 within the first 1 Myr, indicating that the BH and the accretion disc quickly align with each other due to the Lense-Thirring torque.

In our model, $f_{\text{Edd},16}$ rapidly decreases to $f_{\text{Edd},16} \sim \hat{f}_{\text{Edd},16} \sim 0.9$ and remains at this value for approximately 1 Myr while the BH is aligning with the disc. This behaviour arises from the application of two torque models, depending on whether the Eddington ratio is above or below $\hat{f}_{\text{Edd},16}$ (Section 2.4). The high mass accretion rate torque model, based on thick disc precession, shows a significantly slower alignment process between the BH and the disc compared to the low mass accretion model, which is based on the Bardeen-Peterson configuration (Equation 44).

Consequently, when $f_{\text{Edd},16} < \hat{f}_{\text{Edd},16}$, the strong alignment torque efficiently reduces J_{disc} , resulting in a more compact disc, leading to an increase in $f_{\text{Edd},16}$. Conversely, when $f_{\text{Edd},16} > \hat{f}_{\text{Edd},16}$, the alignment torque becomes much weaker. In this run, we consider an initial condition in which the disc is aligned with the surrounding gas, so the inflow of angular momentum from the gas is parallel to \mathbf{J}_{disc} . As a result, the angular momentum gained from the gas inflow exceeds the reduction caused by the Lense-Thirring torque. This increases J_{disc} , preventing the system from sustaining $f_{\text{Edd},16} > \hat{f}_{\text{Edd},16}$.

Conversely, once the BH and the disc become nearly aligned, $f_{\text{Edd},16}$ departs from this “equilibrium state” and begins to decline, as the Lense-Thirring torque becomes significantly weaker when the misalignment angle between the BH and the disc is small. In this regime, the inflow of angular momentum from the surrounding gas increases the disc angular momentum. As a result, J_{disc} continues to increase after $t \sim 1$ Myr, once the BH has aligned with the disc, thereby reducing $f_{\text{Edd},16}$.

The results from the model by C21 exhibit a different trend in the evolution of $f_{\text{Edd},16}$ during the first 1 Myr, when the BH is misaligned with the disc. Initially, $f_{\text{Edd},16}$ increases slightly, as the strong Lense-Thirring torque efficiently removes angular momentum from the disc. Then, as the BH

and the disc transition from retrograde to prograde (i.e. when $\theta_{\text{BH-disc}} = \pi/2$), $f_{\text{Edd},16}$ drops to $f_{\text{Edd},16} \sim 0.5$. This occurs because their model imposes an upper limit of $f_{\text{Edd},\eta} \leq 1$. For a prograde accretion disc with $a_{\text{BH}} \sim 0.8$, the radiative efficiency is approximately 0.12 in their model, calculated from the Kerr metric following Bardeen et al. (1972). As a result, $f_{\text{Edd},16} \sim 0.5$ corresponds to $f_{\text{Edd},\eta} \sim 1$, which enforces the cap on $f_{\text{Edd},16}$. After $t > 1$ Myr, this model also shows a gradual decline in $f_{\text{Edd},16}$ due to the increase in J_{disc} from the gas inflow.

Interestingly, despite being based on different physical arguments, both models exhibit a qualitatively similar Eddington cap behaviour around $f_{\text{Edd},16} \sim \mathcal{O}(1)$ in this run. In the model from C21, the cap arises from the imposed limit $f_{\text{Edd},\eta} \leq 1$. In contrast, in our model, it emerges due to the torque prescription changing from the Bardeen-Peterson configuration to the thick disc precession model when $f_{\text{Edd},16} > \hat{f}_{\text{Edd},16}$.

For an easier comparison with alternative definitions of Eddington ratio, we also show the values of $f_{\text{Edd},1}$ in the panel. It is important to note that the definition of super-Eddington accretion varies across the literature. Above $L_{\text{BH}}/L_{\text{Edd}} = 0.3$, the thin α -disc model ceases to properly describe the inner region of the accretion disc (Koratkar & Blaes 1999); hence, some studies classified observed sources as super-Eddington for $f_{\text{Edd},1} > 3$ (assuming a typical value of $\eta = 0.1$; e.g. Du et al. 2018; Liu et al. 2021), while it is common in theoretical studies to adopt $f_{\text{Edd},16} = 1$ as the super-Eddington threshold for simplicity (e.g. Madau et al. 2014). Following these definitions, we include horizontal lines for $f_{\text{Edd},16} = 1$ (the threshold adopted in, e.g. Sassano et al. 2023; Lupi et al. 2024a) and $f_{\text{Edd},1} = 3$ (as done in, e.g. Capelo et al. 2015, 2017) in the panel.

It is important to stress that, in both runs, the BHL accretion rate always exceeds the BH mass accretion rate by at least one order of magnitude. The lower BH accretion rate arises because the angular momentum of the disc, which is crucial in determining $f_{\text{Edd},16}$, cannot be instantaneously removed. Additionally, the mass inflow rate onto the accretion disc is constrained by the condition $M_{\text{disc}} \leq M_{\text{sg}}$ (see Section 2.5). As a result, in both cases, $M_{\text{disc}} = M_{\text{sg}}$ due to sufficient inflow from the surrounding gas. This highlights the critical role of angular momentum inflow in regulating BH growth. If it cannot be reduced effectively, a high BH mass accretion rate cannot be sustained.

The values of M_{disc} and J_{disc} are higher in the model from C21 compared to our model, due to the use of different reference structures for the thin α -disc. However, this has a minor effect on the evolution of the BH properties.

In Figure 6 (bottom-right panel), we also show the evolution of the BH mass for a BH accreting at constant (specific) rates of $f_{\text{Edd},16} = 1$ and $f_{\text{Edd},1} = 3$. In both runs, the BH mass increases by only a few per cent over 10 Myr, comparable to the growth expected if the BH accreted steadily at $f_{\text{Edd},1} = 3$. In contrast, if the BH had consistently accreted at $f_{\text{Edd},16} = 1$ throughout the same period, its mass would have increased by approximately 40 per cent.

The spin parameter, a_{BH} , exhibits a small change in both runs. Since the Lense-Thirring torque does not affect the magnitude of a_{BH} , the spin evolution is governed by accretion onto the BH. Initially, the disc is retrograde, leading to a decrease in a_{BH} . Once the BH aligns with the disc, a_{BH}

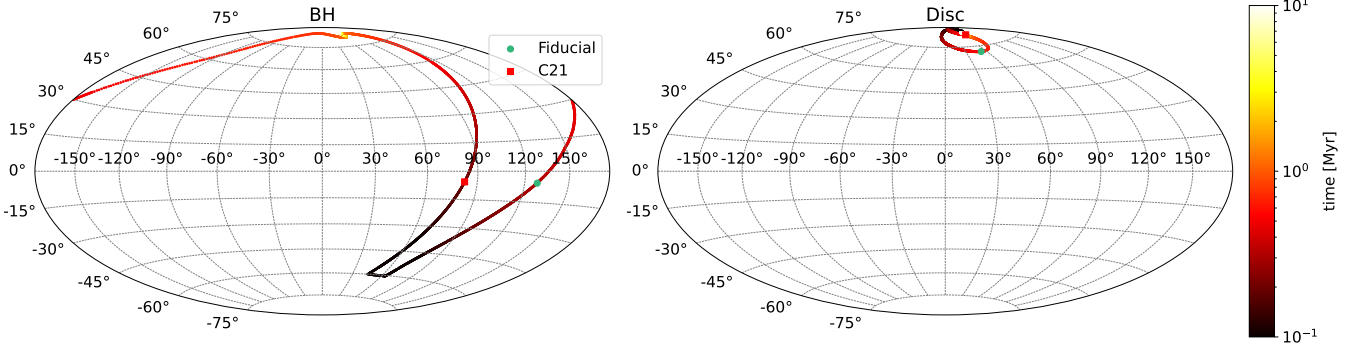


Figure 7. Evolution of the BH (left-hand panel) and disc (right-hand panel) angular momenta for the Fiducial run using our model (green circles) and the model by C21 (red squares), shown via Hammer projections wherein the equatorial plane is defined by the angular momentum of the gas within the BH kernel of the initial conditions (before relaxation). The colour coding indicates time evolution from 0.1 to 10 Myr. In both cases, the direction of \mathbf{j}_{gas} is nearly aligned with the z -axis and thus not shown. Our model exhibits stronger precession in the BH evolution compared to C21, as the Lense-Thirring torque at higher mass accretion rates produces a stronger precession torque. At the beginning of the simulation, \mathbf{j}_{BH} undergoes pronounced precession in our model, as $f_{\text{Edd},16,0} > \hat{f}_{\text{Edd},16}$, resulting in a change in longitude while the latitude remains nearly constant for a brief period.

gradually increases due to prograde accretion. However, this growth slows down as $f_{\text{Edd},16}$ declines. Overall, the net change in a_{BH} is minimal, as the effects of retrograde and prograde accretion largely cancel out.

Figure 7 shows the evolution of the directions of the disc and BH angular momentum vectors for both models, projected onto the full-sky sphere using Hammer projections. Initially, the directions of both \mathbf{j}_{disc} and \mathbf{j}_{gas} are approximately aligned with the z -axis [i.e. the longitude and latitude are around $(0^\circ, 90^\circ)$], although not perfectly, due to relaxation effects. The initial longitude and latitude of \mathbf{j}_{BH} are approximately $(45^\circ, -60^\circ)$. We fix the initial longitude to 45° for all runs in this work, noting that this value does not affect the results due to symmetry. The initial latitude is set by $\theta_{\text{BH-disc},0}$. Because \mathbf{j}_{gas} is roughly aligned with the z -axis, the initial latitude is therefore around -60° .

For both models, during the first 1 Myr, the BH spin undergoes a combination of precession and alignment towards the disc due to the Lense-Thirring torque. In our model, the precession motion is more pronounced due to the use of the inner precessing thick disc torque model at high accretion rates. During this period, \mathbf{j}_{disc} shows a slight precession from its initial direction due to the Lense-Thirring torque. Since J_{disc} is several times larger than J_{BH} , its direction evolves more slowly. Our model exhibits a more significant evolution of \mathbf{j}_{disc} compared to that of C21, as it incorporates the torque model with stronger precession and the magnitude of \mathbf{J}_{disc} is smaller.

After $t \gtrsim 1$ Myr, both models reach a configuration where $\mathbf{j}_{\text{disc}} \sim \mathbf{j}_{\text{BH}} \sim \mathbf{j}_{\text{gas}}$, indicating that the BH has aligned with both the disc and the surrounding gas. Subsequently, the directions of the disc and the BH remain stable. This configuration would only change if the direction of the gas were to vary significantly, which is not observed in this system owing to the simple setup of the CND and stellar components.

4.2 Initial gas-disc alignment

In this section, we consider the gas-disc alignment initial condition, when the gas surrounding the BH is aligned with the accretion disc, and the BH is misaligned with the disc, i.e. $\theta_{\text{BH-disc},0} \neq 0$ and $\theta_{\text{gas-disc},0} = 0$.

In the first column of Figure 8, we present the evolution of $f_{\text{Edd},16}$ and $\theta_{\text{BH-disc}}$ for simulations with different initial Eddington ratios. We compare the runs Edd-VL, Edd-L, Fiducial, and Edd-H, corresponding to $f_{\text{Edd},16,0} = 0.1, 0.6, 1$, and 5, respectively.

For the Edd-VL run, $f_{\text{Edd},16}$ initially increases from 0.1 to 0.2 before gradually decreasing. This trend is qualitatively consistent with the findings of C21. This aligns with our expectation, as our model should reproduce similar results to those of C21 if $f_{\text{Edd},16} \ll 1$. For $t \lesssim 2$ Myr, the accretion disc remains significantly misaligned with the BH, i.e. $\theta_{\text{BH-disc}} \gtrsim \pi/6$. In this regime, the strong Lense-Thirring torque acts to reduce both $\theta_{\text{BH-disc}}$ and J_{disc} , thereby enhancing the BH mass accretion rate. However, once $\theta_{\text{BH-disc}}$ decreases further and the disc is nearly aligned with the BH, the Lense-Thirring torque can no longer efficiently counterbalance the angular momentum supplied by the inflowing gas. Consequently, J_{disc} increases, leading to a decline in $f_{\text{Edd},16}$. The alignment process between the BH and the disc also slows down as the Lense-Thirring torque weakens.

For the Edd-L, Fiducial, and Edd-H runs, $f_{\text{Edd},16}$ rapidly reaches $f_{\text{Edd},16} \sim \hat{f}_{\text{Edd},16}$ and remains at this value for approximately 1 Myr. Regardless of whether the initial condition is $f_{\text{Edd},16,0} = 0.6$ or $f_{\text{Edd},16,0} = 5$, $f_{\text{Edd},16}$ settles into a stable state around $\hat{f}_{\text{Edd},16}$ due to the strong (weak) torque in the low (high) mass accretion rate regime. However, the Edd-L run maintains this state for a slightly shorter duration, as $\theta_{\text{BH-disc}}$ is already smaller than $5\pi/6$ when the system enters this state. This is due to the shorter alignment timescale in the low accretion regime. After leaving this state, all three runs exhibit a similar decline in $f_{\text{Edd},16}$, as a result of increasing disc angular momentum from the inflow. The alignment between the BH and the disc also proceeds more

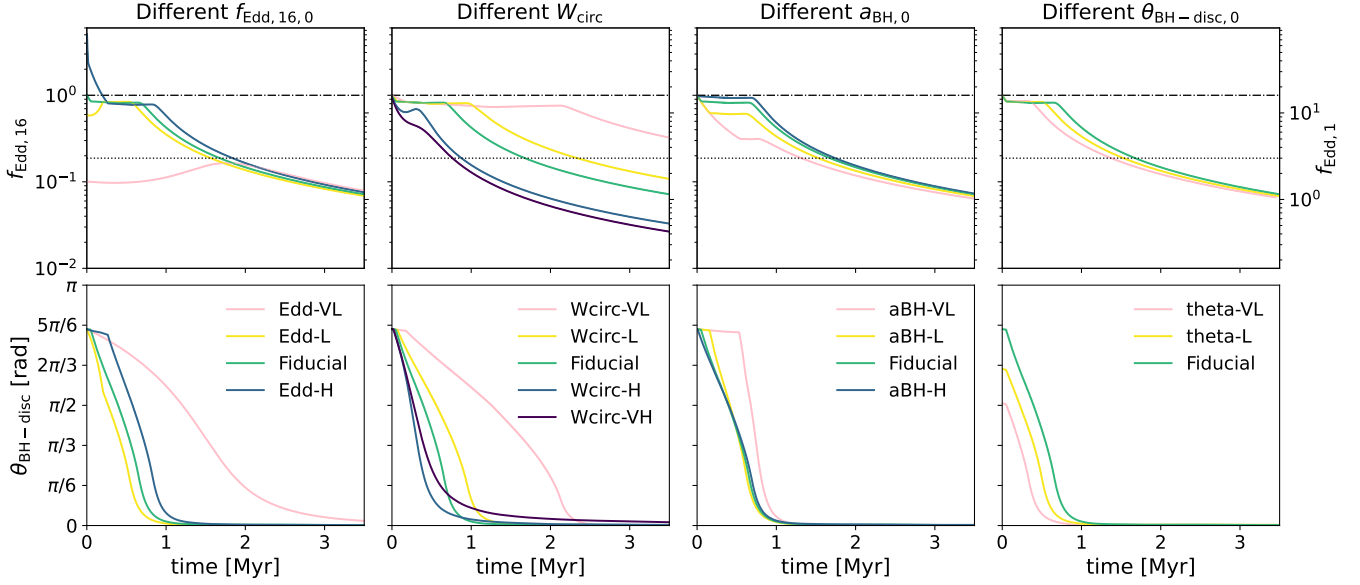


Figure 8. Time evolution of $f_{\text{Edd},16}$ (top row; the values of $f_{\text{Edd},1}$ are also shown for comparison) and $\theta_{\text{BH-disc}}$ (bottom row) for a series of runs in which we vary one parameter at a time of the Fiducial run. In the top row, the black dash-dotted line marks $f_{\text{Edd},16} = 1$, whereas the dotted line indicates $f_{\text{Edd},1} = 3$. In all shown runs, $M_{\text{BH},0} = 10^6 M_{\odot}$, $Q_{\text{min}} = 1$, and $\theta_{\text{gas-disc},0} = 0$. Left to right panels: effects of varying the initial Eddington ratio $f_{\text{Edd},16,0}$, the ratio of the circularisation radius to the self-gravitating radius W_{circ} , the initial BH spin $a_{\text{BH},0}$, and the initial misalignment angle between the BH and the disc $\theta_{\text{BH-disc},0}$ (see the different values of these parameters in Table 2). The Fiducial run is shown in green for reference. Most initial conditions exhibit a similar stabilisation at $f_{\text{Edd},16} \sim \hat{f}_{\text{Edd},16}$, consistent with the behaviour of the Fiducial run. Exceptions are the Edd-VL, Wcirc-H, and Wcirc-VH runs, wherein this stabilisation is not reached due to inefficient removal of disc angular momentum.

quickly in these runs than in the Edd-VL case, due to the stronger Lense-Thirring torque.

In the second column of Figure 8, we illustrate the impact of different values of W_{circ} on the evolution of $f_{\text{Edd},16}$ and $\theta_{\text{BH-disc}}$ by comparing the runs Wcirc-VH, Wcirc-H, Fiducial, Wcirc-L, and Wcirc-VL, with $W_{\text{circ}} = 0.9, 0.5, 0.1, 0.05$, and 0.01 , respectively. A smaller value of W_{circ} corresponds to a lower upper limit for the specific angular momentum of the inflowing gas onto the disc, Λ_{in} . For runs with $W_{\text{circ}} \leq 0.1$, the Eddington ratio can remain stable at $\hat{f}_{\text{Edd},16}$. In this regime, a lower W_{circ} implies that the inflowing angular momentum is smaller, enabling the disc to sustain $f_{\text{Edd},16} \sim \hat{f}_{\text{Edd},16}$ for a longer duration. Consequently, runs with a smaller W_{circ} exhibit longer alignment time-scales. However, for runs with $W_{\text{circ}} \geq 0.5$, the strong angular momentum inflow leads to an increase in J_{disc} , which in turn causes $f_{\text{Edd},16}$ to decrease, preventing the system from reaching $f_{\text{Edd},16} \sim \hat{f}_{\text{Edd},16}$. In this case, the alignment time-scale becomes longer for larger values of W_{circ} because the resulting lower $f_{\text{Edd},16}$ leads to a weaker Lense-Thirring torque within the Bardeen-Petterson configuration.

In the third column of Figure 8, we present the effects of varying $a_{\text{BH},0}$. We include the runs aBH-VL, aBH-L, Fiducial, and aBH-H, with $a_{\text{BH},0} = 0.2, 0.5, 0.8$, and 0.99 , respectively. All these runs exhibit a similar stable state at $f_{\text{Edd},16} \sim \hat{f}_{\text{Edd},16}$. A larger $a_{\text{BH},0}$ results in a higher value of $\hat{f}_{\text{Edd},16}$ (Equation 35) and prolongs the duration over which the system remains at $f_{\text{Edd},16} \sim \hat{f}_{\text{Edd},16}$, due to the larger magnitude of the BH angular momentum.

In the fourth column of Figure 8, we display the results of

varying $\theta_{\text{BH-disc},0}$ by comparing the runs theta-VL, theta-L, and Fiducial, with $\theta_{\text{BH-disc},0} = \pi/2, 3\pi/2$, and $5\pi/6$, respectively. All these runs show a similar stable state at $f_{\text{Edd},16} \sim \hat{f}_{\text{Edd},16}$. A smaller initial misalignment angle between the BH and the disc results in a shorter duration at this state, as the BH aligns with the disc more rapidly.

The left-hand column of Figure 9 presents the results of varying the Toomre parameter by comparing the runs Q-VH, Q-H, Fiducial, and Q-L, with $Q_{\text{min}} = 4, 2, 1$, and 0.5 , respectively. The evolution of $f_{\text{Edd},16}$, $\theta_{\text{BH-disc}}$, M_{disc} , and J_{disc} is shown in the figure. As in all other runs, M_{disc} remains equal to M_{sg} , since the inflow of mass is sufficient to maintain this condition. Consequently, the value of Q_{min} sets the size of the accretion disc, with a higher Q_{min} producing a smaller disc. Although values such as $Q_{\text{min}} = 0.5$ or $Q_{\text{min}} = 4$ may be physically unrealistic, they are included to explore how different disc sizes may influence the results.

For the Q-H, Fiducial, and Q-L runs, $f_{\text{Edd},16}$ remains at $f_{\text{Edd},16} \sim \hat{f}_{\text{Edd},16}$ for approximately 1 Myr. After $\theta_{\text{BH-disc}}$ decreases and the system exits this state, a larger Q_{min} leads to a more rapid decline in $f_{\text{Edd},16}$, as it corresponds to a smaller disc, making the relative changes in J_{disc} more significant.

For the Q-VH run, in which $Q_{\text{min}} = 4$, we also plot the evolution of $\theta_{\text{gas-disc}}$ for comparison. The disc angular momentum is slightly smaller than the BH angular momentum, i.e. $J_{\text{disc}} \lesssim J_{\text{BH}}$, due to the reduced disc size. When $\theta_{\text{BH-disc}} > \pi/2$, the alignment torque acting on the BH pulls the BH angular momentum towards the disc, while the corresponding torque on the disc pushes the disc angular momentum further away from the BH, owing to conservation of

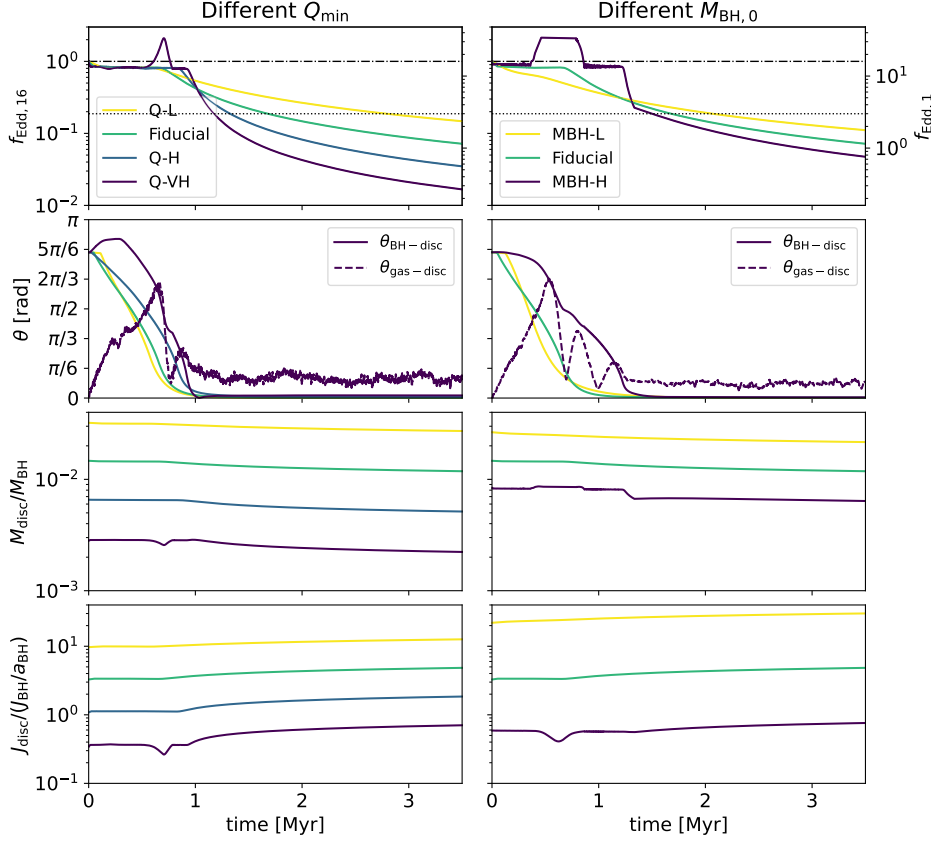


Figure 9. Time evolution of BH-disc quantities for different values of Q_{\min} (left-hand column) and $M_{\text{BH},0}$ (right-hand column). From top to bottom: $f_{\text{Edd},16}$ (with $f_{\text{Edd},1}$ on the right axis for comparison), $\theta_{\text{BH-disc}}$ (solid line), $M_{\text{disc}}/M_{\text{BH}}$, and $J_{\text{disc}}/(J_{\text{BH}}/a_{\text{BH}})$. In the top row, the black dash-dotted line marks $f_{\text{Edd},16} = 1$, whereas the dotted line indicates $f_{\text{Edd},1} = 3$. The Fiducial run is shown in green for reference. The evolution of $\theta_{\text{gas-disc}}$ is shown in the second row only for the Q-VH and MBH-H runs (purple dashed lines). These two runs have smaller discs with lower J_{disc} , resulting in a misalignment between the disc and the gas. This enables efficient removal of disc angular momentum through misaligned inflow, allowing the system to reach $f_{\text{Edd},16} \gtrsim 2$ for a brief period.

angular momentum. Since $J_{\text{disc}} \lesssim J_{\text{BH}}$, the Lense-Thirring torque has a stronger effect on the disc than on the BH. Together with the influence of the precession torque, this causes $\theta_{\text{gas-disc}}$ to increase significantly from its initial value of zero, because the disc deviates from its original orientation.

Once $\theta_{\text{gas-disc}}$ exceeds $\pi/2$, the continued accretion of misaligned gas further decreases J_{disc} , leading to a substantial drop in J_{disc} and driving $f_{\text{Edd},16}$ above $\hat{f}_{\text{Edd},16}$. In this simulation, $f_{\text{Edd},16}$ reaches a peak of approximately 2. The strong inflow of angular momentum onto the disc then rapidly decreases both $\theta_{\text{BH-disc}}$ and $\theta_{\text{gas-disc}}$. Similarly, once the BH becomes nearly aligned with the disc, $f_{\text{Edd},16}$ decreases rapidly due to the weak Lense-Thirring torque.

In the right-hand column of Figure 9, we present the results of varying $M_{\text{BH},0}$ by comparing the MBH-L, Fiducial, and MBH-H runs, with $M_{\text{BH},6} = 0.1, 1$, and 10 , respectively. Since $R_{\text{sg}}/R_{\text{g}}$ decreases as M_{BH} increases (Section 2.5), a more massive BH leads to an initially smaller $M_{\text{disc}}/M_{\text{BH}}$ and $J_{\text{disc}}/J_{\text{BH}}$. In the MBH-L run, the larger value of J_{disc} reduces the relative influence of the Lense-Thirring torque on J_{disc} . Furthermore, since $R_{\text{circ}} \propto R_{\text{sg}}$, the angular momentum inflow onto the disc is also larger. Consequently, the combined effect of these factors leads to an increase in J_{disc} , preventing the system from reaching $f_{\text{Edd},16} \sim \hat{f}_{\text{Edd},16}$.

For the MBH-H run, we also plot the evolution of $\theta_{\text{gas-disc}}$. As in the Q-VH run, $f_{\text{Edd},16}$ can exceed the critical value $\hat{f}_{\text{Edd},16}$ due to the smaller disc ($J_{\text{disc}} \lesssim J_{\text{BH}}$). A smaller R_{sg} associated with a larger BH mass also helps sustain a higher mass accretion rate by providing a smaller angular momentum inflow. In this run, $f_{\text{Edd},16}$ reaches its maximum value $f_{\text{Edd},16,\text{max}} \sim 2$ when $t \sim 0.4\text{--}0.8$ Myr. The alignment time is also longer in this run, as the system remains in the $f_{\text{Edd},16} > \hat{f}_{\text{Edd},16}$ regime, wherein the alignment process is much slower, for an extended duration.

Interestingly, in this setup, a more massive BH exhibits higher mass accretion rates, resulting in larger BH mass growth. This is counter-intuitive, since the mass inflow rate needed to go above Eddington levels increases linearly with BH mass. The main reason is that $J_{\text{disc}}/J_{\text{BH}}$ decreases with increasing M_{BH} , and a smaller $J_{\text{disc}}/J_{\text{BH}}$ enhances the influence of Lense-Thirring torques. Moreover, in our setup, there is always sufficient gas surrounding the BH to sustain a lasting inflow. However, different initial conditions (both in the sub-grid model and the surrounding gas) may not yield the same outcome.

In Figure 10, we present the evolution of j_{BH} and j_{disc} for the Q-VH and MBH-H runs via Hammer projections. In both cases, $J_{\text{disc}} \lesssim J_{\text{BH}}$. Due to conservation of angular momen-

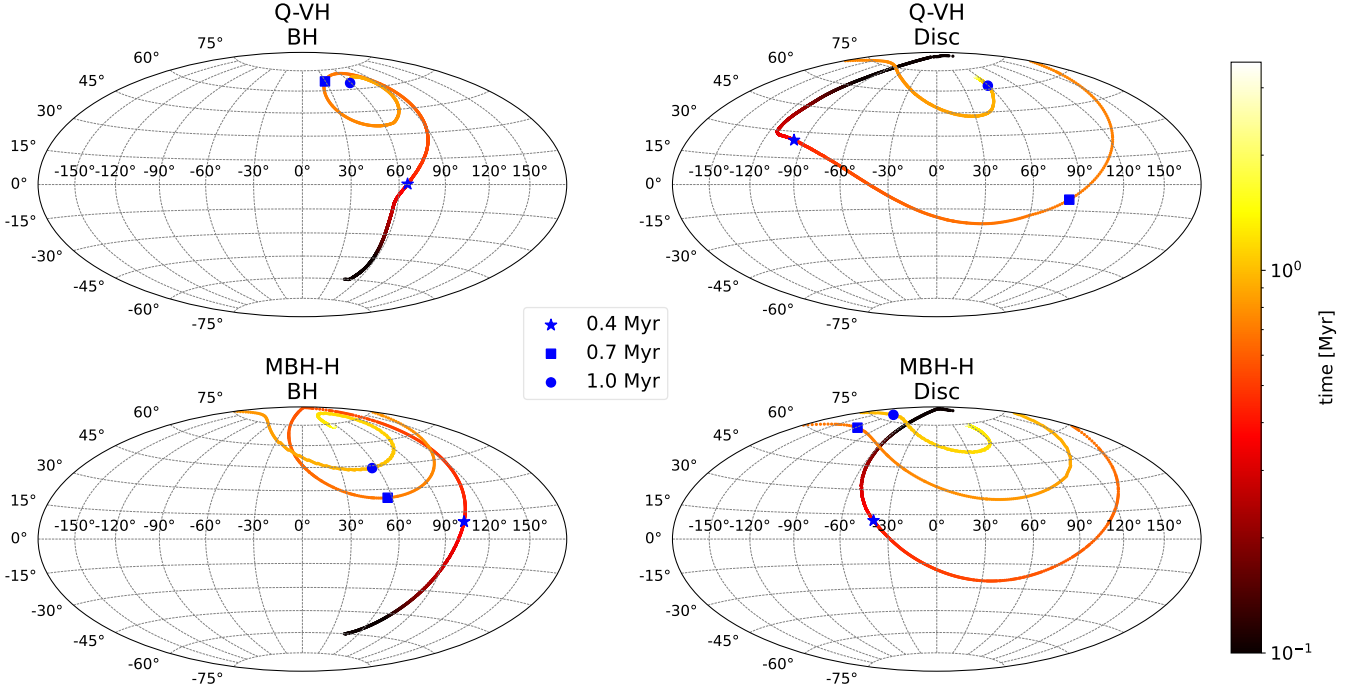


Figure 10. Evolution of the BH (left panels) and disc (right panels) angular momenta for the Q-VH (top row) and MBH-H (bottom row) runs, shown via Hammer projections wherein the equatorial plane is defined by the angular momentum of the gas within the BH kernel of the initial conditions (before relaxation). The blue markers highlight specific time stamps at 0.4 (star), 0.7 (square), and 1 Myr (circle). In both runs, the direction of \mathbf{j}_{gas} is nearly aligned with the z -axis and is therefore omitted. Both runs feature a smaller disc ($J_{\text{disc}} < J_{\text{BH}}$), which causes the disc to be pushed away from its initial direction and leads to pronounced precession between the BH and the disc.

tum, the Lense-Thirring torque pushes the disc away from its initial direction, leading to an increase in $\theta_{\text{gas-disc}}$. As a result of both the Lense-Thirring torque and gas inflow, the BH gradually aligns with the disc and surrounding gas, while exhibiting strong precessional motion. For these two runs, the initial condition does not satisfy the alignment criterion proposed by King et al. (2005), given by Equation (38). However, the BH and disc do not become counter-aligned. Although a slight increase in $\theta_{\text{BH-disc}}$ is observed in the Q-VH run, the BH and disc still ultimately align within approximately 1 Myr. This outcome arises because $R_{\text{disc}} > R_{\text{warp}}$, meaning that the time-scale to reach counter-alignment is not negligible. During this period, the angular momentum inflow can significantly modify the disc angular momentum, thereby preventing the system from reaching counter-alignment.

4.3 Initial BH-disc alignment

In this section, we consider the BH-disc alignment initial condition, when the gas surrounding the BH is misaligned with the BH-disc system, and the BH is aligned with the disc, i.e. $\theta_{\text{BH-disc},0} = 0$ and $\theta_{\text{gas-disc},0} \neq 0$.

In Figure 11, we show the results of the GD-Misalign-VH run using our model and that of C21. These two models produce significantly different outcomes.

In our model, $f_{\text{Edd},16}$ rises rapidly at the beginning and reaches $f_{\text{Edd},16,\text{max}} \sim 20$. This occurs because the inflow of angular momentum from the surrounding gas onto the accretion disc significantly reduces J_{disc} , due to the misalignment between the gas and the disc. The decrease of J_{disc} leads to a

high BH mass accretion rate. The strong mass inflow onto the disc at $f_{\text{Edd},16} \sim 20$ results in the rapid alignment of the disc and BH with the surrounding gas within the first 0.5 Myr. After $t > 0.5$ Myr, as the BH, disc, and gas become nearly aligned, J_{disc} begins to increase due to the gas inflow, which subsequently decreases $f_{\text{Edd},16}$.

By contrast, in the C21 model, the imposed limit of $f_{\text{Edd},\eta} \leq 1$ prevents the model from capturing the effects of high mass accretion rates. The strong reduction in J_{disc} due to the gas inflow onto the disc does not translate into an increased Eddington ratio because of this cap. As a result, $f_{\text{Edd},16}$ remains at approximately 0.5 for around 7 Myr, and the BH aligns with the surrounding gas much more slowly than in our model.

In our model, M_{disc} shows a notable bump at $t \sim 0.5$ Myr, when $f_{\text{Edd},16} \sim f_{\text{Edd},16,\text{max}}$. This occurs because the value of M_{sg} is substantially larger at $f_{\text{Edd},16,\text{max}}$. In the model by C21, M_{disc} varies only slightly over the first 7 Myr, as $f_{\text{Edd},16}$ remains nearly constant during this period. Both models show a significant reduction in J_{disc} due to the misaligned gas inflow, although the time-scale of this decrease differs considerably owing to the different mass accretion rates.

During this time interval, a_{BH} increases from 0.8 to 0.9 in both models, due to the BH mass accretion from a prograde accretion disc. Our model results in a 15 per cent increase in the BH mass within the first 0.5 Myr. By contrast, the model of C21 shows a smaller BH mass growth, even over 10 Myr.

In Figure 12, we illustrate the evolution of the direction of \mathbf{j}_{BH} and \mathbf{j}_{disc} for both models, projected onto the full-sky sphere using Hammer projections. In both models, the BH

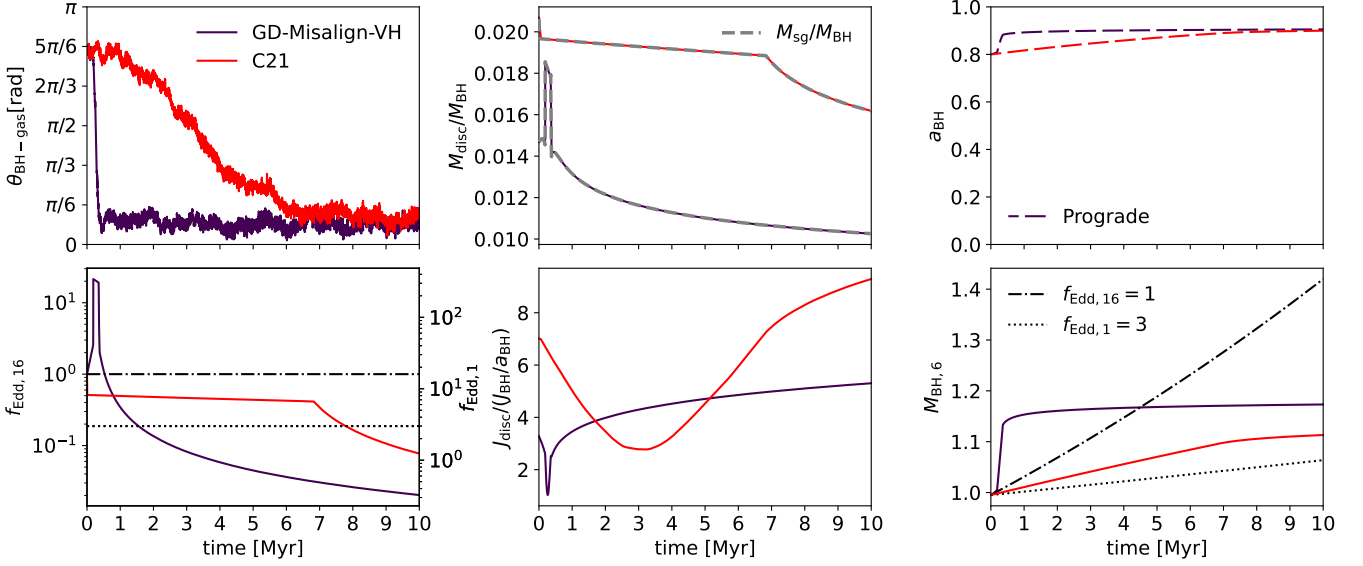


Figure 11. Comparison of the GD-Misalign-VH run using our model (purple) and the model by C21 (red). Similar to Figure 6, from left to right and from top to bottom: time evolution of $\theta_{\text{BH-gas}}$, $M_{\text{disc}}/M_{\text{BH}}$ (with M_{sg} shown as a grey dashed line), a_{BH} (the dashed line indicating that the disc remains prograde), $f_{\text{Edd},16}$ (with $f_{\text{Edd},1}$ on the right axis; dash-dotted and dotted lines show $f_{\text{Edd},16} = 1$ and $f_{\text{Edd},1} = 3$), $J_{\text{disc}}/(J_{\text{BH}}/a_{\text{BH}})$, and $M_{\text{BH},6}$ (with reference tracks for $f_{\text{Edd},16} = 1$ and $f_{\text{Edd},1} = 3$). The two models show significantly different results. For both runs, J_{disc} decreases substantially due to the misaligned gas inflow onto the disc. In our model, we capture the rise of $f_{\text{Edd},16}$ to $f_{\text{Edd},16,\text{max}} \sim 20$ as a result of this decrease, whereas C21 impose a (lower) cap at $f_{\text{Edd},\eta} = 1$ and therefore cannot model this increase in $f_{\text{Edd},16}$.

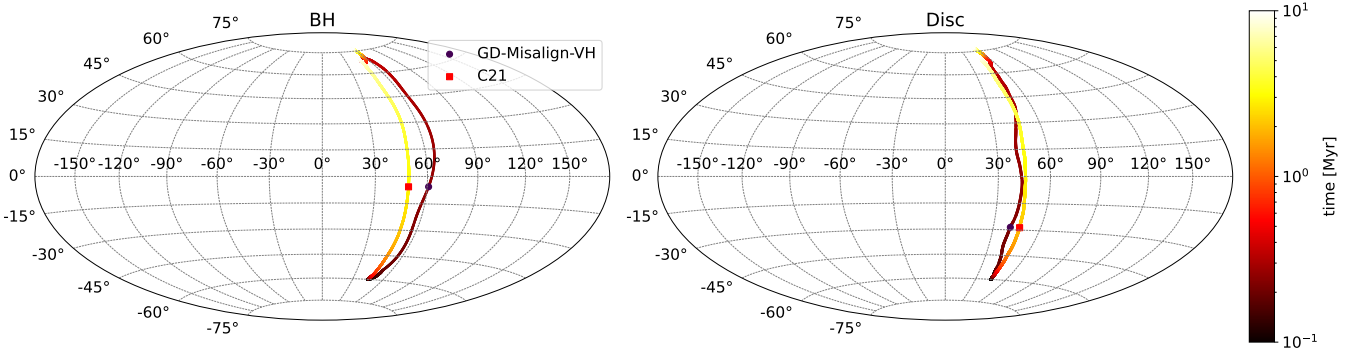


Figure 12. Evolution of the BH (left-hand panel) and disc (right-hand panel) angular momenta for the GD-Misalign-VH run using our model (purple) and the model by C21 (red), shown via Hammer projections wherein the equatorial plane is defined by the angular momentum of the gas within the BH kernel of the initial conditions (before relaxation). The colour bar indicates time evolution from 0.1 to 10 Myr. In both models, the direction of \mathbf{j}_{gas} is nearly aligned with the z -axis and is therefore omitted. Our model shows faster alignment and slightly stronger precession motion of both the BH and disc angular momentum vectors compared to C21, due to the higher $f_{\text{Edd},16}$ at early times, driven by the misaligned gas inflow.

and disc progressively align with the gas direction (which is approximately aligned with the z -axis). In our model, the time-scale for alignment is significantly shorter, as a larger $f_{\text{Edd},16}$ drives a stronger inflow of angular momentum onto the disc. Moreover, our model also exhibits a more pronounced precession between the BH and the disc, although it is relatively mild in this scenario, as the misalignment angle between the BH and the disc is generally small.

This initial condition clearly highlights the importance of incorporating the super-Eddington model when the angular

momentum of the surrounding gas is misaligned with the accretion flow.

Figure 13 compares the runs Fiducial, GD-Misalign-L, GD-Misalign-H, and GD-Misalign-VH. The Fiducial run adopts the gas-disc alignment initial condition, whereas the other three runs adopt the BH-disc alignment initial condition, with $\theta_{\text{gas-disc},0} = 2\pi/3, 3\pi/4$, and $5\pi/6$, respectively.

Comparing the three GD-Misalign runs, we can see that a larger $\theta_{\text{gas-disc},0}$ results in a higher mass accretion rate, resulting in a faster alignment between the BH and the surrounding gas. We observe that the maximum Eddington ratio

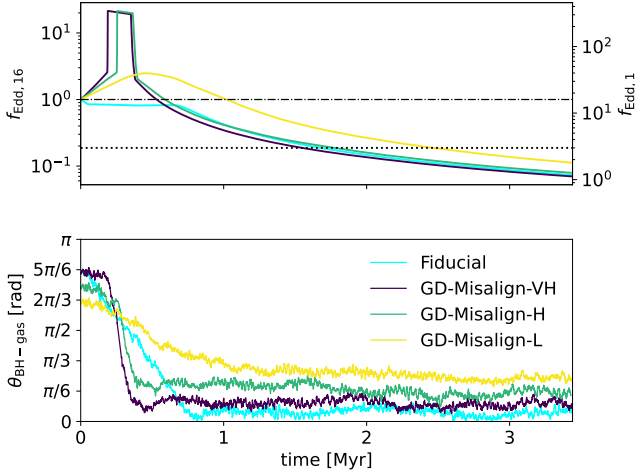


Figure 13. Time evolution of $f_{\text{Edd},16}$ (top panel, with $f_{\text{Edd},1}$ shown on the right axis for comparison) and misalignment angle between the BH and the surrounding gas, $\theta_{\text{BH-gas}}$ (bottom panel), for the Fiducial, GD-Misalign-L, GD-Misalign-H, and GD-Misalign-VH runs. All GD-Misalign runs adopt the gas-disc alignment initial conditions and exhibit a higher peak in $f_{\text{Edd},16}$ compared to the Fiducial case. This is because the misaligned gas inflow efficiently reduces the disc angular momentum, enabling short-lived phases of enhanced accretion. In particular, the GD-Misalign-VH and GD-Misalign-H runs reach $f_{\text{Edd},16} = f_{\text{Edd},16,\text{max}} \sim 20$, which drives a faster alignment between the BH and the gas.

in the GD-Misalign-L run is approximately an order of magnitude lower than in the other two runs. This difference arises because M_{sg} is not a strictly monotonic function of $f_{\text{Edd},16}$, due to the complex structure of the accretion disc structure. In particular, for $2 \lesssim f_{\text{Edd},16} \lesssim 2.5$, M_{sg} slightly decreases with increasing $f_{\text{Edd},16}$. However, once $f_{\text{Edd},16} \gtrsim 2.5$, M_{sg} increases rapidly with $f_{\text{Edd},16}$. As a result, once $f_{\text{Edd},16}$ exceeds this threshold, the corresponding rise in M_{sg} drives a stronger inflow onto the accretion disc. This enhanced inflow further reduces the disc angular momentum, leading to a significantly higher mass accretion rate.

Comparing the GD-Misalign runs with the Fiducial run, we can see that at the beginning of the simulation, the Fiducial run consistently shows a smaller $f_{\text{Edd},16}$ because it cannot effectively reduce J_{disc} due to the combined effect of the Lense-Thirring torque models for low and high mass accretion rates. However, the GD-Misalign runs can reduce J_{disc} effectively through the misaligned gas inflow onto the disc. As a result, the GD-Misalign runs exhibit a larger maximum $f_{\text{Edd},16}$, particularly for larger $\theta_{\text{gas-disc},0}$. For the GD-Misalign-VH and GD-Misalign-H runs, the alignment between the BH and the gas proceeds much more rapidly than in the Fiducial run due to the significantly higher $f_{\text{Edd},16}$. It is worth noting that the final value of $\theta_{\text{BH-gas}}$ is larger for the GD-Misalign runs, especially in the GD-Misalign-L run. This is because, as the system approaches alignment, the gas inflow is no longer able to efficiently reduce J_{disc} , leading to a lower $f_{\text{Edd},16}$, resulting in inefficient final alignment.

5 DISCUSSION

We developed a new sub-grid model for the evolution of BH mass and spin that incorporates super-Eddington accretion, regulated via an accretion disc-mediated growth. Our work builds upon the model proposed by C21. We conducted a suite of simulations in idealised setups to test the model and investigate the evolution of the BH. In Section 5.1, we discuss the relevance of super-Eddington accretion based on our simulation results. In Section 5.2, we discuss a few potential caveats of our model.

5.1 Relevance of super-Eddington accretion

We begin by examining the simulations in which the surrounding gas is initially aligned with the accretion disc but the BH is initially misaligned with both (i.e. gas-disc alignment initial conditions: $\theta_{\text{gas-disc},0} = 0$ and $\theta_{\text{BH-disc},0} \neq 0$). In this setup, the BH initially experiences a moderately high accretion rate, when the BH is not aligned with the disc, as the Lense-Thirring torque efficiently reduces the disc angular momentum. However, the system can typically sustain an accretion rate of at most $f_{\text{Edd},16} \sim \hat{f}_{\text{Edd},16}$ for about 1 Myr, even with sufficient gas inflow (Figure 8). The value of $\hat{f}_{\text{Edd},16}$ is around 0.9 for all runs with $a_{\text{BH}} \sim 0.8$. This limitation arises from the two torque models employed in the simulation. Since the torque model for higher mass accretion rates is less efficient at reducing J_{disc} , $f_{\text{Edd},16}$ cannot significantly exceed $\hat{f}_{\text{Edd},16}$. If the disc is smaller, due to a larger Q_{min} or a larger M_{BH} , a higher mass accretion rate is achievable due to a lower $J_{\text{disc}}/J_{\text{BH}}$ (Figure 9). This can result in a greater misalignment between the disc and the surrounding gas, allowing inflows to further decrease the disc angular momentum. This suggests that, even when incorporating a more detailed accretion disc structure and torque models suited to super-Eddington accretion, a system starting with gas-disc alignment initial conditions often exhibits an emerging “Eddington cap”, with the accretion rate stabilising around $f_{\text{Edd},16} = \hat{f}_{\text{Edd},16} \sim 1$ (i.e. $f_{\text{Edd},1} \gtrsim 10$) for rapidly spinning BHs (Figure 4). Interestingly, although arising from different physical mechanisms, this behaviour aligns with the commonly adopted upper limit on BH mass accretion rates in various BH growth models and simulations focused on sub-Eddington accretion ($f_{\text{Edd},\eta} \sim 1$, with $\eta \sim 0.1$; e.g. Dubois et al. 2014; Weinberger et al. 2017; Fiacconi et al. 2018; Bus-tamante & Springel 2019; C21).

If we consider a different initial condition, in which the BH is aligned with the disc but both are misaligned with the surrounding gas (i.e. BH-disc alignment initial conditions: $\theta_{\text{gas-disc},0} \neq 0$ and $\theta_{\text{BH-disc},0} = 0$), the misaligned inflow can significantly reduce J_{disc} . Under these conditions, our simulations show that the system can reach $f_{\text{Edd},16} \sim 20$ with $M_{\text{BH},6} = 1$ (Figure 11). However, even in this scenario, $f_{\text{Edd},16} > 1$ is maintained for less than 1 Myr, as the BH and the disc rapidly align themselves with the surrounding gas. Despite its short duration, the large Eddington ratio leads to a significant increase in BH mass (by up to ~ 15 per cent) over this brief time-scale.

In this case, the direction of the angular momentum inflow onto the accretion disc plays a crucial role in determining the BH mass growth rate. If a new inflow of misaligned gas enters the centre of the galaxy, a configuration similar to the

BH-disc alignment initial condition might emerge, provided that the BH and disc were originally aligned (which is always the case at the end of our simulations). A misaligned inflow would enhance the mass accretion rate, potentially leading to super-Eddington accretion. However, this process is highly non-linear, making it challenging to predict without detailed simulations. This highlights the importance of considering the direction of the angular momentum of the gas surrounding the accretion disc in order to better estimate the rate of BH growth.

In general, reducing the disc angular momentum is crucial for sustaining a high mass accretion rate. Otherwise, the mass accretion rate onto the BH can remain low, even if the BHL accretion rate is potentially large. One mechanism for reducing J_{disc} is via the Lense-Thirring torque, but in our simulations this effect can bring $f_{\text{Edd},16}$ to at most ~ 1 . Another approach is through the inflow of low-angular-momentum and/or misaligned gas, which could lead to a larger mass accretion rate ($f_{\text{Edd},16} = f_{\text{Edd},16,\text{max}} \sim 20$ for $M_{\text{BH},6} = 1$). Such inflows may arise from chaotic cosmic accretion, disturbed morphologies in proto-galaxies, merger events, starbursts, gravitational instabilities, or non-axisymmetric gravitational torques (e.g. Shlosman et al. 1989; Hopkins & Quataert 2010; Capelo & Dotti 2017; Blumenthal & Barnes 2018; see Capelo et al. 2023 for a recent review). Additionally, turbulence on scales slightly larger than those of the accretion disc can induce chaotic accretion, contributing to the efficient removal of disc angular momentum and thereby promoting sustained high accretion rates (Dotti et al. 2013; Fiacconi et al. 2018).

In high-redshift environments, it is more frequent to have chaotic gas accretion onto the (proto-)galaxy, a highly turbulent gas kinematics, and galaxy-galaxy interactions, leading to more frequent strong and misaligned inflows onto the accretion disc (Gabor & Bournaud 2014; Danhaive et al. 2025; Duan et al. 2025). In such cases, super-Eddington accretion might be (re-)triggered when a misaligned inflow occurs, making episodic super-Eddington accretion in the early Universe a plausible mechanism for facilitating rapid BH growth (Volonteri et al. 2015; Khoperskov et al. 2021). However, the detailed exploration of this scenario is left for future work.

Sassano et al. (2023) modelled BH growth and feedback in the super-Eddington regime in simulations of the central region of a proto-galaxy, starting from an initial BH mass of $M_{\text{BH}} = 10^3 M_{\odot}$. Similar to our findings, they found that the BH accretion is quenched after approximately 1 Myr. However, the BH in their simulations accretes up to $\sim 10^4 M_{\odot}$ within this time-frame, corresponding to a growth of more than an order of magnitude – substantially higher than our results. Zana et al. (in prep.), using an improved version of the code used by Sassano et al. (2023) and different initial conditions, obtain even larger growth rates (of the order of $\lesssim 10^5 M_{\odot}$ in less than 1 Myr). Part of this discrepancy may arise from their use of BHL accretion rates for the BH accretion rate, which neglects the angular momentum of the inflowing gas and thus overestimates the accretion rate.

We extrapolate our results to estimate the growth of a BH from $z = 11$ down to $z = 6$, using a simple calculation that consider a sequence of episodic super-Eddington accretion events, following the approach of Sassano et al. (2023). We consider a BH at $z = 11$ with an initial mass of $M_{\text{BH},z=11} = 10^6 M_{\odot}$, consistent with a massive BH seed formed via direct collapse in Mayer et al. (2024) and with

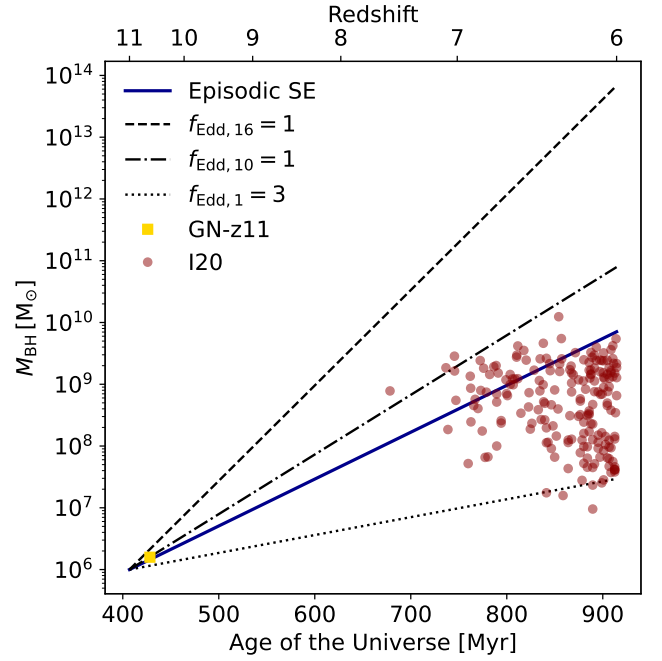


Figure 14. Time evolution of BH mass from $z = 11$ to $z = 6$, from an initial value of $M_{\text{BH}} = 10^6 M_{\odot}$. The blue line shows BH growth via episodic super-Eddington accretion (Episodic SE), assuming a dynamic time-scale of $t_{\text{dyn}} = 2$ Myr, a misaligned inflow fraction of $p_{\text{mis}} = 0.25$, and a mass increase of $\Delta M_{\text{BH}}/M_{\text{BH}} = 0.15$ during each misaligned inflow event. The dashed, dash-dotted, and dotted lines correspond to constant specific accretion rates of $f_{\text{Edd},16} = 1$, $f_{\text{Edd},10} = 1$, and $f_{\text{Edd},1} = 3$, respectively. The yellow square denotes GN-z11 (Maiolino et al. 2024), whereas the dark red circles represent 196 quasars observed at $z \geq 6$, taken from the supplemental table in Inayoshi et al. (2020; I20). This figure shows that our model can potentially reproduce the most massive BHs observed at $z = 6$.

GN-z11, observed by Maiolino et al. (2024). Sassano et al. (2023) showed that the dynamical time-scale at the centre of a galaxy is $t_{\text{dyn}} = 2$ Myr, corresponding to the typical time required for gravitational torques and dynamical instabilities to replenish the gas within the central 2 pc. We assume that the minimum time between new gas inflows is t_{dyn} , yielding a maximum of $N_{\text{max}} = 253$ inflow events between $z = 11$ and $z = 6$. We define p_{mis} as the fraction of these events involving misaligned gas inflows capable of triggering super-Eddington accretion. Based on Figures 11 and 13, we assume that, if $\theta_{\text{gas-disc}} > 2\pi/3$, the resulting misaligned gas inflow can lead to rapid BH growth, with $\Delta M_{\text{BH}}/M_{\text{BH}} = 0.15$ within 1 Myr.¹⁵ For simplicity, we assume that the angular momentum of the inflowing gas is isotropically distributed in

¹⁵ One important difference between this calculation and that of Sassano et al. (2023) is that we assume a fixed $\Delta M_{\text{BH}}/M_{\text{BH}}$ (i.e. a fixed $f_{\text{Edd},16}$; as in Regan et al. 2019) for each event, whereas they assume a fixed ΔM_{BH} . We adopt this approach because our simulations always feature sufficient gas inflow onto the accretion disc. Therefore, we expect that, for a more massive BH, similar growth rates can be sustained due to the available gas reservoir. However, both a fixed $\Delta M_{\text{BH}}/M_{\text{BH}}$ and a fixed ΔM_{BH} are strong assumptions, as the actual BH growth rates should also depend on

each event, which gives $p_{\text{mis}} = 0.25$. Thus, the final BH mass at $z = 6$ is

$$M_{\text{BH},z=6} = M_{\text{BH},z=11} \left(1 + \frac{\Delta M_{\text{BH}}}{M_{\text{BH}}} \right)^{N_{\text{max}} p_{\text{mis}}} \quad (57)$$

$$= 6.9 \times 10^9 M_{\odot},$$

which is consistent with the most massive BHs observed at $z \sim 6$ (e.g. Inayoshi et al. 2020; Fan et al. 2023). The corresponding BH growth rates are equivalent to an overall effective Eddington ratio of $f_{\text{Edd},16} = 0.53$ (i.e. $f_{\text{Edd},\eta}/\eta_{0.1} = f_{\text{Edd},10} = 0.84$, $f_{\text{Edd},1} = 8.4$).

The results of this calculation are shown in Figure 14. The GN-z11 source (Maiolino et al. 2024) and 196 quasars observed at $z \sim 7.5$ –6, listed in Inayoshi et al. (2020), are also included for comparison. Our results successfully reproduce the most massive BHs observed at $z \sim 6$, but fall slightly short by approximately an order of magnitude at $z \sim 6.5$ to 7.5. We also note that, if we begin with a low-mass seed (e.g. $10^3 M_{\odot}$; Sassano et al. 2021), the final mass would be much lower, even when starting at a much earlier redshift. Additionally, the figure displays the BH mass growth under a constant specific accretion rate of $f_{\text{Edd},16} = 1$, $f_{\text{Edd},10} = 1$, and $f_{\text{Edd},1} = 3$, which correspond to three common definitions of super-Eddington accretion in the literature: we note that the choice of definition for super-Eddington accretion substantially impacts the final M_{BH} , as illustrated in the figure.

Both Regan et al. (2019) and Massonneau et al. (2023b) conduct high-resolution hydrodynamics simulations to investigate BH growth, allowing for super-Eddington accretion in the presence of BH feedback. In both studies, episodic super-Eddington accretion is found, as BH feedback expels gas from the surrounding region, which is later replenished via inflows. Regan et al. (2019) reported an effective Eddington ratio of $f_{\text{Edd},10} \sim 0.1$ –0.5 (i.e. $f_{\text{Edd},16} \sim 0.06$ –0.3), whereas Massonneau et al. (2023b) found that an effective Eddington ratio of $f_{\text{Edd},10} \sim 1$ (i.e. $f_{\text{Edd},16} \sim 0.6$) can be achieved when jet feedback efficiencies are weak. Although both studies yield mass accretion rates comparable to ours, the cumulative growth of M_{BH} from $z = 11$ to $z = 6$ can differ by more than an order of magnitude. The discrepancy in effective Eddington ratios may arise from the inclusion of BH feedback, as well as differences in BH accretion prescriptions and initial BH mass.

5.2 Caveats

5.2.1 Accretion disc structure

In this paper, we modelled the accretion disc structure by combining the fitting formulae for the photon-trapping region from simulations by K18 with the three regions of the thin α -disc. We selected K18 because they provide fitting formulae for the disc structure across a wide range of values of $f_{\text{Edd},16}$ and M_{BH} . However, we note that different simulations and theoretical models predict varying structures for the photon-trapping region. We compared the results from

K18 to those of Watarai (2006) and Sądowski (2011) in Section 2.2. Simulations that include magnetic fields and/or GR effects may yield more significant differences (e.g. Sądowski & Narayan 2016; Jiang et al. 2019; Hu et al. 2022a). Furthermore, we renormalise the surface density and specific angular momentum profiles of this inner region to ensure continuity. While these differences may not strongly affect the calculation of the BH mass accretion rate as a function of M_{disc} and J_{disc} , they could influence the magnitude of the Lense-Thirring torque exerted by the inner precessing thick disc in the photon-trapping region.

Furthermore, the simulations in K18 assumed a constant $\alpha = 0.1$. Even though many of our equations are formulated for a generic α , using different values of α in our model may lead to an inaccurate representation of the photon-trapping region structure. In addition, GRMHD simulations predict significant radial variations in α (e.g. Jiang et al. 2019; Liska et al. 2021). Moreover, we adopt $\xi = 0.7$ in this study, consistent with $\alpha = 0.1$ (Lodato & Pringle 2007): a different value of α would imply a different value of ξ (Lodato & Pringle 2007; Perego et al. 2009). The parameter ξ affects the Lense-Thirring torque through R_{warp} , t_{gm} , and $f_{\text{Edd},16}$.

The surface density and specific angular momentum profiles of the disc used in this work are all derived assuming a non-spinning BH. If the effects of BH spin are taken into consideration, the disc structure might be altered in the innermost regions near the event horizon. We neglected this effect, as the integral properties of the disc are dominated by the outer parts, and thus it does not significantly affect our results.

The thin α -disc model is widely used to describe the structure of accretion discs due to its simplicity and success at explaining many observed properties of such systems (Abramowicz & Fragile 2013). Accordingly, we adopt it to describe the disc where $R_{\text{disc}} \geq R_{\text{trap}}$. However, several fundamental questions remain unsolved. For instance, it has difficulties accounting for the variability commonly observed in AGN (e.g. Burke et al. 2021), as well as the discrepancy between observed disc sizes and theoretical predictions (e.g. Dai et al. 2010).

In our model, we impose $f_{\text{Edd},16} \leq f_{\text{Edd},16,\text{max}}$ to avoid the “degeneracy” behaviour in the $(M_{\text{disc}}, J_{\text{disc}})$ parameter space discussed in Appendix C, which arises when region (a) dominates the accretion disc structure. By doing this, we effectively ignore region (a) for the mass accretion rate calculations, but we note that we still include this region for the torque computations. This constraint prevents us from studying the evolution of the BH when the Eddington ratio exceeds this limit. We note, however, that this limit is much higher than the usually applied Eddington limit for a wide range of BH and disc masses, and it becomes low only for very massive BHs and/or the extreme case of a nearly depleted accretion disc. Furthermore, region (a) of the disc is both viscously and thermally unstable in the thin α -disc theory (Lightman & Eardley 1974). These instabilities might produce a different disc structure than what assumed in this work, and the degeneracy might disappear. However, these instabilities are not observed in the simulations conducted by Kitaki et al. (2021), and the underlying reasons remain unclear (King et al. 2023).

Another caveat is that our model is not applicable at very low mass accretion rates ($f_{\text{Edd},16} \lesssim 10^{-2}$), when the inner-

several other factors, such as the surrounding gas mass, dynamics, temperature, and the BH mass and spin.

most part ($R < R_{\text{tran}}$ in Figure 2) of the accretion disc transitions into an ADAF that cannot be adequately described by the thin α -disc model. In contrast to our approach, Koudmani et al. (2024) extends the sub-grid model of Fiacconi et al. (2018) to include this regime by coupling an inner ADIOS flow with an outer thin α -disc.

Furthermore, the viscous time-scale, t_{visc} , for the thin α -disc at R_{disc} is approximately 0.1–1 Myr in our model. This implies that if the disc structure changes rapidly on a time-scale shorter than t_{visc} , the results may be inaccurate, as the system does not have sufficient time to reach a stable and stationary accretion disc configuration. In contrast, Tarténas & Zubovas (2022) explicitly model the viscous evolution of the disc surface density to account for this situation. They find that including viscous evolution leads to a reduced and more extended BH accretion rate and alters the impact of BH feedback on the surrounding gas, compared to the BHL prescription, in simulations of collisions between a gas ring and a molecular cloud in the galactic centre.

Additionally, we do not incorporate the effects of magnetic fields in our model. Magnetorotational instability turbulence is believed to be one of the primary mechanisms responsible for the generation of viscosity, which facilitates the transport of angular momentum within the accretion disc (Balbus & Hawley 1991). The presence of strong magnetic pressure can substantially influence the dynamics and structure of accretion flows (e.g. Narayan et al. 2003; Hopkins et al. 2024). Moreover, the interaction between magnetic fields and a spinning BH provides a mechanism for jet launching via the Blandford-Znajek process (Blandford & Znajek 1977). Incorporating magnetic effects in future studies could further refine our understanding of SMBH evolution and its impact on jet formation and strength.

As discussed in Section 2.5, we impose the limit that $R_{\text{disc}} < R_{\text{sg}}$ to prevent the disc from becoming self-gravitating. However, if the local cooling time is not sufficiently short at $R \gtrsim R_{\text{sg}}$, the disc might not collapse and a gravitoturbulent disc could instead form, as the spiral shocks can heat the gas and increase Q (Durisen et al. 2007; Deng et al. 2020). Several models have also been proposed to describe this region (e.g. Goodman 2003; Sirko & Goodman 2003; Thompson et al. 2005). For simplicity, our model does not include this potential gravitoturbulent regime.

5.2.2 Torque modelling and angular momentum inflow

In our torque evolution model, we consider two scenarios based on the mass accretion rate. For $f_{\text{Edd},16} > \hat{f}_{\text{Edd},16}$, we apply the Lense-Thirring effect derived from an inner precessing thick disc. For $f_{\text{Edd},16} < \hat{f}_{\text{Edd},16}$, we adopt the Lense-Thirring effect from the Bardeen-Petterson configuration. The exact value of $\hat{f}_{\text{Edd},16}$ is a crucial parameter, derived in Section 2.4.2, as our simulation results often exhibit a “stable state” around $f_{\text{Edd},16} \sim \hat{f}_{\text{Edd},16}$ lasting for around 1 Myr in the runs with gas-disc alignment initial conditions.

Furthermore, the transition between the two torque models in our framework is quite abrupt, leading to the emergence of this stable state observed in our simulation results. In a more realistic model, the change between the two regimes should be smoother, yielding a more gradual evolution of $f_{\text{Edd},16}$ when its value is close to $\hat{f}_{\text{Edd},16}$. This would produce a higher peak value of $f_{\text{Edd},16}$ over a shorter time interval, due to

a stronger Lense-Thirring torque, ultimately resulting in a similar overall BH growth. Our results should in principle remain qualitatively consistent.

The W_{circ} parameter sets an upper limit on the specific angular momentum of the inflow onto the accretion disc. As shown in Figure 8, a lower W_{circ} results in lower angular momentum inflow, leading to a higher mass accretion rate in the gas-disc alignment initial conditions. This makes W_{circ} a crucial free parameter in our model. However, determining its exact value (and whether it remains constant) requires a detailed study that resolves spatial scales from the accretion disc to the larger environments, providing insights into how angular momentum evolves in this region. Furthermore, we do not account for the possibility of chaotic accretion with varying angular momentum direction of the inflow in this model (e.g. Dotti et al. 2013; Fiacconi et al. 2018; Bustamante & Springel 2019).

Smoothed particle hydrodynamics simulations and GRMHD simulations indicate that a thin disc might experience a sharp change in density and tilt angle, or even fragment into rings, when the inclination angle between the BH and the disc exceeds 45° (Nealon et al. 2015; Liska et al. 2021; Speicher & Blaes 2025). This could significantly impact the structure of the accretion disc, the BH mass accretion rate, and the strength of the Lense-Thirring torque. However, quantifying how this effect influences the evolution of the SMBH is beyond the scope of this study.

5.2.3 Opacity effect

It is well known that an accurate opacity table is crucial for correctly modelling the structure of accretion discs in protoplanetary discs (Bell & Lin 1994; Semenov et al. 2003). This is often neglected for AGN accretion disc models, due to their typically high temperature, which justifies the use of a simplified opacity law. In the original thin α -disc model developed by Shakura & Sunyaev (1973), the dominant opacity source is assumed to be either electron scattering opacity or free-free absorption opacity, a treatment that is retained in, e.g. Frank et al. (2002) and K08. Consequently, our model adopts the same assumption for the opacity source when computing the structure of the thin α -disc.

However, as pointed out by, e.g. Hure et al. (1994b), Frank et al. (2002), and Perego et al. (2009), this assumption breaks down when $T \lesssim 10^4$ K. At such temperatures, hydrogen recombination significantly reduces the opacity (known as the opacity gap), meaning that it no longer follows the simple electron scattering or free-free absorption prescriptions. In the outermost regions of the accretion disc, the temperature can drop below 10^4 K when the mass accretion rate is low, thereby invalidating this opacity assumption.

For regions where $T \lesssim 10^4$ K, the opacity gap leads to a lower optical depth, allowing photons to escape more easily from the accretion disc. This further lowers the disc temperature, which in turn causes a significant drop in Q . Hure et al. (1994a,b) and Derdzinski & Mayer (2023) demonstrate that Q drops rapidly by one to two orders of magnitude when T enters the opacity gap, potentially rendering the low-temperature regions of the disc gravitationally unstable and triggering fragmentation and a reduction in disc size.

We can calculate the accretion disc temperature at R_{sg} to assess the validity of this assumption in our model. Assuming

that R_{sg} lies in region (c) of the accretion disc (i.e. $R_{\text{sg}} = R_{\text{sg},c}$), we use the temperature profile from K08 to calculate $T(R = R_{\text{sg}}) \equiv T_{\text{sg}}$:

$$T_{\text{sg}} = 5.0 \times 10^3 \alpha_{0.1}^{-2/3} M_{\text{BH},6}^{2/3} f_{\text{Edd},16}^{2/3} Q_{\text{min}}^{2/3} \text{ K} . \quad (58)$$

If we impose the condition $T_{\text{sg}} \geq 10^4$ K to ensure that the opacity assumption remains valid, then we obtain the following criterion (see also Perego et al. 2009; their numerical value slightly differs from ours because we employ the K08 solution and they use the solution by Frank et al. 2002):

$$M_{\text{BH},6} f_{\text{Edd},16} / \alpha_{0.1} \geq 2.84 / Q_{\text{min}} . \quad (59)$$

In our test runs, this criterion is not always satisfied, indicating that, in those instances, we likely overestimate the disc size. A smaller disc could potentially result in a slightly higher mass accretion rate initially, followed by a more rapid decline (Figure 9). We note that all previous accretion disc-based sub-grid models, which assume that the outer disc follows the thin α -disc and enforce $R_{\text{disc}} \leq R_{\text{sg}}$, adopt similar assumptions and may therefore be subject to the same limitations (e.g. Perego et al. 2009; Dubois et al. 2014; Fiacconi et al. 2018; Bustamante & Springel 2019; C21; Koudmani et al. 2024).¹⁶

To accurately model the low-temperature regions of the accretion disc ($T < 10^4$ K), a detailed computation using a comprehensive opacity table would be required (e.g. Gangardt et al. 2024; Rozner et al. 2025). However, such an approach is beyond the scope of this paper. Moreover, Jiang & Blaes (2020) show that the “iron opacity bump” in the detailed opacity table can cause the disc to become convectively unstable, leading to large fluctuations in surface density and temperature.

5.2.4 Other caveats

We assume that the radiative efficiency follows the expressions from Madau et al. (2014), which was derived only for aligned discs ($\theta_{\text{BH-disc}} = 0$) and extended in this work to include counter-aligned discs ($\theta_{\text{BH-disc}} = \pi$). For a misaligned disc ($0 < \theta_{\text{BH-disc}} < \pi$), we still use Equation (49), using the minus (plus) sign for $\theta_{\text{BH-disc}} \leq \pi/2$ ($\theta_{\text{BH-disc}} > \pi/2$) in Equations (50)–(52), although this expression becomes less and less accurate as we approach $\theta_{\text{BH-disc}} = \pi/2$. Hughes & Blandford (2003) provide a fitting function of η as a function of $\theta_{\text{BH-disc}}$. However, we do not adopt it in this work, as the precise value of η only slightly influences our results, since it only affects the BH growth rate through the $1 - \eta$ term. Nonetheless, if BH feedback is included, the precise value of η becomes significantly more important. In addition, these changes are only relevant if the disc remains misaligned in the innermost region, i.e. $f_{\text{Edd},16} > \hat{f}_{\text{Edd},16}$, as most of the energy conversion occurs in the inner region close to the ISCO.

¹⁶ Perego et al. (2009) also noted this limitation, but they neglected its effect, as they assume a constant f_{Edd} . Consequently, they do not require a relation between M_{disc} , J_{disc} , and f_{Edd} to update the BH mass accretion rate, which is strongly influenced by the outer parts of the disc.

Within our model, we only model gas accretion in the absence of AGN feedback mechanisms, which are crucial to the evolution of SMBHs and their host galaxies. If feedback effects are included, the BH mass accretion rate may be suppressed due to interactions between AGN-driven outflows and the surrounding gas. Coupling our model with a feedback model (e.g. Sala et al. 2021; Bollati et al. 2024) and exploring the influence of BH feedback will be addressed in future work. It is also worth noting that jet launching can rapidly reduce the BH spin in the presence of a strongly-magnetized super-Eddington accretion disc (e.g. Ricarte et al. 2023). Moreover, stellar physics (star formation and stellar feedback) are not accounted for in this study. Finally, we note that we have only studied a few configurations of BH-disc-gas alignment (or lack thereof).

6 CONCLUSIONS

We have developed a new sub-grid model for super-Eddington accretion which is based on structural and thermodynamical properties of realistic accretion discs in RHD simulations. We have implemented this model in the GIZMO code using a BH-accretion disc particle that evolves the BH mass and spin through a disc-mediated accretion rate. We have extended the models by Fiacconi et al. (2018) and C21 to incorporate super-Eddington accretion, by combining simulation results of super-Eddington flows from K18 with the three-region structure of the thin α -disc model to describe the disc structure. The evolution of the BH spin is determined by two models for calculating the Lense-Thirring torque: the Bardeen-Petterson configuration for low mass accretion rates and the inner precessing thick disc model for high mass accretion rates. An overview of the model is provided in Table 1.

This model enables us to explore the relevance of super-Eddington accretion under different boundary conditions around the BH and the accretion disc. We ran a suite of simulations in idealised scenarios with a spinning SMBH surrounded by an accretion disc embedded in a gaseous disc. We considered two types of initial conditions: (i) gas-disc alignment, in which initially the surrounding gas is aligned with the accretion disc but both are misaligned with the BH; (ii) BH-disc alignment, wherein initially the BH is aligned with the accretion disc but both are misaligned with the surrounding gas. We summarise our findings as follows:

- In order to reach high mass accretion rates, not only a sufficient gas inflow is required, but the efficient removal of disc angular momentum is also essential. One mechanism for this is the Lense-Thirring torque between a misaligned BH and disc. However, for the gas-disc alignment initial condition ($\theta_{\text{gas-disc},0} = 0$), this usually sustains at most $f_{\text{Edd},16} \sim 1$ for approximately 1 Myr (Figure 6). We stress that this level of mass accretion corresponds to $f_{\text{Edd},1} \sim 16$ and thus is considered super-Eddington in most works. This behaviour is due to the interplay between the two torque prescriptions: the torque model for high mass accretion rates has a longer alignment time-scale, whereas the model for low mass accretion rates leads to a much faster alignment. This behaviour persists under various initial conditions, in which we varied $f_{\text{Edd},16,0}$, W_{circ} , $a_{\text{BH},0}$, and $\theta_{\text{BH-disc},0}$ (Figure 8). Slightly higher accretion rates are also observed when the disc is smaller, due to

a higher Q_{\min} , or when the BH is more massive, as in these cases the initial $J_{\text{disc}}/J_{\text{BH}} \lesssim 1$ (Figure 9).

- Another way to achieve a high mass accretion rate is to reduce the disc angular momentum through the misaligned inflow of gas onto the accretion disc. We tested this scenario using BH-disc alignment initial conditions ($\theta_{\text{BH-disc},0} = 0$). We demonstrated that, in this case, the system can clearly achieve super-Eddington accretion, with $f_{\text{Edd},16}$ reaching as high as 20 for less than 0.5 Myr (Figures 11 and 13), resulting in a rapid increase in BH mass of approximately 15 per cent in such a short time-frame. This highlights the relevance of episodic super-Eddington accretion triggered by new inflows of gas with varying angular momentum into the galactic centre.

- In our simulations, the BH spin typically aligns with the direction of the surrounding gas within less than a few Myr (Figures 7, 10, and 12). For the gas-disc alignment initial conditions, this alignment occurs due to the Lense-Thirring torque between the BH and the disc. The magnitude of a_{BH} initially decreases when the disc is retrograde and then returns to its original value when the disc becomes prograde. For the BH-disc alignment initial conditions, alignment results from the combined effects of gas accretion and the Lense-Thirring torque. The magnitude of a_{BH} increases steadily due to prograde accretion. If the BH continues to experience coherent accretion over an extended period, a_{BH} will continue to increase due to sustained prograde accretion. This trend is consistent with the findings in Dotti et al. (2013).

- We extrapolate our results and explore episodic super-Eddington accretion, triggered by successive misaligned gas inflows into the galactic centre. We find that the BH can grow from an initial mass of $M_{\text{BH}} = 10^6 M_{\odot}$ at $z = 11$ to $M_{\text{BH}} \sim 7 \times 10^9 M_{\odot}$ at $z = 6$ (Figure 14), which is consistent with the most massive SMBHs observed at such redshift. This suggests that episodic super-Eddington accretion may provide a viable mechanism for reaching the mass of the most massive BHs at $z \sim 6$, when starting at $z \sim 11$ from a BH seed of $\sim 10^6 M_{\odot}$ (typical of direct-collapse scenarios). The same calculation, applied to a lower-mass seed (e.g. Sassano et al. 2021), would not yield the same result, even starting at a much higher redshift.

This model offers a new method for modelling the growth of SMBHs in the super-Eddington regime, based on a detailed physics framework. After combining our model with a suitable BH feedback model, the relevance of rapid BH growth in the early Universe can be studied in greater detail within a cosmological context. This can provide further insight into the massive SMBHs observed in the early Universe. The model could also be applied to other astrophysical systems to investigate super-Eddington accretion onto BHs, such as binary BHs or TDE-powered accretion in galaxy-scale simulations.

ACKNOWLEDGEMENTS

We thank Robert Feldmann, Mudit Garg, Alexandre Refregier, and Alessandro Trani for useful and inspiring discussions. PRC acknowledges support from the Swiss National Science Foundation under the Sinergia Grant CR-SII5_213497 (GW-Learn). AL acknowledges support by the

PRIN MUR “2022935STW” funded by European Union-Next Generation EU, Missione 4 Componente 2, CUP C53D23000950006.

DATA AVAILABILITY

The data underlying this article will be shared on reasonable request to the corresponding author.

REFERENCES

- Abramowicz M. A., Fragile P. C., 2013, *Living Reviews in Relativity*, **16**, 1
- Abramowicz M. A., Czerny B., Lasota J. P., Szuszkiewicz E., 1988, *ApJ*, **332**, 646
- Abramowicz M. A., Chen X., Kato S., Lasota J.-P., Regev O., 1995, *ApJ*, **438**, L37
- Abuter R., et al., 2024, *Nature*, **627**, 281
- Antonucci R., 1993, *ARA&A*, **31**, 473
- Bañados E., et al., 2018, *Nature*, **553**, 473
- Bachetti M., et al., 2014, *Nature*, **514**, 202
- Balbus S. A., Hawley J. F., 1991, *ApJ*, **376**, 214
- Bardeen J. M., Petterson J. A., 1975, *ApJ*, **195**, L65
- Bardeen J. M., Press W. H., Teukolsky S. A., 1972, *ApJ*, **178**, 347
- Begelman M. C., 1978, *MNRAS*, **184**, 53
- Bell K. R., Lin D. N. C., 1994, *ApJ*, **427**, 987
- Blandford R. D., Begelman M. C., 1999, *MNRAS*, **303**, L1
- Blandford R. D., Begelman M. C., 2004, *MNRAS*, **349**, 68
- Blandford R. D., Znajek R. L., 1977, *MNRAS*, **179**, 433
- Blumenthal K. A., Barnes J. E., 2018, *MNRAS*, **479**, 3952
- Boekholt T. C. N., Schleicher D. R. G., Fellhauer M., Klessen R. S., Reinoso B., Stutz A. M., Haemmerlé L., 2018, *MNRAS*, **476**, 366
- Bollati F., Lupi A., Dotti M., Haardt F., 2024, *A&A*, **690**, A194
- Bondi H., 1952, *MNRAS*, **112**, 195
- Bondi H., Hoyle F., 1944, *MNRAS*, **104**, 273
- Booth C. M., Schaye J., 2009, *MNRAS*, **398**, 53
- Burke C. J., et al., 2021, *Science*, **373**, 789
- Bustamante S., Springel V., 2019, *MNRAS*, **490**, 4133
- Capelo P. R., Dotti M., 2017, *MNRAS*, **465**, 2643
- Capelo P. R., Volonteri M., Dotti M., Bellovary J. M., Mayer L., Governato F., 2015, *MNRAS*, **447**, 2123
- Capelo P. R., Dotti M., Volonteri M., Mayer L., Bellovary J. M., Shen S., 2017, *MNRAS*, **469**, 4437
- Capelo P. R., Feruglio C., Hickox R. C., Tombesi F., 2023, in , *Handbook of X-ray and Gamma-ray Astrophysics*. Springer Nature Singapore, p. 126, doi:10.1007/978-981-16-4544-0_115-1
- Cenci E., Sala L., Lupi A., Capelo P. R., Dotti M., 2021, *MNRAS*, **500**, 3719
- Chen X., Abramowicz M. A., Lasota J.-P., Narayan R., Yi I., 1995, *ApJ*, **443**, L61
- Chen Y.-X., Jiang Y.-F., Goodman J., Ostriker E. C., 2023, *ApJ*, **948**, 120
- Chiu H. H. S., Schive H.-Y., Yang H.-Y. K., Huang H., Gaspari M., 2025, *Phys. Rev. Lett.*, **134**, 051402
- Dai X., Kochanek C. S., Chartas G., Kozłowski S., Morgan C. W., Garmire G., Agol E., 2010, *ApJ*, **709**, 278
- Dai L., McKinney J. C., Roth N., Ramirez-Ruiz E., Miller M. C., 2018, *ApJ*, **859**, L20
- Danhaive A. L., et al., 2025, *arXiv e-prints*, p. arXiv:2503.21863
- Deng H., Mayer L., Meru F., 2017, *ApJ*, **847**, 43
- Deng H., Mayer L., Latter H., 2020, *ApJ*, **891**, 154
- Derdzinski A., Mayer L., 2023, *MNRAS*, **521**, 4522
- Di Matteo T., Springel V., Hernquist L., 2005, *Nature*, **433**, 604

- Dijkstra M., Haiman Z., Spaans M., 2006, *ApJ*, **649**, 14
- Dotti M., Ruszkowski M., Paredi L., Colpi M., Volonteri M., Haardt F., 2009, *MNRAS*, **396**, 1640
- Dotti M., Colpi M., Pallini S., Perego A., Volonteri M., 2013, *ApJ*, **762**, 68
- Du P., et al., 2015, *ApJ*, **806**, 22
- Du P., et al., 2018, *ApJ*, **856**, 6
- Duan Q., et al., 2025, *MNRAS*,
- Dubois Y., Volonteri M., Silk J., Devriendt J., Slyz A., 2014, *MNRAS*, **440**, 2333
- Durisen R. H., Boss A. P., Mayer L., Nelson A. F., Quinn T., Rice W. K. M., 2007, in Reipurth B., Jewitt D., Keil K., eds, *Protostars and Planets V*. p. 607 ([arXiv:astro-ph/0603179](https://arxiv.org/abs/astro-ph/0603179)), [doi:10.48550/arXiv.astro-ph/0603179](https://doi.org/10.48550/arXiv.astro-ph/0603179)
- Eddington A. S., 1916, *MNRAS*, **77**, 16
- Fabian A. C., 2012, *ARA&A*, **50**, 455
- Fan X., Bañados E., Simcoe R. A., 2023, *ARA&A*, **61**, 373
- Fiacconi D., Sijacki D., Pringle J. E., 2018, *MNRAS*, **477**, 3807
- Fragile P. C., Liska M., 2024, *arXiv e-prints*, p. [arXiv:2404.10052](https://arxiv.org/abs/2404.10052)
- Fragile P. C., Lindner C. C., Anninos P., Salmonson J. D., 2009, *ApJ*, **691**, 482
- Frank J., King A., Raine D. J., 2002, *Accretion Power in Astrophysics: Third Edition*. Cambridge University Press
- Gabor J. M., Bournaud F., 2014, *MNRAS*, **437**, L56
- Gangardt D., Trani A. A., Bonnerot C., Gerosa D., 2024, *MNRAS*, **530**, 3689
- Gibbons G. W., 1975, *Communications in Mathematical Physics*, **44**, 245
- Goodman J., 2003, *MNRAS*, **339**, 937
- Guo M., Stone J. M., Kim C.-G., Quataert E., 2023, *ApJ*, **946**, 26
- Guo M., Stone J. M., Quataert E., Kim C.-G., 2024, *ApJ*, **973**, 141
- Heckman T. M., Best P. N., 2014, *ARA&A*, **52**, 589
- Hernquist L., 1990, *ApJ*, **356**, 359
- Hopkins P. F., 2015, *MNRAS*, **450**, 53
- Hopkins P. F., Quataert E., 2010, *MNRAS*, **407**, 1529
- Hopkins P. F., et al., 2024, *The Open Journal of Astrophysics*, **7**, 20
- Hoyle F., Lyttleton R. A., 1939, *Proceedings of the Cambridge Philosophical Society*, **35**, 405
- Hu H., Inayoshi K., Haiman Z., Quataert E., Kuiper R., 2022a, *ApJ*, **934**, 132
- Hu H., Inayoshi K., Haiman Z., Li W., Quataert E., Kuiper R., 2022b, *ApJ*, **935**, 140
- Hughes S. A., Blandford R. D., 2003, *ApJ*, **585**, L101
- Hure J. M., Collin-Souffrin S., Le Bourlot J., Pineau des Forets G., 1994a, *A&A*, **290**, 19
- Hure J. M., Collin-Souffrin S., Le Bourlot J., Pineau des Forets G., 1994b, *A&A*, **290**, 34
- Huško F., Lacey C. G., Roper W. J., Schaye J., Briggs J. M., Schaller M., 2025, *MNRAS*, **537**, 2559
- Inayoshi K., Ichikawa K., 2024, *ApJ*, **973**, L49
- Inayoshi K., Haiman Z., Ostriker J. P., 2016, *MNRAS*, **459**, 3738
- Inayoshi K., Visbal E., Haiman Z., 2020, *ARA&A*, **58**, 27
- Inayoshi K., Kimura S., Noda H., 2024, *arXiv e-prints*, p. [arXiv:2412.03653](https://arxiv.org/abs/2412.03653)
- Ingram A. R., Motta S. E., 2019, *New Astron. Rev.*, **85**, 101524
- Ingram A., Done C., Fragile P. C., 2009, *MNRAS*, **397**, L101
- Jiang Y.-F., Blaes O., 2020, *ApJ*, **900**, 25
- Jiang Y.-F., Dai L., 2024, *arXiv e-prints*, p. [arXiv:2408.16856](https://arxiv.org/abs/2408.16856)
- Jiang Y.-F., Stone J. M., Davis S. W., 2014, *ApJ*, **796**, 106
- Jiang Y.-F., Stone J. M., Davis S. W., 2019, *ApJ*, **880**, 67
- Jin C., Ward M., Done C., 2012, *MNRAS*, **422**, 3268
- Kato S., Fukue J., Mineshige S., 2008, *Black-Hole Accretion Disks — Towards a New Paradigm —*. Kyoto University Press
- Kerr R. P., 1963, *Phys. Rev. Lett.*, **11**, 237
- Khoperskov S., et al., 2021, *MNRAS*, **500**, 3870
- King A., 2003, *ApJ*, **596**, L27
- King A., Pounds K., 2015, *ARA&A*, **53**, 115
- King A. R., Lubow S. H., Ogilvie G. I., Pringle J. E., 2005, *MNRAS*, **363**, 49
- King A., Lasota J.-P., Middleton M., 2023, *New Astron. Rev.*, **96**, 101672
- Kitaki T., Mineshige S., Ohsuga K., Kawashima T., 2018, *PASJ*, **70**, 108
- Kitaki T., Mineshige S., Ohsuga K., Kawashima T., 2021, *PASJ*, **73**, 450
- Koratkar A., Blaes O., 1999, *PASP*, **111**, 1
- Kormendy J., Ho L. C., 2013, *ARA&A*, **51**, 511
- Kormendy J., Richstone D., 1995, *ARA&A*, **33**, 581
- Koudmani S., Somerville R. S., Sijacki D., Bourne M. A., Jiang Y.-F., Profit K., 2024, *MNRAS*, **532**, 60
- Kubota A., Done C., 2019, *MNRAS*, **489**, 524
- Lightman A. P., et al., 2024, *arXiv e-prints*, p. [arXiv:2409.13047](https://arxiv.org/abs/2409.13047)
- Laor A., Netzer H., 1989, *MNRAS*, **238**, 897
- Larson R. L., et al., 2023, *ApJ*, **953**, L29
- Latif M. A., Bovino S., Grassi T., Schleicher D. R. G., Spaans M., 2015, *MNRAS*, **446**, 3163
- Lense J., Thirring H., 1918, *Physikalische Zeitschrift*, **19**, 156
- Leung G. C. K., et al., 2024, *arXiv e-prints*, p. [arXiv:2411.12005](https://arxiv.org/abs/2411.12005)
- Lightman A. P., Eardley D. M., 1974, *ApJ*, **187**, L1
- Lin D., et al., 2017, *Nature Astronomy*, **1**, 0033
- Liska M., Hesp C., Tchekhovskoy A., Ingram A., van der Klis M., Markoff S., 2018, *MNRAS*, **474**, L81
- Liska M., Tchekhovskoy A., Ingram A., van der Klis M., 2019, *MNRAS*, **487**, 550
- Liska M., Hesp C., Tchekhovskoy A., Ingram A., van der Klis M., Markoff S. B., Van Moer M., 2021, *MNRAS*, **507**, 983
- Liu B. F., Yuan W., Meyer F., Meyer-Hofmeister E., Xie G. Z., 1999, *ApJ*, **527**, L17
- Liu H., Luo B., Brandt W. N., Brotherton M. S., Gallagher S. C., Ni Q., Shemmer O., Timlin III J. D., 2021, *ApJ*, **910**, 103
- Lodato G., Pringle J. E., 2007, *MNRAS*, **381**, 1287
- Lopez Armengol F. G., et al., 2021, *ApJ*, **913**, 16
- Lupi A., Haardt F., Dotti M., Colpi M., 2015, *MNRAS*, **453**, 3437
- Lupi A., Haardt F., Dotti M., Fiacconi D., Mayer L., Madau P., 2016, *MNRAS*, **456**, 2993
- Lupi A., Quadri G., Volonteri M., Colpi M., Regan J. A., 2024a, *A&A*, **686**, A256
- Lupi A., Trinca A., Volonteri M., Dotti M., Mazzucchelli C., 2024b, *A&A*, **689**, A128
- Lynden-Bell D., 1969, *Nature*, **223**, 690
- Madau P., 2025, *arXiv e-prints*, p. [arXiv:2501.09854](https://arxiv.org/abs/2501.09854)
- Madau P., Haardt F., Dotti M., 2014, *ApJ*, **784**, L38
- Maiolino R., et al., 2024, *Nature*, **627**, 59
- Martin R. G., Pringle J. E., Tout C. A., 2007, *MNRAS*, **381**, 1617
- Marziani P., Garnica Luna K., Floris A., del Olmo A., Deconto-Machado A., Buendia-Rios T. M., Negrete C. A., Dultzin D., 2025, *Universe*, **11**, 69
- Massonneau W., Dubois Y., Volonteri M., Beckmann R. S., 2023a, *A&A*, **669**, A143
- Massonneau W., Volonteri M., Dubois Y., Beckmann R. S., 2023b, *A&A*, **670**, A180
- Mayer L., 2019, in Latif M., Schleicher D., eds, *Formation of the First Black Holes*. World Scientific, pp 195–222, [doi:10.1142/9789813227958_0011](https://doi.org/10.1142/9789813227958_0011)
- Mayer L., Capelo P. R., Zwick L., Di Matteo T., 2024, *ApJ*, **961**, 76
- Mayer L., van Dokelaar F., Messa M., Capelo P. R., Adamo A., 2025, *ApJ*, **981**, L28
- McKinney J. C., Tchekhovskoy A., Blandford R. D., 2012, *MNRAS*, **423**, 3083
- Mortlock D. J., et al., 2011, *Nature*, **474**, 616
- Motch C., Pakull M. W., Soria R., Grisé F., Pietrzyński G., 2014, *Nature*, **514**, 198
- Narayan R., McClintock J. E., 2008, *New Astron. Rev.*, **51**, 733
- Narayan R., Yi I., 1994, *ApJ*, **428**, L13

Narayan R., Yi I., 1995a, *ApJ*, **444**, 231
Narayan R., Yi I., 1995b, *ApJ*, **452**, 710
Narayan R., Igumenshchev I. V., Abramowicz M. A., 2003, *PASJ*, **55**, L69
Nealon R., Price D. J., Nixon C. J., 2015, *MNRAS*, **448**, 1526
Negri A., Volonteri M., 2017, *MNRAS*, **467**, 3475
Novikov I. D., Thorne K. S., 1973, in Dewitt C., Dewitt B. S., eds, *Black Holes (Les Astres Occlus)*. pp 343–450
Ogilvie G. I., 1999, *MNRAS*, **304**, 557
Ohsuga K., Mori M., Nakamoto T., Mineshige S., 2005, *ApJ*, **628**, 368
Pacucci F., Narayan R., 2024, *ApJ*, **976**, 96
Papaloizou J. C. B., Pringle J. E., 1983, *MNRAS*, **202**, 1181
Perego A., Dotti M., Colpi M., Volonteri M., 2009, *MNRAS*, **399**, 2249
Piana O., Pu H.-Y., Wu K., 2024, *MNRAS*, **530**, 1732
Power C., Nayakshin S., King A., 2011, *MNRAS*, **412**, 269
Rafikov R. R., 2015, *ApJ*, **804**, 62
Regan J. A., Downes T. P., Volonteri M., Beckmann R., Lupi A., Trebitsch M., Dubois Y., 2019, *MNRAS*, **486**, 3892
Ricarte A., Narayan R., Curd B., 2023, *ApJ*, **954**, L22
Rozner M., Trani A. A., Samsing J., Perets H. B., 2025, *MNRAS*, **537**, 1220
Sala L., Cenci E., Capelo P. R., Lupi A., Dotti M., 2021, *MNRAS*, **500**, 4788
Sala L., Valentini M., Biffi V., Dolag K., 2024, *A&A*, **685**, A92
Sassano F., Schneider R., Valiante R., Inayoshi K., Chon S., Omukai K., Mayer L., Capelo P. R., 2021, *MNRAS*, **506**, 613
Sassano F., Capelo P. R., Mayer L., Schneider R., Valiante R., 2023, *MNRAS*, **519**, 1837
Schmidt M., 1963, *Nature*, **197**, 1040
Semenov D., Henning T., Helling C., Ilgner M., Sedlmayr E., 2003, *A&A*, **410**, 611
Shakura N. I., Sunyaev R. A., 1973, *A&A*, **24**, 337
Shi Y., Kremer K., Hopkins P. F., 2024, *ApJ*, **969**, L31
Shlosman I., Begelman M. C., 1987, *Nature*, **329**, 810
Shlosman I., Frank J., Begelman M. C., 1989, *Nature*, **338**, 45
Silk J., Rees M. J., 1998, *A&A*, **331**, L1
Sirko E., Goodman J., 2003, *MNRAS*, **341**, 501
Sądowski A., 2009, *ApJS*, **183**, 171
Sądowski A., 2011, *arXiv e-prints*, p. arXiv:1108.0396
Sądowski A., Narayan R., 2016, *MNRAS*, **456**, 3929
Souza Lima R., Mayer L., Capelo P. R., Bellovary J. M., 2017, *ApJ*, **838**, 13
Souza Lima R., Mayer L., Capelo P. R., Bortolas E., Quinn T. R., 2020, *ApJ*, **899**, 126
Speicher J., Blaes O., 2025, *ApJ*, **980**, 143
Springel V., Di Matteo T., Hernquist L., 2005, *MNRAS*, **361**, 776
Suh H., et al., 2025, *Nature Astronomy*, **9**, 271
Tamburello V., Capelo P. R., Mayer L., Bellovary J. M., Wadsley J. W., 2017, *MNRAS*, **464**, 2952
Tarténas M., Zubovas K., 2022, *MNRAS*, **516**, 2522
Thompson T. A., Quataert E., Murray N., 2005, *ApJ*, **630**, 167
Thorne K. S., 1974, *ApJ*, **191**, 507
Toomre A., 1964, *ApJ*, **139**, 1217
Toyouchi D., Inayoshi K., Li W., Haiman Z., Kuiper R., 2023, *MNRAS*, **518**, 1601
Volonteri M., Madau P., Quataert E., Rees M. J., 2005, *ApJ*, **620**, 69
Volonteri M., Sikora M., Lasota J.-P., 2007, *ApJ*, **667**, 704
Volonteri M., Silk J., Dubus G., 2015, *ApJ*, **804**, 148
Volonteri M., Habouzit M., Colpi M., 2021, *Nature Reviews Physics*, **3**, 732
Wang J.-M., Zhou Y.-Y., 1999, *ApJ*, **516**, 420
Wang F., et al., 2021, *ApJ*, **907**, L1
Watarai K.-y., 2006, *ApJ*, **648**, 523
Watarai K.-y., Fukue J., Takeuchi M., Mineshige S., 2000, *PASJ*, **52**, 133

Weinberger R., et al., 2017, *MNRAS*, **465**, 3291
Wise J. H., Regan J. A., O’Shea B. W., Norman M. L., Downes T. P., Xu H., 2019, *Nature*, **566**, 85
Yang J., et al., 2020, *ApJ*, **897**, L14
Yang J., et al., 2021, *ApJ*, **923**, 262
Yoshioka S., Mineshige S., Ohsuga K., Kawashima T., Kitaki T., 2024, *PASJ*, **76**, 1015
Yuan F., Yoon D., Li Y.-P., Gan Z.-M., Ho L. C., Guo F., 2018, *ApJ*, **857**, 121
Zwick L., Mayer L., Haemmerlé L., Klessen R. S., 2023, *MNRAS*, **518**, 2076

APPENDIX A: DIFFERENCES BETWEEN OUR MODEL AND CENCI ET AL. (2021)

Our model is built upon that of C21. We first note that C21 use $f_{\text{Edd},\eta}$ to represent the Eddington ratio (see also Footnote 3). In contrast, we adopt $f_{\text{Edd},16}$ throughout this paper, ensuring that the Eddington ratio remains independent of the radiative efficiency. Below, we summarise the differences between our model and that of C21:

(i) In C21, only region (c) of the thin α -disc is used to describe the accretion disc structure. By contrast, our model incorporates all three regions – (a), (b), and (c) – of the thin α -disc, together with a fitting formula for the photon-trapping region from K18. This results in differences in the surface density and specific angular momentum profiles, which in turn lead to differences in the disc mass and angular momentum. Consequently, the relationship between the Eddington ratio, M_{disc} , and J_{disc} is no longer a simple analytic expression like in C21. Instead, we determine $f_{\text{Edd},16}$ numerically using the Newton-Raphson method.

(ii) C21 adopt the solution in Frank et al. (2002) for the thin α -disc structure. In contrast, we use that of K08, as that work provides detailed expressions for all three regions of the thin α -disc. As described in Appendix B, there are several differences between Frank et al. (2002) and K08 (and the original description by Shakura & Sunyaev 1973), including the treatment of opacity, the definitions adopted, and the value of the mean molecular weight. Consequently, the surface density in K08 is approximately 1.7 times higher than that in Frank et al. (2002), which leads to different values of M_{sg} for a fixed M_{BH} , $f_{\text{Edd},16}$, and Q_{min} .

(iii) As we adopt a different accretion disc structure, we have re-derived the expressions for R_{warp} (Equation 27), t_{gm} (Equation 37), and R_{sg} (Equation 48) to ensure consistency.

(iv) C21 impose $f_{\text{Edd},\eta} \leq 1$ to prevent super-Eddington accretion. In our model, we do not have this limit. Instead, we introduce a new upper limit for BH accretion, denoted as $f_{\text{Edd},16,\text{max}}$ (Equation 20), which is much higher than 1 for a wide range of BH masses. For example, $f_{\text{Edd},16,\text{max}} \sim 20$ for $M_{\text{BH},6} = 1$ (and $M_{\text{disc}} = M_{\text{sg}}$).

(v) In C21, the Lense-Thirring torque is consistently calculated using the Bardeen-Petterson configuration, which is valid only at relatively low mass accretion rates ($f_{\text{Edd},16} < \dot{f}_{\text{Edd},16} \sim 1$ for $a_{\text{BH}} \gtrsim 0.5$) in our model. For higher mass accretion rates, we adopt a different torque prescription based on the inner precessing thick disc model (Section 2.4.4).

(vi) We consider the dependence on Q_{min} in our model, exploring cases with varying Q_{min} values, which set the max-

imum size of the accretion disc, to examine their impact on the SMBH evolution.

(vii) C21 use the Kerr metric to compute the radiative efficiency (Bardeen et al. 1972), which does not account for the photon-trapping effect in super-Eddington flows. In contrast, we employ an improved version of the original fitting function by Madau et al. (2014; Equations 49–52) to include this effect in the calculation of the radiative efficiency.

(viii) In our model, we initialise $M_{\text{disc},0} = M_{\text{sg}}$, whereas in C21, $M_{\text{disc},0}$ is treated as a free parameter. We adopt this approach because a substantial inflow onto the disc typically occurs at the beginning of the simulation if $M_{\text{disc},0} < M_{\text{sg}}$. This strong inflow would lead to a discontinuous increase in both M_{disc} and J_{disc} , causing $f_{\text{Edd},16}$ to deviate abruptly from its given initial value $f_{\text{Edd},16,0}$.

APPENDIX B: DIFFERENCES BETWEEN THIN α -DISC DESCRIPTIONS

The thin- α disc model was originally developed by Shakura & Sunyaev (1973) and later extended to include GR effects by Novikov & Thorne (1973). In this work, we adopt the formulation of K08 for describing such a structure. In contrast, Perego et al. (2009), Fiacconi et al. (2018), C21, and Koudmani et al. (2024) refer to Frank et al. (2002). All three non-GR references (Shakura & Sunyaev 1973; Frank et al. 2002; K08) provide similar descriptions for the thin α -disc structure, with only minor differences in normalisation and characteristic radii (e.g. R_{ab} and R_{bc}). These discrepancies arise from differences in the definitions and opacity assumptions adopted in each reference, which are summarised in Table B1.

We also note that the expression for ν_1 differs slightly in K08, as they define the α parameter via the $r\phi$ -component of the shear stress tensor, i.e. $t_{r\phi} = -\alpha P$, as opposed to Shakura & Sunyaev (1973) and Frank et al. (2002), who use $\nu_1 = \alpha c_s H$. In addition, Frank et al. (2002) adopt a significantly larger value for κ_{ff} compared to the other two references, likely due to a higher metallicity. However, this has only a weak impact on the overall results, as most quantities depend on the opacity through very low power-law exponents (typically ~ 0.1).

APPENDIX C: APPLYING THE NEWTON-RAPHSON METHOD TO CALCULATE THE MASS ACCRETION RATE

Considering the accretion disc structure discussed in Section 2.2, we can calculate M_{disc} and J_{disc} (Equations 18 and 19) by providing R_{disc} and $f_{\text{Edd},16}$, along with given values of M_{BH} , α , and a_{BH} . We then use the Newton-Raphson method to calculate $f_{\text{Edd},16}$ (Section 2.3). However, it is necessary to carefully explore the parameter space of $(M_{\text{disc}}, J_{\text{disc}})$, as degeneracies in this space can cause the Newton-Raphson method to fail.

In Figure C1, we set $M_{\text{BH},6} = 1$ and $\alpha_{0.1} = 1$ (the value of a_{BH} is not relevant, since it only affects the value of the ISCO radius, which is not used in the integration) and explore the parameter space of M_{disc} and J_{disc} . This parameter space exhibits a clear lower boundary in J_{disc} at any given

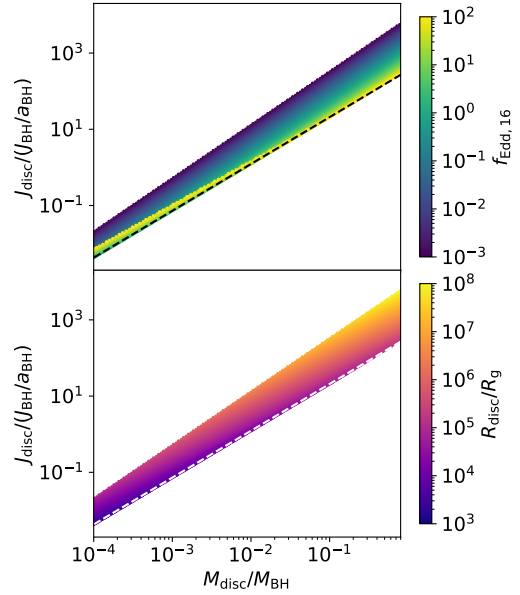


Figure C1. A section of the $(M_{\text{disc}}, J_{\text{disc}})$ parameter space for $M_{\text{BH},6} = 1$ and $\alpha_{0.1} = 1$, for different values of $f_{\text{Edd},16}$ (top panel) and R_{disc} (bottom panel). The black (white) dashed line represents the lower boundary of the parameter space in the top (bottom) panel, determined by $f_{\text{Edd},16,\text{max}}$. We consider $f_{\text{Edd},16}$ values ranging from 10^{-3} to 10^2 , with R_{disc} varying from $10^3 R_g$ to $10^8 R_g$.

M_{disc} . This behaviour arises because Σ_b and Σ_c increase with $f_{\text{Edd},16}$, whereas $\Sigma_a \propto f_{\text{Edd},16}^{-1}$. To demonstrate how this behaviour can lead to the degeneracy, we first define

$$\mathcal{P} = \left(\frac{\partial J_{\text{disc}}}{\partial f_{\text{Edd},16}} \right)_{M_{\text{disc}}} . \quad (\text{C1})$$

When $f_{\text{Edd},16} \ll 1$, the disc is dominated by regions (b) and (c). In this regime, for a given M_{disc} , if $f_{\text{Edd},16}$ increases, Σ also increases, resulting in a more compact disc and hence a smaller J_{disc} , hence \mathcal{P} is negative. However, when $f_{\text{Edd},16}$ is large, the disc becomes dominated by region (a), provided that $R_{\text{disc}} \lesssim R_{\text{ab}}$. In this case, as $f_{\text{Edd},16}$ increases, Σ decreases, resulting in a larger J_{disc} , hence \mathcal{P} is positive.

Consequently, \mathcal{P} transitions from negative to positive when $R_{\text{disc}} \sim R_{\text{ab}}$. This results in a degeneracy in the $(M_{\text{disc}}, J_{\text{disc}})$ parameter space. We can estimate the boundary of the parameter space by identifying when the condition $M_{\text{disc},a} \ll M_{\text{disc}}$ is not satisfied, where $M_{\text{disc},a}$ is the disc mass in region (a). We estimate that this condition breaks down at $R_{\text{disc}} = 2.7R_{\text{ab}}$, where $M_{\text{disc},a} \sim 0.1M_{\text{disc}}$. We can estimate the minimum disc angular momentum $J_{\text{disc},\text{min}}$ for a given M_{disc} by setting $R_{\text{disc}} = 2.7R_{\text{ab}}$. The Eddington ratio at $(M_{\text{disc}}, J_{\text{disc},\text{min}})$ is then defined as $f_{\text{Edd},16,\text{max}}$ (Equation 20). Cases where $f_{\text{Edd},16} > f_{\text{Edd},16,\text{max}}$ may result in degeneracy or no solution for a given $(M_{\text{disc}}, J_{\text{disc}})$. To avoid such failures in the Newton-Raphson method, we impose the constraint $f_{\text{Edd},16} \leq f_{\text{Edd},16,\text{max}}$.

APPENDIX D: RADIATIVE EFFICIENCY

In Figure D1, we show the value of η as a function of a_{BH} . We compare the results from Bardeen et al. (1972) to those from

Table B1. Comparison of three references used to compute the structure of a thin α -disc structure.

Reference	ν_1	Σ	μ	τ	κ_{ff} (in cgs units)
Shakura & Sunyaev (1973)	$\alpha c_s H$	$2\rho H$	1	$2\kappa\rho H$	$0.64 \times 10^{23} \rho T^{-7/2}$
Frank et al. (2002)	$\alpha c_s H$	ρH	0.615	$\kappa\rho H$	$5 \times 10^{24} \rho T^{-7/2}$
K08	$2\alpha c_s H/3$	$2\rho H$	0.5	$\kappa\rho H$	$0.64 \times 10^{23} \rho T^{-7/2}$

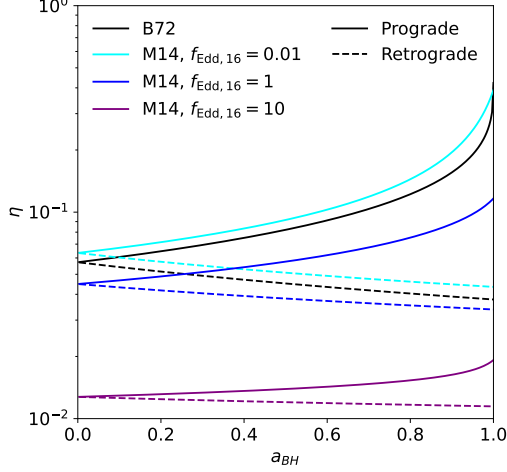


Figure D1. Radiative efficiency as a function of BH spin. The solid and dashed lines represent prograde and retrograde discs, respectively. The black lines show the relation from Bardeen et al. (1972: B72), whereas the coloured lines indicate an improved version of the original fitting function by Madau et al. (2014: M14; Equations 49–52) for different Eddington ratios: $f_{\text{Edd},16} = 0.01$ (cyan), 1 (blue), and 10 (purple).

an improved version of the original fitting function by Madau et al. (2014; Equations 49–52) with $f_{\text{Edd},16} = 0.01, 1$, and 10. It is clear that, at low mass accretion rates, both models show similar values of η . However, at high mass accretion rates, Equations (49)–(52) yield a significantly lower value than that of Bardeen et al. (1972), due to the photon-trapping effect.

APPENDIX E: EXTRA FIGURES

In this section, we show the complete results for the runs MBH-H (Figure E1), Q-VH (Figure E2), and Edd-L (Figure E3).

This paper has been typeset from a \LaTeX file prepared by the author.

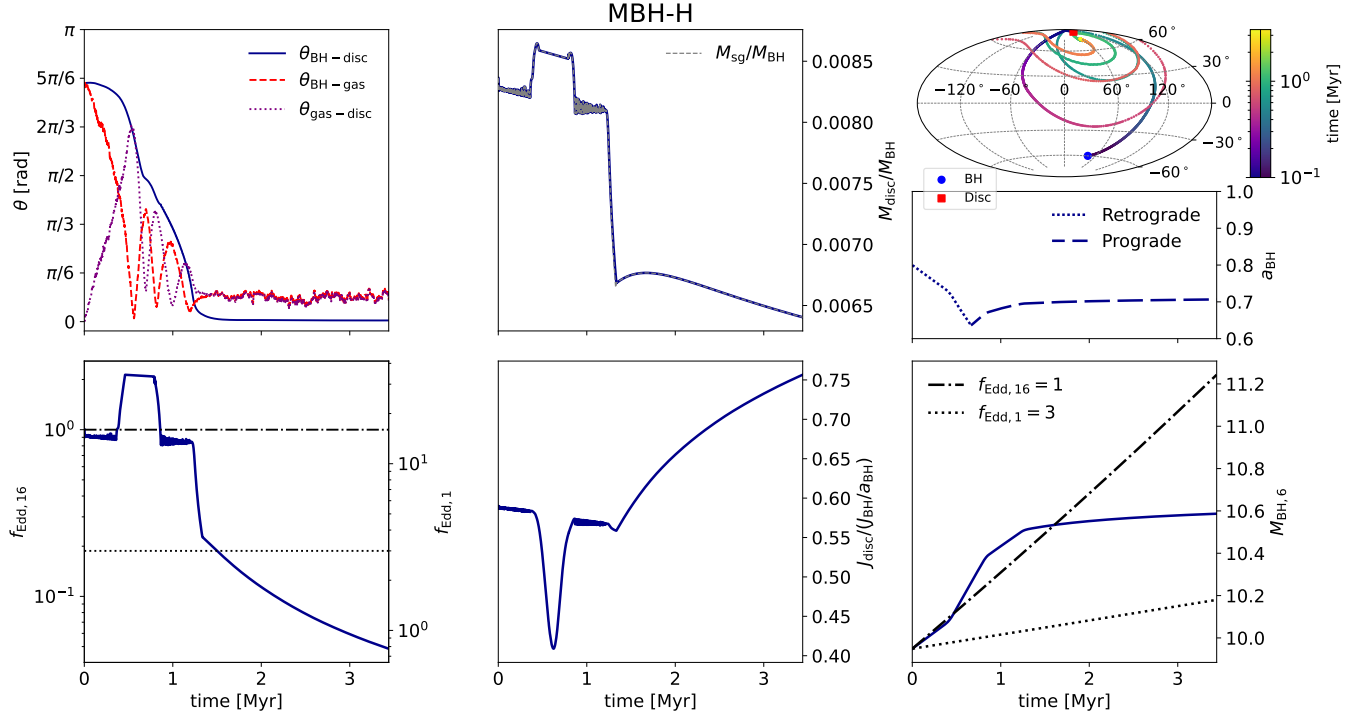


Figure E1. Time evolution of key quantities for the MBH-H run. Panels from top left to bottom right show: misalignment angles $\theta_{\text{BH-disc}}$ (solid blue line), $\theta_{\text{BH-gas}}$ (dashed red line), and $\theta_{\text{gas-disc}}$ (dotted purple line); disc mass, M_{disc} , in units of M_{BH} along with the self-gravitating mass, M_{sg} (grey line); BH (blue circle) and disc (red square) angular momenta shown via Hammer projections, colour-coded by time; a_{BH} during retrograde (dotted line) and prograde (dashed line) accretion; Eddington ratio $f_{\text{Edd},16}$, with $f_{\text{Edd},1}$ indicated on the right axis; disc angular momentum, J_{disc} , in units of $(J_{\text{BH}}/a_{\text{BH}})$; and BH mass $M_{\text{BH},6}$, with black lines showing constant specific accretion at $f_{\text{Edd},16} = 1$ and $f_{\text{Edd},16} = 3$.

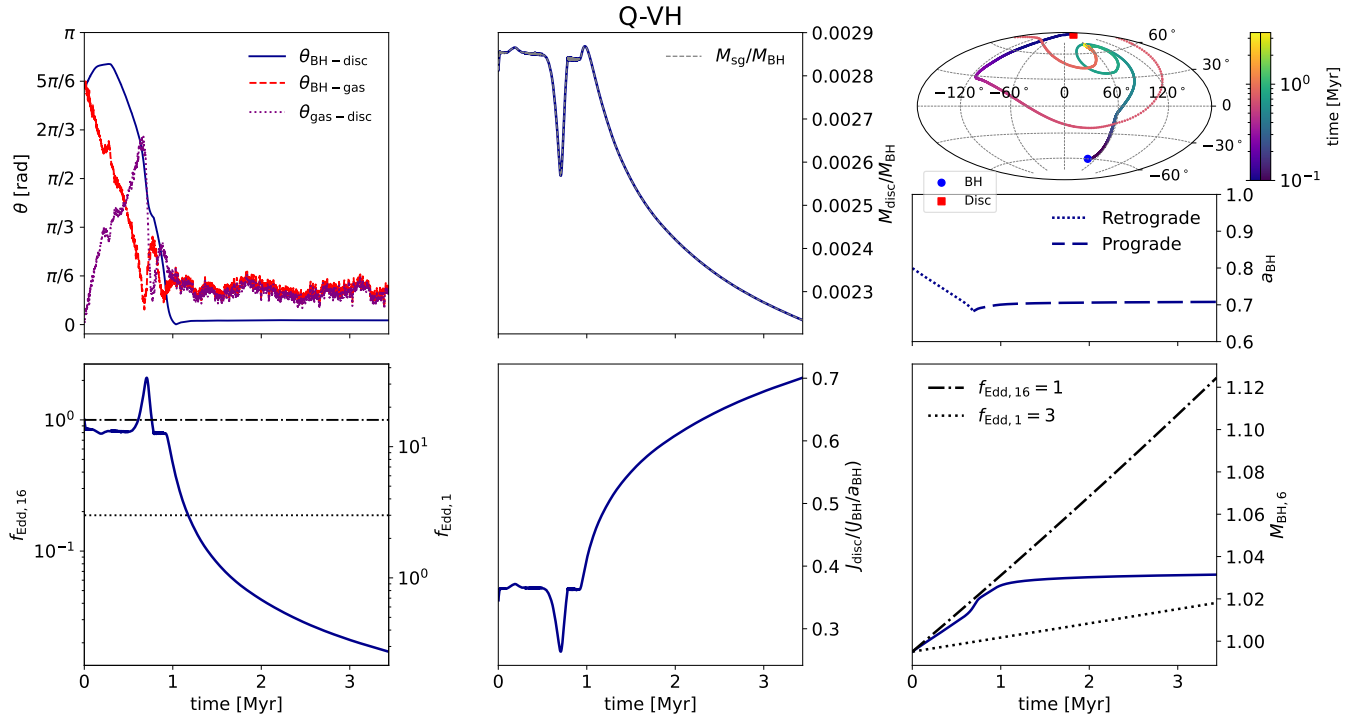


Figure E2. Same as Figure E1, but for the run Q-VH.

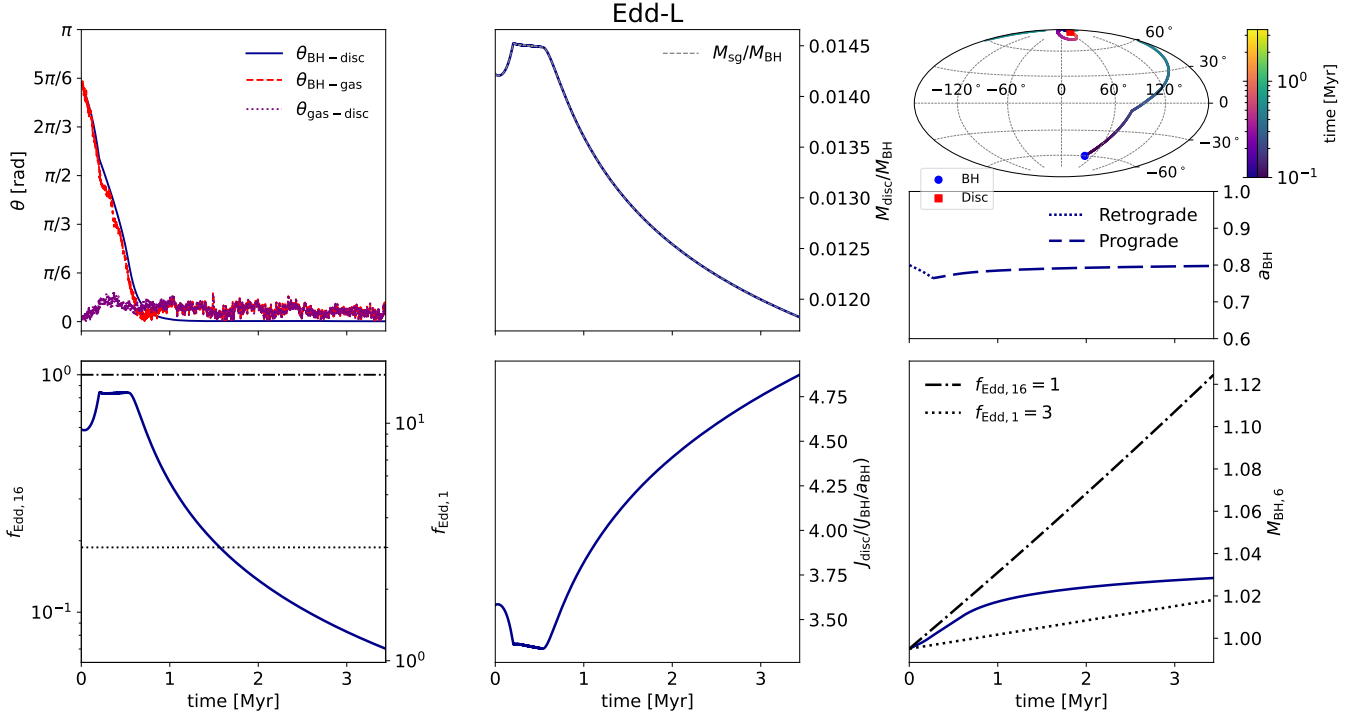


Figure E3. Same as Figure E1, but for the run Edd-L.